

Applications of Non-linearities in RF MEMS Switches and Resonators.

Krishna Prasad Vummidi Murali

Dissertation submitted to the Faculty of the
Virginia Polytechnic Institute and State University
in partial fulfillment of the requirements for the degree of

Doctor of Philosophy
in
Electrical Engineering

Sanjay Raman, Chair
Masoud Agah
Louis Guido
Majid Manteghi
Craig Woolsey

February 11, 2015
Blacksburg, Virginia

Keywords: RF MEMS, Non-linearity, Switches, Resonators

Copyright 2015, Krishna Vummidi

Applications of Non-linearities in RF MEMS Switches and Resonators.

Krishna Vummidi

(ABSTRACT)

The 21st century is emerging into an era of wireless ubiquity. To support this trend, the RF (Radio Frequency) front end must be capable of processing a range of wireless signals (cellular phone, data connectivity, broadcast TV, GPS positioning, etc.) spanning a total bandwidth of nearly 6 GHz. This warrants the need for multi-band/multi-mode radio architectures. For such architectures to satisfy the constraints on size, battery life, functionality and cost, the radio front-end must be made reconfigurable. RF-MEMS (RF Micro-Electro-Mechanical Systems) are seen as an enabling technology for such reconfigurable radios. RF-MEMS mainly include micromechanical switches (used in phase shifters, switched capacitor banks, impedance tuners etc.) and micromechanical resonators (used in tunable filters, oscillators, reference clocks etc.). MEMS technology also has the potential to be directly integrated into CMOS (Complementary metal-oxide semiconductor) ICs (Integrated Circuits) leading to further potential reductions of cost and size. However, RF-MEMS face challenges that must be addressed before they can gain widespread commercial acceptance. Relatively low switching speed, power handling, and high-voltage drive are some of the key issues in MEMS switches. Phase noise influenced by non-linearities, need for temperature compensation (especially Si based resonators), large start-up times, and aging are the key issues in Si MEMS Resonators.

In this work potential solutions are proposed to address some of these key issues, specifically the reduction of high voltage drives in switches and the reduction of phase noise in MEMS resonators for timing applications.

MEMS devices that are electrostatically actuated exhibit significant non-linearities. The origins of the non-linearities are both electrical (electrostatic actuation) and mechanical (dimensions and material properties). The influence of spring non-linearities (cubic and

quadratic) on the performance of switches and resonators are studied. Gold electroplated fixed-fixed beams were fabricated to test the phenomenon of dynamic (or resonant) pull-in in shunt switches. The dynamic pull-in phenomenon was also tested on commercially fabricated lateral switches. It is shown that the resonant pull-in technique reduces the overall voltage required to actuate the switch. There is an additional reduction of total actuation voltage possible via applying an AC actuation signal at the correct non-linear resonant frequency. The demonstrated best case savings from operating at the non-linear resonance is 50 % (for the lateral switch) and 60 % (for the vertical switch) as compared to 25 % and 40 % respectively using a fixed frequency approach. However, the timing response for resonant pull-in has been experimentally shown to be slower than the static actuation. To reduce the switching time, a shifted-frequency method is proposed where the excitation frequency is shifted up or down by a discrete amount $\delta\Omega$ after a brief hold time. It was theoretically shown that the shifted-frequency method enables a minimum realizable switching time comparable to the static switching time for a given set of actuation frequencies.

The influence of V_{DC} on the effective non-linearities of a fixed-fixed beam is also studied. Based on the dimensions of the resonator and the type of resonance there is a certain $V_{DC, Lin}$ where the response is near linear ($S \approx 0$). In the near-linear domain, the dynamic pull-in is the only upper bound to the amplitude of vibrations, and hence the amplitude of output current, thereby maximizing the power handling capacity of the resonator. Apart from maximizing the output current, it is essential to reduce the amplitude and phase variations of the displacement response which are due to noise mixing into frequency of interest, and are eventually manifested as output phase noise due to capacitive current nonlinearity. Two major aliasing schemes were analyzed and it was shown that the capacitive force non-linearity is the major source of mixing that causes the up-conversion of $1/f$ frequency into signal sidebands. The resonator's periodic response (displacement) is defined by a set of two first-order nonlinear ordinary differential equations that describe the modulation of amplitude and phase of the response. Frequency response curves of amplitude and frequency are determined from these modulation equations. The zero slope point on the amplitude resonance curve

is the peak of the resonance curve where the phase (γ_{dc}) of the response is $\pm\pi/2$. For a strongly non-linear system, the resonance curves are skewed based on the amount of total non-linearity S . For systems that are strongly non-linear, the best region to operate the resonator is the fixed point that correspond to infinite slope ($\gamma_{dc} = \pm 2\pi/3$) in the frequency response of the system. The best case phase noise response was analytically developed for such a fixed point. Theoretically at this fixed point, phase noise will have contributions only from $1/f$ noise and not from $1/f^2$ and $1/f^3$. The resonators phase can be set by controlling the rest of the phase in the loop such that the total phase around the loop is zero or 2π .

In addition, this work has also developed an analytical model for a lateral MEMS switch fabricated in a commercial foundry that has the potential to be processed as MEMS on CMOS. This model accounts for trapezoidal cross sections of the electrodes and springs and also models electrostatic fringing as a function of the moving gap. The analytical model matches closely with the Finite Element (FEA) model.

Acknowledgments

I would like to thank my advisor, Dr. Sanjay Raman: for his guidance, unwavering support, providing me with this unique opportunity to work on RFICs and MEMS at WML (Wireless Microsystems Lab), his patience, his great acumen to turn this document into something that is dissertation worthy and most of all giving me the freedom to explore this multi-disciplinary area at my will while keeping me rooted to the topic. I'm confident the knowledge I have gained in this area of work and the research work-ethic I have developed during my tenure in this lab will serve me well in my professional career long after I have graduated. I would also like extend my appreciation and thanks to Dr. Masoud Agah (ECE), Dr. Louis Guido (ECE and MSE), Dr. Majid Manteghi (ECE) and Dr. Craig Woolsey (AOE) for reviewing my dissertation and serving on my committee. I would like to thank Dr. Manteghi and Dr. Woolsey for jumping in as an able committee members in the last minute. I would like to extend a special thanks Dr. Agah for serving on my committee. I would also like to thank Dr. Guido and Dr. Hendricks for serving on my PhD qualifiers.

I would like to thank Dr. Eihab Abdel-Rahman, currently serving as an Associate Professor at University of Waterloo and his PhD student Mahmoud Khater for their research collaborations, that has been very valuable to this work. I would like to especially thank Dr. Eihab for sharing his knowledge and expertise on non-linear systems. I would like to extend my thanks to Dr. Ali H. Nayfeh, Dr. Mohamad Younis and Dr. Eihab for their contributions in the field of non-linearities in MEMS (and otherwise), which has been a crucial and necessary foundation for this work.

Next, I would like to thank folks at RF Micro Devices (RFMD Inc. now) for providing me with an year long co-op opportunity at their Silicon Technology Group which was managed by Julio Costa in their Corporate R & D. I would also like to thank Julio and Vic Steel for their generous support in funding me for my PhD work. It was a great learning experience that eventually shaped up my dissertation into addressing challenges faced by the (ever emerging) RF-MEMS industry. I would like to extend my special thanks to Jonathan Hammond: for his experience, knowledge in the MEMS industry, his tenacity in setting up experiments and simplicity in elucidation; keeping my ever verbose text in our publications to the point and officially introducing me into the world of MEMS in the industry. Finally, folks that were at RFMD namely: Dr. Tony Ivanov, George (Yiorgo) and Eric Patton for making my stay at Greensboro, NC a fun and a learning experience.

For fabrication and processing help along the way, I would like to thank all the folks at University of Cincinnati (Dr. Chong. H Ahn among others) for first introducing me to the world of MEMS. I would like to thank Chris Maxey (for first introducing me into the MicrON clean room) and passing along some ancient wisdom about the world of fabrication, Dr. Kathleen Meehan (for her e-beam evaporator knowledge), Stephen McCartney and John McIntosh (for their SEM and FIB expertise respectively), Dr. Gustina Collins (for her electroplating set-up), Dr. Jess Calata (for his Dektak training) and most of all our MicrON clean room Manager Don Leber for his almost magical hands and workmanship in keeping all the tools in their best behavior unlike the people that were operating them. I would like to thank all the old and new MicrON members along the way.

For their companionship, to their knowledge on RFICs and MEMS to inspiring me to do physical exercise, I would like to thank all the old and new members of WML and VT MEMS Lab. To Chris Maxey, Jun Zhao (especially for finding me an awesome employee referral plan for my cell phone, which to this day I still use), Rich Svitek, Gustina Collins, Arvind Narayanan, Swaminathan Muthukrishnan (especially for letting me live on his couch during my days at RFMD), Ibrahim Chamas, Mark Lehne, Joe Wood, Nikhil Kakkar, Marcus Oliver and Parrish Ralston (especially for making me guilty about my eating and exercising habits).

I would also like to thank folks at VT MEMS Lab (from across the aisle) especially Shree (name shortened to save on space and aid remembrance) for all the discussions about MEMS to world economics to cooking biryani and about why to this day he does not have texting in his plan among other things. I wish them, the best of luck in their current and future endeavors.

To all my old roommates especially Lindsay Moss, that have endured my presence and made my living experience the most enjoyable. Thanks to an old room mate, Rajesh Thirugnanam for making me realize that sometimes presentation is more important than content. Finally to some long lasting friends in the US, especially Pradeep Srinivasan, HariPriya Prakasam, Baskar Narayanaswamy and Jaganathan Narasimhan for letting me believe some things do stand test of time.

For printing my first political caricature and enduring my attempts at it for over a year, I would like to thank The Collegiate Times, an independent student-run newspaper.

For all the fun times, to being involved in the community called *grad school*, I want to thank all of the members the Graduate Student Assembly that I have worked with during graduate school. I thoroughly enjoyed my involvement with the GSA (2006 - 2009) during my graduate education at Virginia Tech. Without friends and colleagues like the members of the Graduate Student Assembly, graduate school would not have been nearly as rewarding and enjoyable. Finally the acknowledgment of friends and life at Tech would be incomplete if not for the mention of the famed (or rather infamous) bar in Blacksburg, VA: RiverMill. Thank you for all the good times.

Finally, I would like to thank all my family for making me feel wanted all the time. To my dad, Vummidi Murali (especially for putting the math bug in me) and my mom, Prathiba Murali for their unwavering love and support. No words can describe how thankful I am for the trust and confidence they had in me, the hardships and sacrifices they had to endure in shaping my future and their infinite love which i hope to carry with me always; that has given me strength everyday to strive for something always beyond my reach.

I would like to thank my sister (Supreetha Balaji Raj) for she has been my fountain of inspiration when I was growing up. I admire her for her courage and love; for making me realize that one does not exist without the other.

Last but for the least, I would like to thank my wife Deeya Muhury for being such an integral part of my life.

Finally, to the vast expanse of the unknown that instills humility in the human hearts and minds, I owe it all.

Dedication

To my maternal uncle, Tata Krishna Kumar.

Contents

1	Introduction	1
1.1	Motivation	1
1.2	MEMS in Radio Architectures	2
1.2.1	Impact of Q on Transceiver Architectures	2
1.2.2	Alternative MEMS enabled Transceiver Architectures	5
1.3	CMOS-MEMS Integration	12
1.3.1	Standard MEMS processing	12
1.3.2	CMOS-MEMS	17
1.4	Dissertation Overview	24
2	MEMS Switches and Resonators	27
2.1	MEMS switches	27
2.1.1	Electrostatic Actuation	30
2.1.2	MEMS Series Switches	34
2.1.3	MEMS Capacitive Shunt Switches	36
2.2	MEMS Resonators	39

2.2.1	Linear Resonator Model	41
2.2.2	MEMS based Oscillators	46
2.2.3	Nonlinear Resonator Model	46
2.2.4	Issues with MEMS oscillator solutions	52
2.3	Summary	52
3	Design, Modeling and Measurement Results of a Laterally Driven Variable Gap DC Contact Series Switch	53
3.1	Introduction	53
3.2	Design and Modeling	56
3.2.1	Modeling the Spring	62
3.2.2	Modeling the Actuator	64
3.2.3	Modeling Fringing fields	71
3.2.4	Contact Head Design	74
3.3	Fabrication Challenges	76
3.4	Electrical Performance	78
3.4.1	Actuation Voltage Measurements	78
3.4.2	Isolation and Insertion Loss Measurements	81
3.5	Summary	85
4	Dynamic Pull-in Phenomenon in a Variable Gap Lateral Contact RF MEMS Switch	87
4.1	Experimental Results	88

4.1.1	Regions of Operation	89
4.1.2	Resonant Switch	92
4.1.3	Impact Oscillator	95
4.1.4	Timing Response	100
4.2	Summary	101
5	Dynamic Actuation of Shunt Capacitive MEMS Switches	103
5.1	Shunt Capacitive Switch Design	104
5.2	Fabrication process	105
5.3	Shunt Switch Model	110
5.4	Experimental setup	113
5.4.1	Parameter Estimation	114
5.4.2	Estimation of Q	117
5.5	Dynamic Actuation Results	119
5.6	Dynamic Switching Methods	123
5.7	Summary	132
6	Non-linear Response of Electrostatically Actuated Beam Resonators and Oscillator Phase Noise Implications	134
6.1	Background	135
6.2	Clamped-Clamped Microbeam Resonator Model	139
6.3	Steady State Solution of the Displacement Response	141
6.3.1	Resonance curve: Points of Zero Slope	142

6.3.2	Resonance Curve: Points of Infinite Slope	144
6.4	Non-linear Cancellation of Electrostatically actuated Resonators	148
6.5	Phase Noise Analysis	152
6.6	Analytical Phase Noise Model	154
6.7	Summary	158
7	Conclusions, Contributions and Recommendations	159
7.1	Conclusions and Contributions	160
7.1.1	Modeling process non-idealities in a MEMS commercial foundry process	160
7.1.2	Influence of non-linearities on Dynamic Pull-in of lateral (series) and vertical (shunt) MEMS switches	161
7.1.3	Influence of effective non-linearities on the phase noise performance of MEMS electrostatic resonators	162
7.2	Recommendations for Future Work	163
7.2.1	RF MEMS Switches	163
7.2.2	RF MEMS Resonators	164
	Bibliography	165

List of Figures

1.1	Simplified superheterodyne receiver architecture	3
1.2	Transmission (dB) versus frequency for a 4th order LC Chebyshev filter with various values for inductor Q	4
1.3	System block diagram of a super-heterodyne receiver architecture showing potential MEMS replacements via MEMS-based components.	5
1.4	Multi-band/Multi-mode radio architecture.	8
1.5	Multi-band/Multi-mode reconfigurable radio architecture showing potential MEMS replacements shaded in blue bubbles.	9
1.6	System block diagram for a RF channel-select architecture utilizing large numbers of micromechanical resonators in banks to trade Q for power consumption.	11
1.7	System block diagram for an all-MEMS receiver front-end, employing an RF image reject filter, a fixed μ mechanical resonator local oscillator, and a switchable array of IF μ mechanical mixer-filters.	12
1.8	Bulk micromachining of Si showing anisotropic (a & b) and isotropic etching (c & d)	14
1.9	Surface micromachining showing lift-off (a), dielectric patterning (b), sacrificial layer patterning (c), electroplating and release of a fixed-fixed beam (d).	15

1.10	MetalMUMPs process flow showing steps (a) - (f) (from [1]).	18
1.11	MetalMUMPs process flow showing steps (h) - (l) (from [1]).	19
1.12	MetalMUMPs process flow showing steps (m) - (p) (from [1]).	20
1.13	Hybrid approach (a) versus monolithic integration (b) of MEMS and CMOS	22
1.14	Cross-section schematic of an iMEMS process from Sandia.	22
1.15	Cross-sections (a) immediately before and (b) after release in the original polysilicon MICS process, a surface-micromachining process done directly over CMOS. (c) SEM of the 16.5-kHz CMOS μ mechanical oscillator.	23
2.1	1-D MEMS Switch model.	30
2.2	Equilibrium relationship between plate displacement and applied voltage. . .	32
2.3	The total stiffness as a function of displacement. The simulations shown are for a switch with a gap of 5 μ m. Positive stiffness indicates unstable equilibrium point.	33
2.4	Switch Classification: Broadside MEMS-series switches with (a) one electrode, (b) two electrodes, and (c) inline MEMS-series switches	35
2.5	Equivalent Electrical model (a) Switch open (b) Switch closed.	35
2.6	Plot showing switch isolation for different typical open-state capacitances. . .	36
2.7	Plot showing switch insertion loss for different series contact resistances. . .	37
2.8	Side view of a shunt capacitive switch and its electrical equivalent circuit model	38
2.9	Mechanical lumped model for the resonator.	43
2.10	(a) Measured spectrum of a MEMS resonator; (b) its equivalent model . . .	45

2.11	Implementation of a MEMS based reference Oscillator. b) Equivalent circuit for both drive and sense electrodes separately. c) Equivalent circuit combing both drive and sense electrodes.	47
2.12	The effect of nonlinear stiffness on the resonator frequency.	50
3.1	3D switch model. Insets show SEMs of switch: a) contact. b) asymmetric electrode spacing. The dotted arrows in the figure indicate the direction of motion.	55
3.2	Optical images of the contact head and electrodes when no voltage is applied (a, b).	55
3.3	Plot shows switch forces, F_{net} in μN as function of electrode travel, Δ in μm	59
3.4	SEM pictures a)Top-view of the electrode, b) Electrode cross-section ($A - A'$) and c) Spring cross-section depicting trapezoidal profiles. The cross-sections were obtained using Focused Ion Beam (FIB).	61
3.5	3D Cross sections: a) Electrodes and b) Springs with Trapezoidal Profile . .	61
3.6	Schematic representation of the asymmetric electrode spacing in the actuator.	62
3.7	Free-body diagram of a serpentine spring	64
3.8	Plot of spring constant values as function of sidewall angle α calculated analytically and compared with FEA. Castigliano's energy method models the spring stiffness more accurately than the simple bending analysis	65
3.9	Capacitance as a function of α when the applied Voltage = 12 V and 20 V. .	68
3.10	Plot of maximum switch travel (Δ_{PI}) before pull-in as a function of sidewall angle α . The plot shows the travel for a single sided capacitor (squares) and a double sided capacitor (circles) as a function of the sidewall angle α	69

3.11	Plots of Pull-in voltage (V_{PI}) as a function of side-wall angle (α) by keeping K_x as constant (triangles), by keeping Capacitance as a constant (circles) and finally varying both Capacitance and K_x as a function of α (squares).	70
3.12	Electrostatic forces as a function of α when Voltage = 12 V and 20 V (solid lines) by not accounting for the influence of α on K_x (is held constant). The dotted lines in both the graphs correspond to the electrostatic forces after accounting for the influence of α on K_x in computing the travel for the above voltages.	72
3.13	Electrode cross-section showing the increased capacitance area between the electrodes accounting for increased capacitance due to the fringing fields. . .	73
3.14	Plot of analytical CV curves comparing, Analytical models: Constant fringe (blue) and Variable fringe (red). FEA model (orange) agrees well with the variable fringe model.	75
3.15	Different configurations of the head with width and angle variations.	75
3.16	a) Au overplate on Ni sidewall b) bottom of Ni electrode showing electroplating seed layer c) Coventor FEA simulation of stress gradient d) uniform overplate.	77
3.17	The above schematic depicts the top view of the movable and fixed electrodes. The dashed edges are the drawn mask dimensions and the solid edges are the fabricated switch dimensions.	79
3.18	Plot of CV curves comparing, Measured data (blue), Ideal Model (green), Analytical Model (red) and FEA models with and without stress (blue and orange).	80
3.19	Switch Isolation with Si undercut on a high ρ substrate.	80

3.20	Isolation study of multiple heads: Varying Si undercut and substrate resistivity (ρ) measured in dB at 2 GHz	81
3.21	Insertion loss plots of actuators with different contact heads.	82
3.22	I-V curves showing Break down Voltages (B.V) at the contact for high and low actuation voltages.	83
3.23	Force vs contact resistance without (a) and with (b) an observed breakdown voltage.	84
4.1	(a, b) Optical images of the contact head and electrodes when no voltage is applied.	90
4.2	First three resonant modes of the switch under study. Finite Element Simulations were done using Coventor.	91
4.3	Linear resonant frequency vs. V_{DC} for the first mode of resonance.	91
4.4	Different regions of operation for the switch with $V_{SP} = 41 V$. The combination of V_{DC} and v_{ac} values maps to different regions of operation. The frequency of operation corresponds to the first mode of resonance. The numbers on the plot correspond the the different v_{ac} (RMS) values.	93
4.5	Combination of V_{DC} and v_{ac} values for a constant frequency (dotted line) and for varying frequency (solid line).	96
4.6	Shows the percentage savings of V_{FOM} w.r.t static pull-in for varying amplitude (dotted line) and varying frequency (solid line).	96
4.7	Shows percentage savings w.r.t to V_{DP} and V_{SP}	97
4.8	Timing measurement set-up also used to capture switch response as an impact oscillator	98

4.9	Oscilloscope screen capture of the switch’s response at the output of the diode detector. The switch is resonating while opening and closing the contact head.	99
4.10	Circuit topologies of (a) a conventional Class E amplifier using a transistor switch device; and (b) one simplified rendition of the proposed Class E amplifier utilizing a “resoswitch” as driven by the input ac signal v_i .	100
4.11	Average values of switch response times for different methods of actuation.	101
4.12	Scope capture of the switch’s response when a $V_{DC} + v_{ac}$ is applied. An RF signal is switched through a diode detector to measure the response time.	102
5.1	A cross-section schematic of the shunt microswitch structure.	104
5.2	A schematic of the shunt microswitch.	106
5.3	Fabrication procedure of the capacitive shunt switch.	107
5.4	An SEM picture of a positive photo-resist with a lift-off profile.	108
5.5	Supercritical drying (yellow arrow) goes beyond the critical point of the working fluid in order to avoid the direct liquid-gas transition seen in ordinary drying (green arrow).	110
5.6	SEM pictures showing switches released a) without and b) with critical point dryer.	111
5.7	Shunt switch testing set-up	114
5.8	A 3-D picture of the beam profile using a white light profilometer.	115
5.9	Variation of the fundamental natural frequency with DC voltage.	117
5.10	Experimental frequency-response curve for the RMS velocity of the beam midpoint at ($V_{DC} = 10$, $V_{AC} = 17$) V.	118

5.11	The frequency-response curves of the midpoint RMS velocity for (a) low bias voltage and high AC voltage ($V_{DC} = 20, V_{AC} = 26.5$) V and (b) high bias voltage and low AC voltage ($V_{DC} = 50, V_{AC} = 6.5$) V.	121
5.12	The nonlinear resonance frequency λ as a function of AC voltage V_{AC} at different bias voltages V_{DC}	122
5.13	$V_{DC} - V_{AC}$ combinations required for dynamic pull-in for procedure 1 (circles) and procedure 2 (triangles)	123
5.14	The figure of merit FoM representing the efficiency of dynamic actuation procedures 1 (circles) and 2 (triangles) compared to static actuation.	124
5.15	Frequency-response curve for ($V_{DC} = 56, V_{AC} = 5.8$) V, showing touch-down regions for different switching methods. The x-axis is separated into different regions for different switching methods based on the frequency values. A [68.75 - 75.97] KHz, B_1 [63.7 - 68.75] KHz, B_2 [76 - 79.7] KHz and B_3 [79.7 - 84.1] KHz.	125
5.16	The simulated phase portrait of fixed-frequency switching for ($V_{DC} = 56, v_{ac} = 5.8$) V and $\Omega = 70.6$ kHz, for subinterval A in figure 5.15. The dashed lines depict the homoclinic orbit.	127
5.17	(a) The simulated phase portrait and (b) time history of shifted-frequency switching for the waveform ($V_{DC} = 56, V_{AC} = 5.8$) V starting from an initial excitation frequency $\Omega_o = 67.5$ kHz in the subinterval B_1 from figure 5.15.	129
5.18	(a) The simulated phase portrait and (b) time history of shifted-frequency switching for a waveform of ($V_{DC} = 56, V_{AC} = 5.8$) V starting from an initial excitation frequency $\Omega_o = 83.2$ kHz in subinterval B_3 from figure 5.15.	130
5.19	a) Simulated phase portrait at $V_{DC} = 56$ V and $V_{AC} = 5.8$ V starting from an orbit at $\Omega = 76.92$ kHz and (b) time history with the frequency step function for subinterval B_2 from figure 5.15.	131

6.1	Implementation of MEMS based reference oscillator.	136
6.2	Illustration of an ideal vs. non-ideal spectrum.	137
6.3	Sequence of amplitude-frequency resonance curves for which $S = \pm 1$ (figures 6.3(a) and 6.3(b) respectively) and $\mu = \omega = 1$	146
6.4	Sequence of phase-frequency resonance curves corresponding to the resonance curves of figure 6.3.	147
6.5	Nonlinearity coefficient S verses VDC.	149
6.6	Frequency-response curves in the hardening domain.	150
6.7	Frequency-response curves in the softening domain.	151
6.8	Frequency-response curves in the near-linear domain.	151
6.9	Simulated phase noise plots of the resonator, with finite (blue) and infinite (yellow) Q	157

List of Tables

1.1	Summary of some wireless standards included in 4G Systems	7
2.1	Reliability and performance summary of RF MEMS metal-contact switches, from 2008	39
2.2	Reliability and performance summary of RF MEMS capacitive switches and switched-capacitors, from 2008	40
2.3	Micromechanical Resonators and their applications over the frequency, from 2008	42
3.1	Physical dimensions and material constants of the Lateral switch in discussion.	58
4.1	V_{FOM} vs. V_{DP}	94
5.1	Tabulation of various switch designs	105
5.2	Process parameters for nitride deposition on a TRION PECVD system.	106
5.3	Process parameters for nitride etching on a TRION RIE system.	109
5.4	Switch properties and dimensions.	117
6.1	Dependence of the nonlinearities on V_{DC} and resonator dimensions.	141

6.2	Physical dimensions and material constants.	148
-----	---	-----

Chapter 1

Introduction

1.1 Motivation

From its beginnings in 1901, when Marconi first transmitted his simple message across the Atlantic Ocean with a spark gap generator [2], wireless communications has grown into a multi-billion industry influencing nearly every part of society. The handheld wireless communication devices of the future are becoming more and more complex, capable of operating in global cellular standards (like GSM - Global System for Mobile Communications, UMTS - Universal Mobile Telecommunication System, and emerging 4G LTE technologies), and increasingly supporting other functions such as global positioning (GPS), digital video and audio broadcast (DVB, DAB), wireless local and body area network (WLAN, WBAN) for mobile internet access, and, proximity radio (e.g., Bluetooth) for wireless headsets or printing [3], [4], [5]. These diverse requirements necessitate multi functional, adaptive and low-power radio systems, imposing significant challenges on the current technology and illustrating the need for newer and enabling technologies including novel circuit architectures, tunable filters, reconfigurable impedance matching networks, multiple frequency antennas, advanced materials and novel integration and packaging methods. Current semi-conductor technologies (CMOS, RF-CMOS and III-V) and filter/resonator technologies (Surface Acoustic Wave

(SAW) and Bulk Acoustic Wave (BAW) filters, Quartz crystals etc.) are employed in the design of all the basic wireless transceiver components (amplifiers, oscillators, mixers, doublers, filters, timing references, antennas, switches and so on) and these are packaged and integrated at board level and generally are not reconfigurable. However, over the last two decades research efforts on micromachining and Micro-Electro-Mechanical Systems (MEMS) have been leveraged in field RF-MEMS (Radio Frequency MEMS) that represent a potentially significant enabling technology in developing tunable/reconfigurable, miniaturized, low-cost and low-energy RF components and systems.

1.2 MEMS in Radio Architectures

The vast majority of RF transceivers currently in production use some form of the heterodyning architecture developed by Edwin Armstrong for FM modulation over 75 years ago [6]. A typical super-heterodyne receiver architecture is shown in figure 1.1. Most of the subcircuits, including the amplifiers, mixers, and oscillators are amenable to integration in semiconductor (integrated circuit) technologies. On the other hand, the band-select, image-reject, and channel-select filters and crystal oscillator references critical to the radio architectures, typically require substantially higher Q-factors which are not achievable on-chip in the standard IC processes. High-Q components, which are currently realized using off-chip surface acoustic (SAW), ceramic, or quartz piezoelectric devices, may have Q-factors of 1000 or greater [7]. On the other hand, on-chip realizations using monolithic inductors and capacitors would typically have Q-factors three orders of magnitude lower.

1.2.1 Impact of Q on Transceiver Architectures

The Q-factor of a resonating element can be defined as:

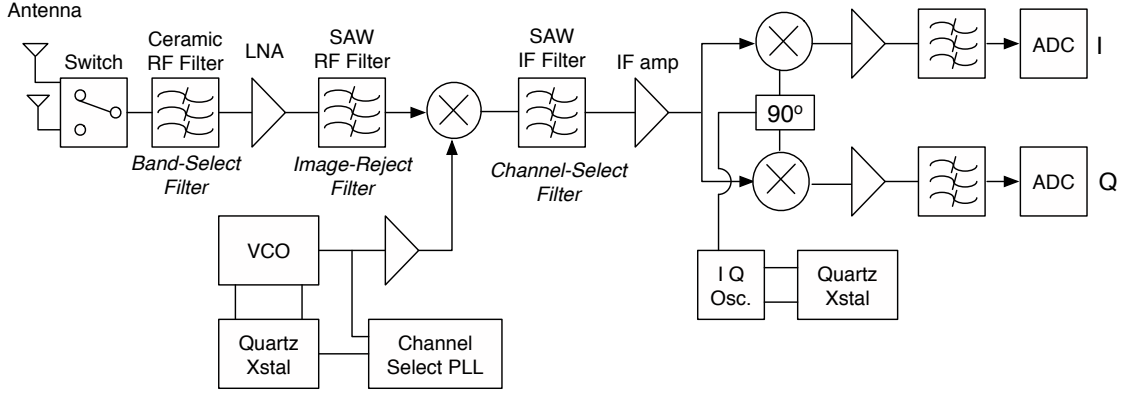


Figure 1.1: Simplified superheterodyne receiver architecture.

$$Q = 2\pi \frac{E_S}{E_D} \quad (1.1)$$

where E_S is the energy stored by the device and E_D is the energy dissipated by the device in one cycle. In filter design, the number of cascaded elements, or poles determine the sharpness of the filter, i.e. the ratio of passband transmission to out-of-band rejection which will increase as the number of poles are increased. Each resonant element will have some non-zero loss associated with it resulting in a finite Q-factor. Therefore, increasing the number of finite-Q poles to increase filter sharpness has an undesired effect of increasing insertion loss, i.e. attenuating the filtered signal transmission in the passband. The band-select filter is the first component of the transceiver (see figure 1.1) seen by the incoming signal after the antenna, and since it is a passive component, its noise figure (NF) is approximately equal to the insertion loss of the filter in the band of interest. Since, the first element in the receive chain is the most critical in determining the overall NF of the system and in order to reduce the overall system NF the band-select filter has to be a very low loss component.

Figure 1.2 shows how low-Q factors can affect the pass band transmission for a 4th order chebyshev filter designed as a band-select filter for UNII band (5.15 - 5.25 GHz). Resonator Q-factors as high as 10,000 are required if the loss in the passband is to be kept to a reasonable

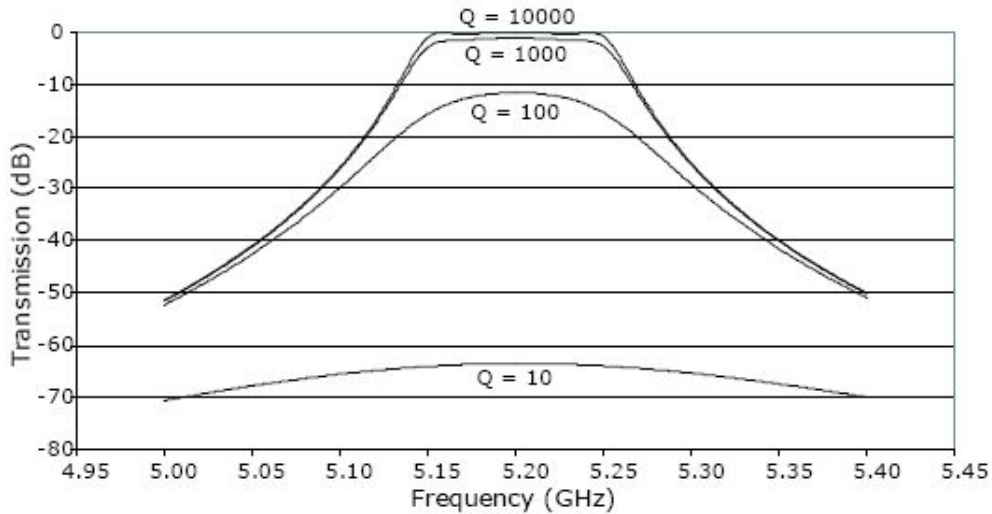


Figure 1.2: Transmission (dB) versus frequency for a 4th order LC Chebyshev filter with various values for inductor Q , after [7].

level (≤ 0.1 dB) [7]. The insertion loss of the filter simulated in figure 1.2 is approximately 11 dB for $Q = 100$ and 0.12 dB for $Q = 10000$. Since, MEMS resonators are potentially very high Q , an obvious way to leverage RF MEMS devices is as direct on-chip replacements of off-chip components in an existing RF architecture.

Analyses before and after replacement of off-chip high- Q passives by higher Q MEMS versions in a super-heterodyne architecture often show dramatic improvements in receiver noise figure, e.g., from 8.8 dB to 2.8 dB [8]. Also, when minimizing the use of high- Q components, one often expends more power to achieve the desired transceiver performance. As a simple illustration, if the high- Q IF filter in the receive path of a communication subsystem is removed, the dynamic range requirement on the subsequent IF amplifier, IQ mixer, and A/D converter circuits, increase dramatically, forcing a corresponding increase in power consumption. Similarly if a large number of high- Q passive components are used at RF, the power consumption in subsequent transistor based circuits can be reduced. Figure 1.3 again depicts the traditional heterodyning architecture of a typical wireless transceiver. The green

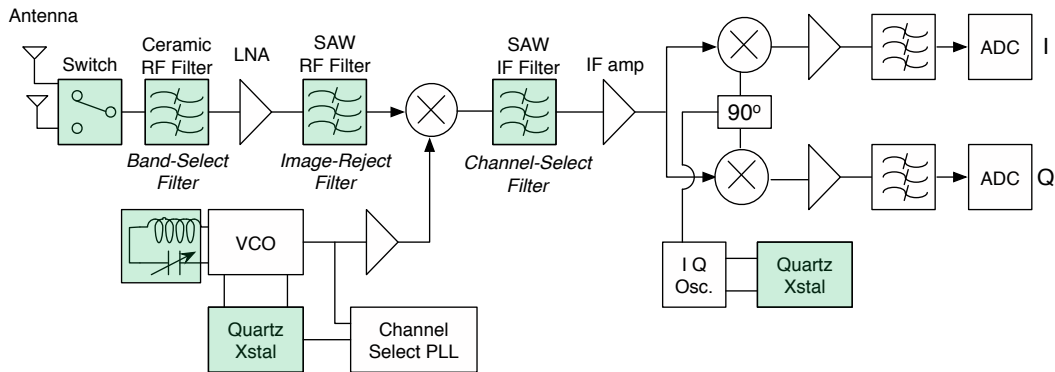


Figure 1.3: System block diagram of a super-heterodyne receiver architecture showing potential replacements via MEMS-based components. The on-chip μ mechanics are shaded.

shading in the figure indicates components that can potentially be realized with MEMS technology. These include switches, phase shifters, tank circuits, resonators, filters and impedance tuners. To fully harness the advantages of μ mechanical circuits, designs should take advantage of their micro-scale size, near zero dc power consumption, and high Q. Full utilization of the properties of MEMS may well require a rethinking of the overall radio architecture and may prove well suited for low-power, high-performance reconfigurable radio transceivers.

1.2.2 Alternative MEMS enabled Transceiver Architectures

The simplest way to harness the small size of micromechanical circuits is add reconfigurability to a transceiver by adding a bank of preselect and tunable filters that can accommodate different communications standards as shown in figure 1.4 and Table 1.1. RF-MEMS is potentially as a key enabling technology for such reconfigurable radio architectures.

In wireless communications, a “band” refers to a specific range of radio frequencies associated with a particular application. For example, the PCS “1900” band (Personnel Communications Services, the FCC-licensed frequency band near 1900 MHz) spans frequencies from

1850 MHz to 1995 MHz. A “mode” or “standard” refers to the type of modulation, multiple access, coding etc. used. Hence a multi-band/multi-mode phone should be able switch between different frequency bands and different standards which employ these bands. Figure 1.4 shows a multi-band/multi-mode radio architecture. The different standards included in 1G through 4G systems are listed in Table 1.1 [9]. 4G refers to the fourth generation of cellular wireless standards, a successor to 3G and 2G standards. 2G represented the move from analog (1G) to digital (2G) transmission. This was followed by multi-media support, with data rates of least 200 kbit/s (3G), and now 4G systems are capable of providing between 100 Mbit/s and 1 Gbit/s speeds.

The drive for increased functionality (as seen in table 1.1) in reduced form factors necessitates a higher degree of integration of the radio front-end combined with further miniaturization of the components, as well as novel front-end architectures based on reconfigurability of the radio front-end. Reconfigurable radio (sometimes referred to as Software Defined Radio (SDR)) will allow the same transceiver and modem chain to be re-configured under software control to switch between different frequency bands and standards. In a conventional architecture, for each new band added into a multi-band front-end, the entire front-end architecture needs to be repeated. This is because band-specific filters, and possibly band-specific LNAs/PAs, etc., are needed in both receive and transmit chains. This parallelization, implying increased component count, can be mitigated using reconfigurable switched filter banks or tunable filters. RF MEMS has the potential to be the key enabling technology to implement such reconfigurable radio architectures (see Figure 1.5), while at the same time attaining higher levels of integration. RF-MEMS components for use in future reconfigurable radios include switches/switch matrix and voltage-tunable capacitors (for use in tunable impedance matching networks), bulk acoustic wave (BAW) devices and micromechanical resonators (for use in tunable filters and oscillator circuits) and are shown as blue bubbles in figure 1.5.

Taking this concept further, figure 1.6 presents the system-level block diagram for a conceptual transceiver front-end architecture that further takes advantage of the capabilities of μ mechanical circuits [11]. The main goal of this architecture is power reduction, attained in

Description	Standard	Access technique	Modulation type	Frequency band T_x/R_x (MHz)	Channel spacing (MHz)	Data rate (Mb/s)
Cellular, 1G (analog voice)	AMPS	FDD	FM	824-849/869-894	0.03	N/A
Cellular, 2G (digital voice, SMS)	GSM	TDMA/FDMA	GMSK	890-915/935-960	0.2	0.27
	DCS - 1800	TDMA	GMSK	1710-1785/1805-1850	0.2	0.27
	PCS - 1900	TDMA	GMSK	1880-1910/1930-1955	0.2	0.27
	IS - 95	CDMA	OQPSK	824-849/869-894	1250	1.228
Cellular, 2.5G	EDGE	TDMA	FDD	1850-1910/1930-1990	0.2	0.27
	GPRS	TDMA	FDD	880-915/925-960	0.2	0.27
Cellular, 3G (voice, multi-media, broadband Internet access)	WCDMA (UMTS)	CDMA	QPSK	1920-1980/2110-2170	5	3.84
Cellular, 3.5G (high-speed download/uplink access)	HSDPA	OFDM/MIMO	QAM	1920-1980/2110-2170	5	14.4
	HSUPA	OFDM/MIMO	QAM	1920-1980/2110-2170	5	5.76
Wireless personal area networks (WPAN)	Bluetooth (IEEE 802.11 FH)	CDMA/FH	GFSK	2400-2483	1	1
	Zigbee	CDMA/FH	GFSK	2402-2480	5	0.02,0.04,0.250
	UWB	CDMA/FH	SP/FS	3100-10600	500	110-480
Wireless local area networks (WLAN)	IEEE 802.11a	OFDM	BPSK	5000	16.25	6-54
	IEEE 802.11b	DSSS	D-BPSK/D-QPSK	2400	22	1-11
	IEEE 802.11g	DSSS	D-BPSK/D-QPSK	2400	16.25-22	1-54
	IEEE 802.11n	OFDM/MIMO	QAM	2400,5000	22	>100, >1000 (stationary)
Metro area networks (WMAN)	IEEE E 802.16/e (WiMAX)	OFDM/MIMO	BPSK/QPSK/QAM	2000-11000	28	>100 (mobile)

Table 1.1: Summary of some wireless standards included in 4G Systems, after [9].

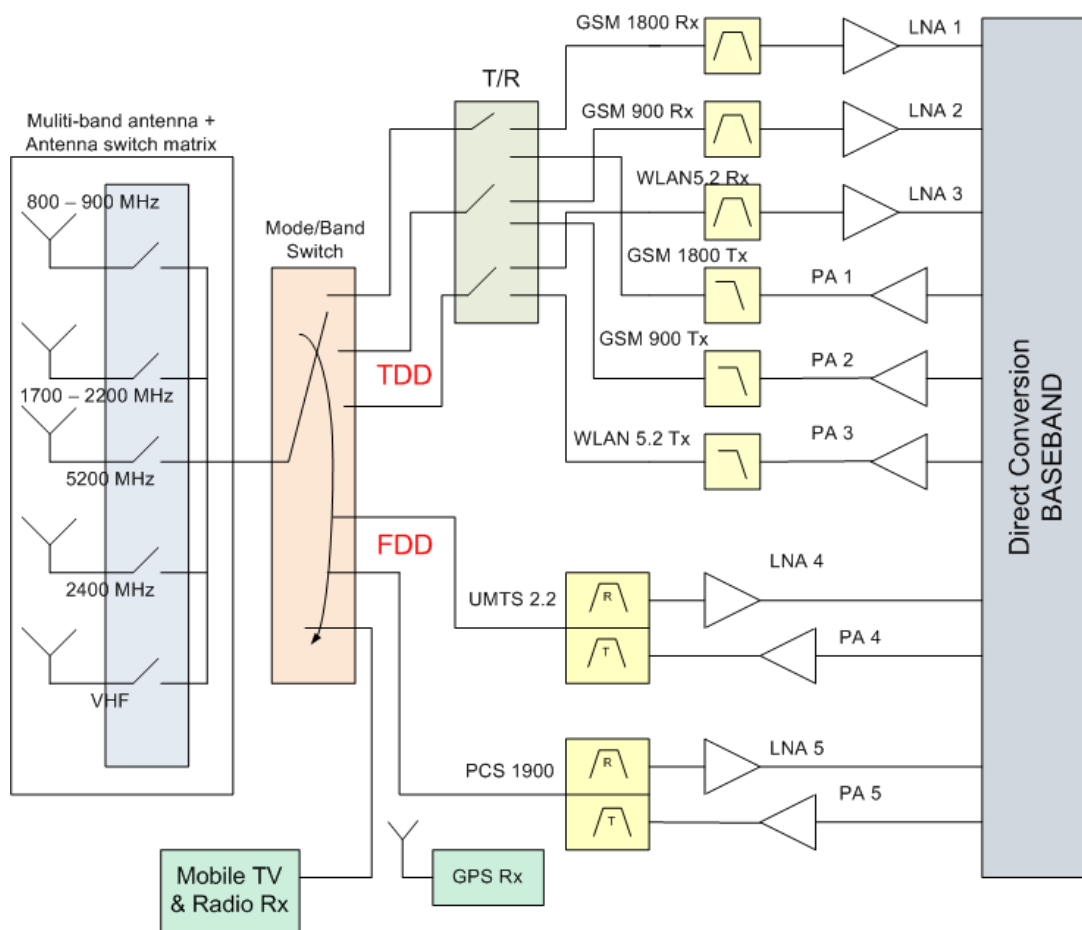


Figure 1.4: Multi-band/Multi-mode radio architecture, after [10].

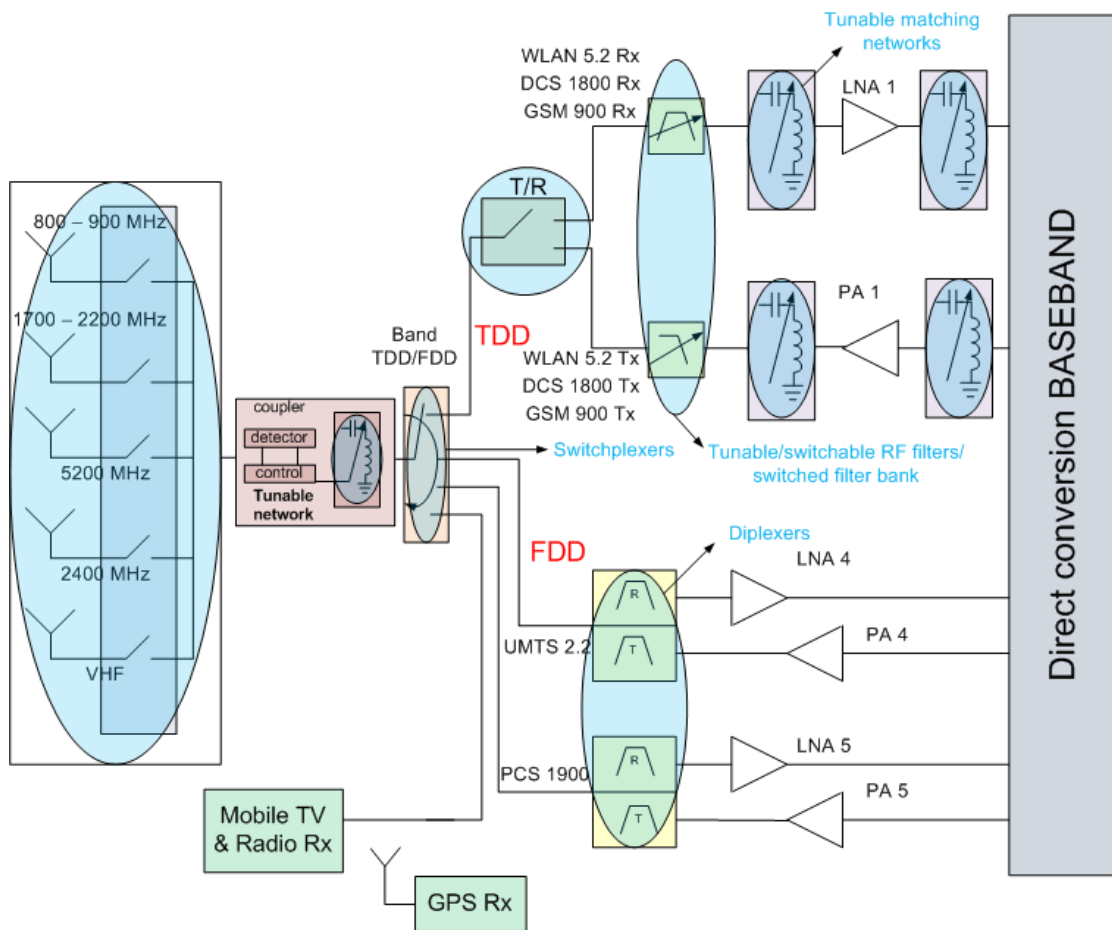


Figure 1.5: Multi-band/Multi-mode reconfigurable radio architecture showing potential MEMS replacements shaded in blue bubbles, after [10].

several of the blocks by replacing active components by low-loss passive μ mechanical devices. Among the key performance enhancing features are:

1. An RF channel selector comprised of a bank of switchable μ mechanical filters, offers multi-band reconfigurability and receiver power savings via relaxed dynamic range requirements. Channel selection at RF frequencies enables succeeding electronic blocks to avoid handling the power of adjacent channel interferes; thus, their dynamic range (linearity requirements) can be greatly relaxed, allowing substantial power reductions.
2. Use of a passive μ mechanical mixer-filter to replace the active mixer normally used, with further power savings.
3. A VCO referenced to a switchable bank of μ mechanical resonators, capable of operating without lower frequency reference, with orders of magnitude of lower power savings than present-day synthesizers since it does not require a PLL (Phase Locked Loop) to maintain a lock.
4. Use of a μ mechanical T/R switch, with already described power savings in transmit-mode.
5. Use of MEMS switches switching between different capacitive banks to implement variable matching networks. The purpose of an adaptive matching network is to effectively change the loading impedance of the output stage of a PA (Power Amplifier) as a function of the desired output power level. The dynamic output matching accounts for varying antenna impedance/mismatches to improve PA efficiency and also to enable reconfigurable matching network for a PA to be operable in a multi-band (different center frequencies) radio.

Further power savings are possible if the high-Q μ mechanical filters in the signal path have such low losses that the RF LNA (normally required to boost the received signal against losses and noise from subsequent stages) may no longer be needed. Rather, the RF LNA can

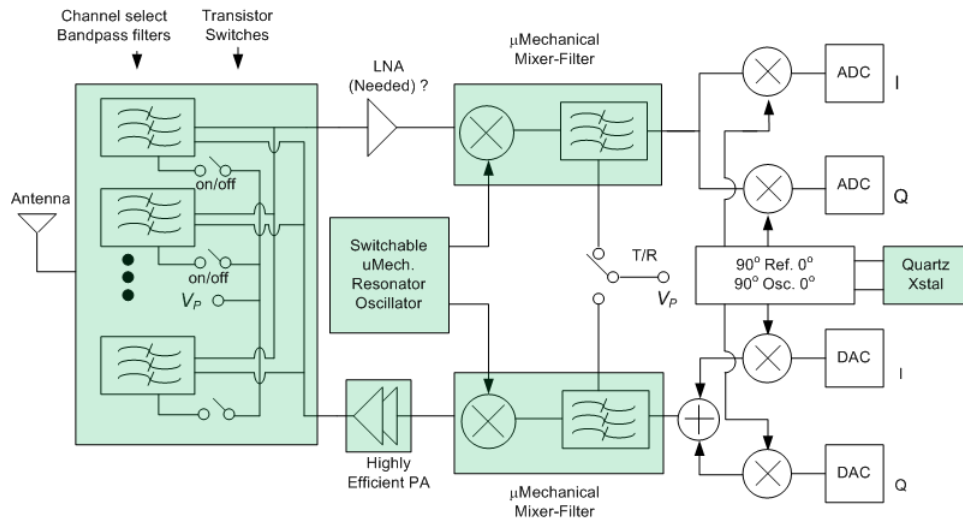


Figure 1.6: System block diagram for a RF channel-select architecture utilizing large numbers of micromechanical resonators in banks to trade Q for power consumption. (On-chip μ mechanics are shaded.)

be removed, and the needed gain to baseband provided instead by an IF LNA that potentially consumes much less power since it operates at the much lower IF frequency. Without the RF LNA or transistor mixer, the receiver front-end architecture reduces to nearly an all-MEMS topology as shown in figure 1.7. In this architecture the channel-selecting filter bank in figure 1.6 has been converted to a mixer-filter bank allowing the use of a single fixed frequency RF local oscillator (LO) to down-convert from RF to IF. Since the RF LO is now a single frequency oscillator, power hungry phase-locking and pre-scaling electronics are not needed. It, however, does so at the cost of a somewhat higher overall noise figure and decreased robustness against hostile interferers. Also, implementing such architectures for receiving wide signal bandwidths for high data rate applications would require a more extensive array of channel select filters/ μ mechanical mixer-filter increasing the area of such filter banks. The size could also potentially increase based on the amount of matching required between the resonators. In the next section, the integration of RF MEMS and CMOS are discussed to enable such systems.

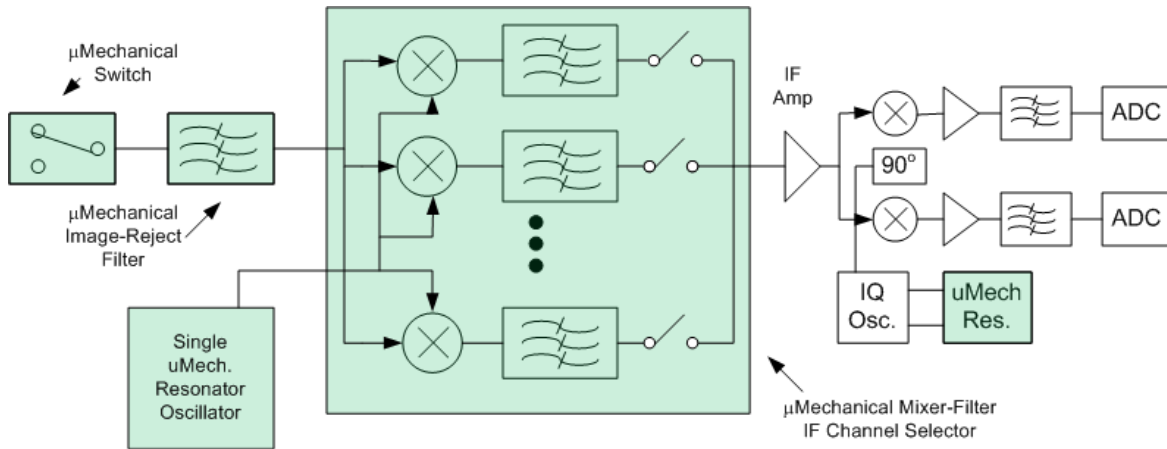


Figure 1.7: System block diagram for an all-MEMS receiver front-end, employing an RF image reject filter, a fixed μ mechanical resonator local oscillator, and a switchable array of IF μ mechanical mixer-filters.)

1.3 CMOS-MEMS Integration

1.3.1 Standard MEMS processing

Most MEMS processing techniques can be classified as either bulk or surface micromachining. Bulk micromachining involves etching features in the bulk material by orientation-independent (isotropic) or orientation-dependent (anisotropic) wet or dry etching techniques (figure 1.8). Surface micromachining (see figure 1.9) usually consists of depositing and patterning of layers of a variety of thin films - including polysilicon, various metals, SiO_2 , Si_3Ni_4 and/or photoresist - on a semiconductor substrate using photolithographic techniques. Some of these films are “sacrificial” in the sense that they are selectively removed in subsequent processing steps, yielding free-standing structures of various shapes [12]. The in-house surface micromachining process shown in figure 1.9 is described in chapter 5 under section 5.2. Another important MEMS processing technique is LIGA, a German acronym for “Lithographie, Galvanoformung, Abformung” which describes a methodology utilizing lithography, electroplating and molding to create high aspect ratio MEMS structures. LIGA was one of the first major techniques to fabricate high-aspect-ratio structures (structures that are much

taller than wide) with lateral precision below one micrometer. In LIGA processing a metallized seed layer is underneath the photoresist structures. This is in contrast to techniques where the conductive layer is over the photoresist. This is because while electroplating the conductive layer at the base of the structures will fill the structures from the bottom up, ensuring good deposition down to the very bottom of deep structures. Conversely if the seed layer is over the photoresist, deep structures may have voids at their base, as the plating deposition tends to plate the top of the structures first. The majority of the processing done in this work is either in-house surface micromachining or LIGA-like processing from a commercially available foundry.

Many MEMS processes have become available to designers as foundry technologies. MEMSCAP's MUMPs (Multi User MEMS Process) is a commercially available MEMS foundry technology. MEMSCAP offers three unique stand-alone, multi-mask MUMPs processes: PolyMUMPs, SOIMUMPs, and MetalMUMPs [1]. MetalMUMPs (figures 1.10 to 1.12) incorporates all three major MEMS processes: LIGA-like, thick metal electroplating, as well as bulk and surface micromachining. Electroplated nickel is used as the primary structural material and electrical interconnect layer. Very tall structures of Nickel, between 18-22 μm , can be built on top of polysilicon and nitride with a deep, KOH-etched trench underneath. Doped polysilicon can be used for resistors, additional mechanical structures, and/or cross-over electrical routing. Silicon nitride is used as an electrical isolation layer. Deposited oxide (PSG) is used for the sacrificial layers. The minimum feature size in MetalMUMPs is 5 μm . Devices that can be made in MetalMUMPs include: relays, magnetic switches, and RF switches and resonators. The design and fabrication of RF switches in MetalMUMPs will be discussed in Chapter 3. A detailed process flow with for MetalMUMPs is given below and shown in figures 1.10 to 1.12:

- (a) A 2 μm thick oxide (Isolation Oxide) is grown on the surface of the starting n-type (100) silicon wafer. This is followed by deposition of a 0.5 μm thick sacrificial phosphosilicate glass (PSG) layer (Oxide 1).

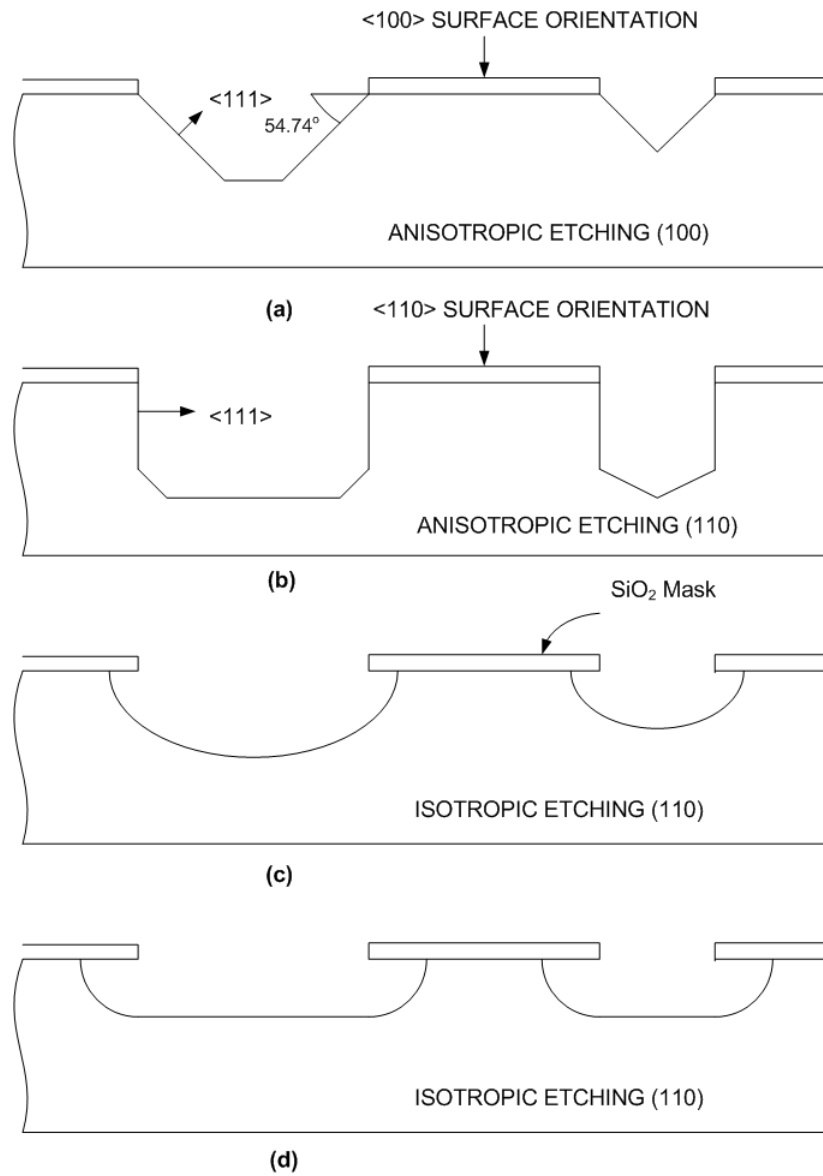


Figure 1.8: Bulk micromachining of Si showing anisotropic (a & b) and isotropic etching (c & d)

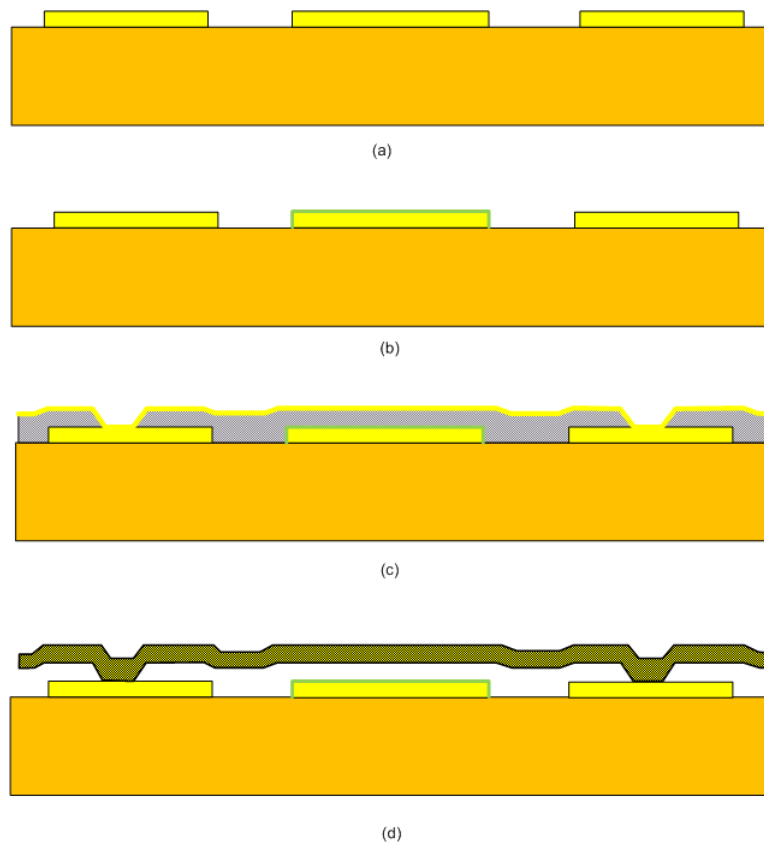


Figure 1.9: Surface micromachining showing lift-off (a), dielectric patterning (b), sacrificial layer patterning (c), electroplating and release of a fixed-fixed beam (d).

- (b) PSG is patterned using photoresist. After the etch, the photoresist is chemically stripped.
- (c) A $0.35\ \mu\text{m}$ layer of silicon nitride (Nitride 1) is deposited, followed immediately by the deposition of a $0.7\ \mu\text{m}$ layer of polysilicon (Poly).
- (d) The wafers are coated with photoresist and the second level (poly) is lithographically patterned. Reactive ion etching (RIE) is used to remove the unwanted polysilicon. After the etch is completed, the photoresist is removed.
- (e) A second $0.35\ \mu\text{m}$ layer of silicon nitride (Nitride 2) is deposited.
- (f) The wafers are coated with photoresist and the third level (NITRHOLE) is lithographically patterned. RIE etching is performed to remove both Nitride 2 and Nitride 1 from the patterned areas. After the etch is complete, the photoresist is removed. Note: Nitride 1 will remain anywhere NITRHOLE is patterned over Poly.
- (g) A second sacrificial layer (Oxide 2), $1.1\ \mu\text{m}$ of PSG, is deposited and annealed at 1050°C for 1 hour.
- (h) The wafer is coated with photoresist and the fourth mask level (METANCH) is lithographically patterned. The Oxide 2 is wet etched and a thin metal layer (Anchor Metal) consisting of $10\ \text{nm Cr} + 25\ \text{nm Pt}$ is deposited. A liftoff process is used to remove the photoresist and leave Anchor Metal only in the bottom of the Oxide 2 openings formed from the METANCH mask level.
- (i) The Plating base layer, consisting of $500\ \text{nm Cu} + 50\ \text{nm Ti}$ is deposited. (Not shown). The wafers are coated with a thick layer of photoresist and patterned with the fifth mask level (METAL). This process forms a patterned stencil for the electroplated Metal layer.
- (j) Nickel is electroplated to a nominal thickness of $20\ \mu\text{m}$ into the patterned resist stencil. A $0.5\ \mu\text{m}$ gold layer is then immediately electroplated on top of the nickel layer. This

forms the Metal layer.

- (k) The photoresist stencil is then chemically removed.
- (l) The wafers are coated with photoresist and patterned with a bloated version of the sixth mask level (GOLDOVP) to remove Plating Base in the regions where Sidewall Metal is desired. The Plating Base is chemically removed from the unpatterned regions, and the photoresist is stripped. The wafers are coated with photoresist and patterned with an un-bloated version of the sixth mask level (GOLDOVP) to define a resist stencil in the regions of Metal where electroplated Sidewall Metal is desired.
- (m) A 1-3 μm gold layer (Sidewall Metal) is electroplated using the GOLDOVP photoresist mask as a stencil.
- (n) The GOLDOVP resist stencil is stripped.
- (o) Plating Base is chemically stripped in the first step of the release process. In the second step of the release process, a 49 % HF solution is used to remove the PSG sacrificial layers (Oxide 1 and Oxide 2) and the Isolation Oxide layer over the trench areas.
- (p) In the final step of the release process, a KOH silicon etch is used to form a 25 μm deep trench in the silicon substrate in the areas defined by the OXIDE1 and NITRHOLE mask levels.

1.3.2 CMOS-MEMS

The benefits of implementing MEMS in various systems motivates their integration with driving, controlling, sensing, signal processing and other associated electronics. This can be achieved by hybrid integration [13, 14, 15] or by monolithic integration [16] (Figure 1.14). In the hybrid approach, the MEMS structures are fabricated on a separate substrate than that of the associated electronics, which is then connected to the electronics by wire bonding

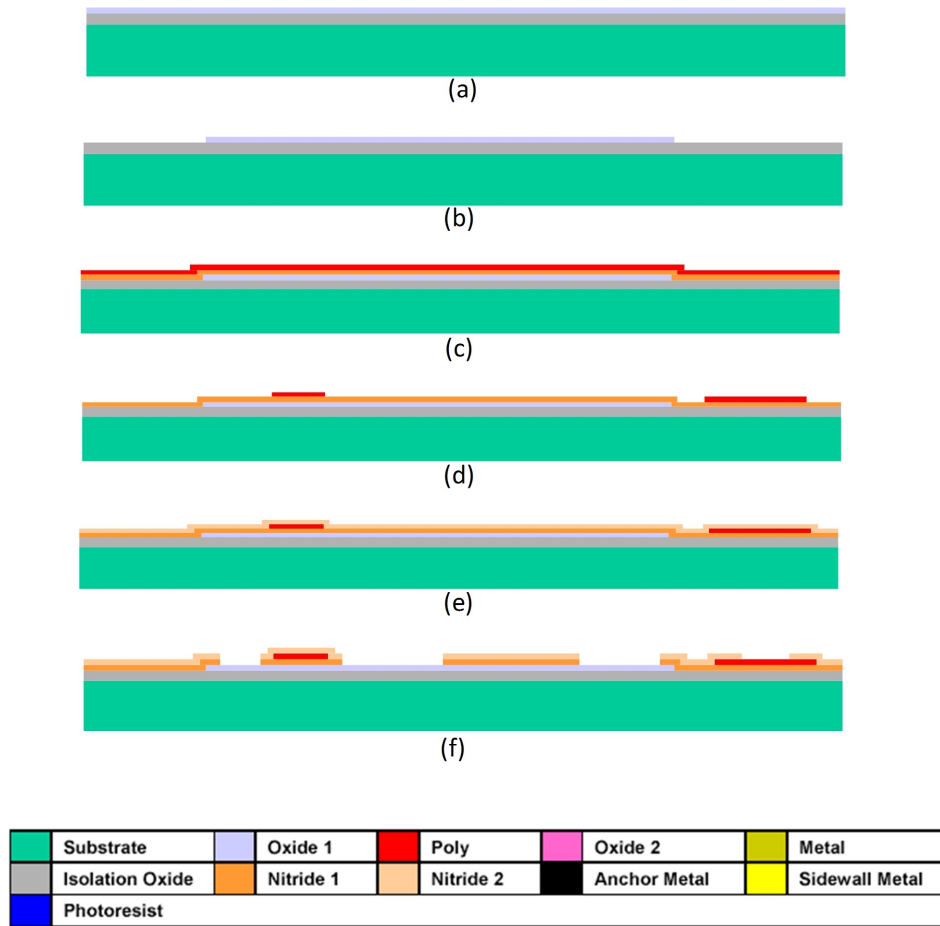
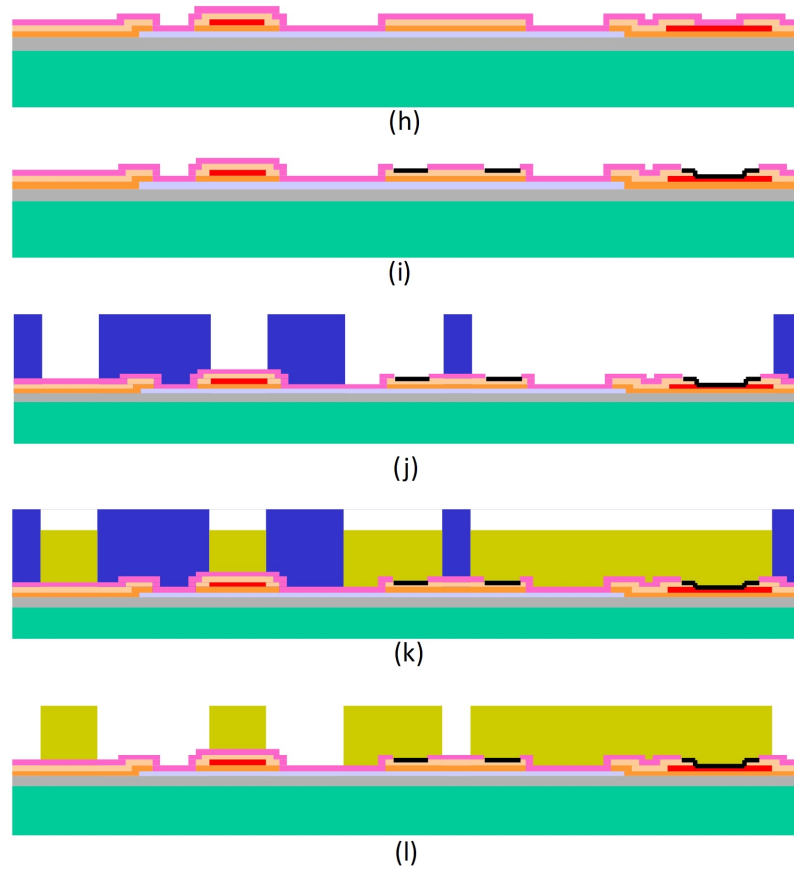


Figure 1.10: MetalMUMPs process flow showing steps (a) - (f) (from [1]).



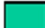
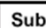
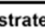


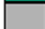
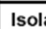
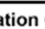
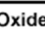


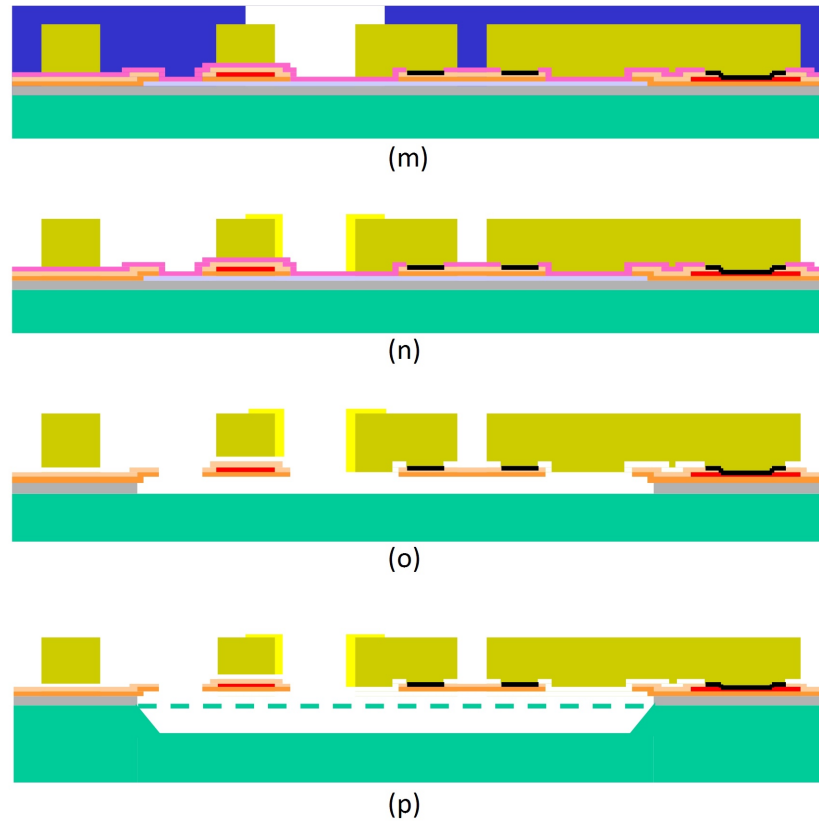
	Substrate		Oxide 1		Poly		Oxide 2		Metal
	Isolation Oxide		Nitride 1		Nitride 2		Anchor Metal		Sidewall Metal
	Photoresist								

Figure 1.11: MetalMUMPs process flow showing steps (h) - (l) (from [1]).





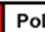
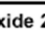
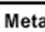


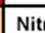
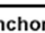
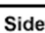

	Substrate		Oxide 1		Poly		Oxide 2		Metal
	Isolation Oxide		Nitride 1		Nitride 2		Anchor Metal		Sidewall Metal
	Photoresist								

Figure 1.12: MetalMUMPs process flow showing steps (m) - (p) (from [1]).

or by flip-chip. Such an approach is modular and, as a consequence, has much shorter development times as compared to the monolithic approach. It also allows for independent optimization of the integrated circuit (IC) and the MEMS technology. There are also no strict limits on the thermal budget for MEMS processing to avoid degradation of the CMOS electronics and interconnects. However, the fill factor is lower due to the relatively large area occupied by the bonding pads, and the assembly and packaging costs are higher in comparison to the monolithic approach. Also, when separate chips are used for MEMS and ICs, performance limiting parasitics are present due to the interconnections between the MEMS and the IC which may have negative impact on the device as well as the system performance particularly in the RF domain. On the other hand, monolithic integration combines MEMS and the associated electronics on the same chip, reducing interconnect parasitics and improving performance. Higher manufacturing yield can potentially lower overall costs as well. Integrating MEMS devices in state-of-the-art CMOS processes, can be done in three general flows:

- processing MEMS first and electronics last, typically adjacent to the sensors [17];
- processing the electronics first and the MEMS last [18, 19, 20], typically above the circuitry;
- interleaving the fabrication of both [21].

Both MEMS first and interleaved processing introduce significant changes to the standard CMOS process flow, and hence, the integration becomes more complicated and expensive. The MEMS last method is probably the most promising way for integrating MEMS devices, as it allows the use of standard CMOS processes and fairly independent optimization of the CMOS and MEMS devices. MEMS last also, in principle, allows scaling of CMOS technology without affecting the MEMS device design. The main constraint imposed by post-processing is that the maximum fabrication temperature for MEMS devices should not introduce any damage or degradation in the underlying electronics or interconnects. This

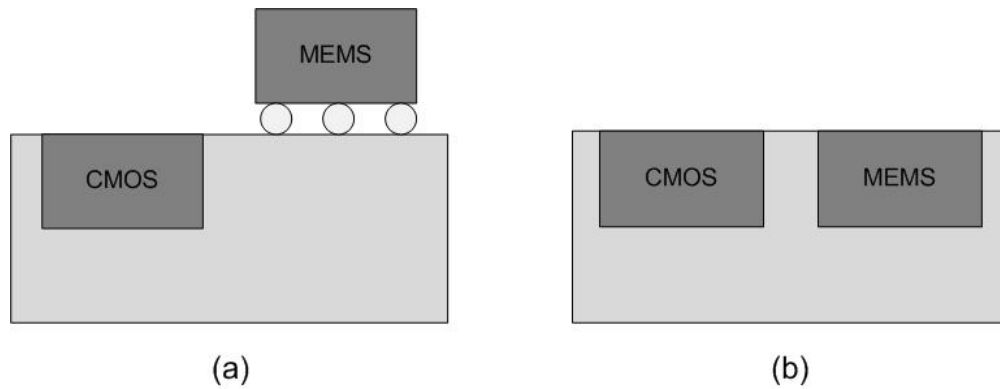


Figure 1.13: Hybrid approach (a) versus monolithic integration (b) of MEMS and CMOS, after [22]

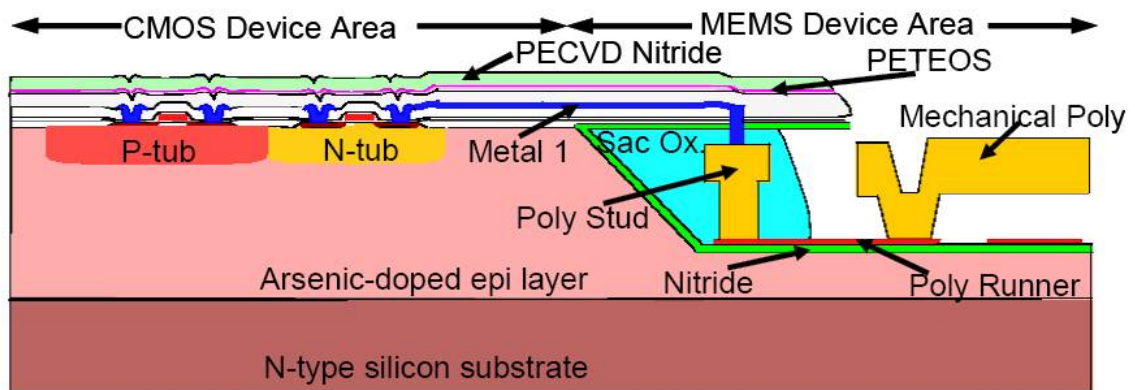


Figure 1.14: Cross-section schematic of an iMEMS process from Sandia, Copyright 1996 IEEE [17]

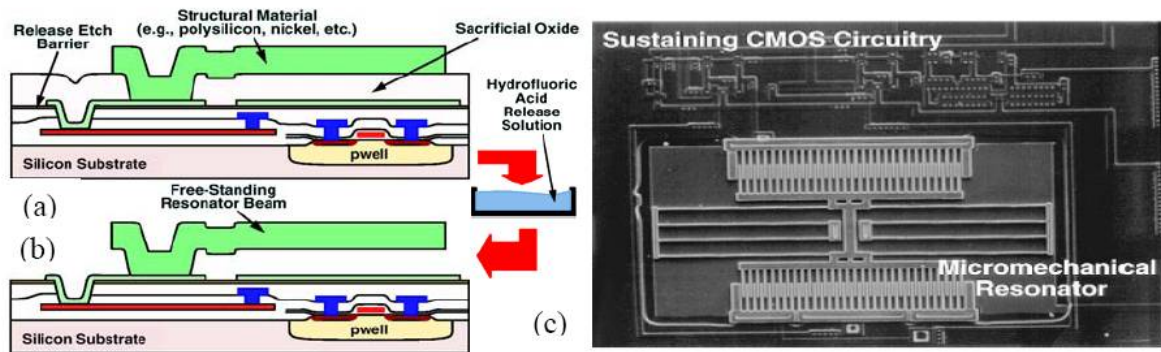


Figure 1.15: Cross-sections (a) immediately before and (b) after release in a surface-micromachining process done directly over CMOS. (c) SEM of the 16.5-kHz CMOS μ mechanical oscillator, Copyright IEEE 1999 [20].

temperature constraint is quite strict for post-processing surface micromachined MEMS, as it might affect relevant physical properties such as polycrystallinity, growth rate, mechanical properties, dopant activation and electrical resistivity. The temperature requirements for depositing most of the metals and dielectrics over CMOS electronics can be accomplished within the thermal budget ($\leq 450^\circ\text{C}$), but Poly-Si requires higher deposition temperature. A promising alternative is the use Poly-SiGe instead of Poly-Si. Poly-SiGe provides the necessary mechanical properties and reliability at a significantly lower temperature compared to conventional poly-Si (i.e. depositing temperature of $\leq 450^\circ\text{C}$ instead of $\geq 800^\circ\text{C}$) [23]. Meanwhile, metal-based MEMS structures, especially switches can also be easily fabricated using a post-CMOS approach.

However, metals are a less attractive choice for high-Q high frequency resonators as the internal dissipation of metals is higher than that of crystalline or poly-crystalline semiconductor materials. Another key process step in MEMS-CMOS integration or stand alone MEMS processing is the packaging of MEMS devices.

1.4 Dissertation Overview

This chapter has introduced the motivations and challenges associated with a single chip reconfigurable wireless transceiver and introduced RF-MEMS as an enabling technology towards that end. The main objectives of this dissertation are to understand and exploit the non-linearities existing in an electrostatically actuated MEMS systems such as switches and resonators. In switches they are used to reduce the actuation voltages and in resonators to improve their phase noise performance. Chapter 2 will provide detail background on RF-MEMS devices such as switches and resonators. Both lateral (series) and vertical (shunt) topologies are discussed briefly along with their electrical models and limitations. An analytical model is developed for the lateral switch accounting for various process non-idealities in Chapter 3. Dynamic (resonant) pull-in of electrostatic lateral (contact) type and shunt (capacitive) switches are modeled and demonstrated in Chapter 4 and 5. A non-linear analytical model for a transversely vibrating microbeam resonator is adopted and the influence of non-linearities on the phase noise performance of the resonators are studied in Chapter 6.

- **Chapter 2** presents basic background and modeling of RF-MEMS switches and resonators. Various switch topologies are presented and MEMS series switches (metal-to-metal contact) and shunt capacitive switches are discussed in some detail. The performance of the state of the art RF-MEMS switches and their challenges are summarized. Linear and a non-linear models of the resonator are presented discussing the influence of non-linearities on its phase noise performance.
- **Chapter 3** focuses on the mechanical modeling of a metal-metal contact variable gap lateral RF MEMS switch. An analytical model for a variable gap contact switch that accounts for the process non-idealities has been developed in this chapter. The process non-idealities considered are the trapezoidal cross-sections for electrodes and springs (instead of rectangular) and the droop in the switch carriage and fixed electrodes along their length due to gradients of in-plane stress thru the thickness of the released layer

combined with the conductor plane underneath the switch. The model also accounts for electrostatic fringing fields as a function of the moving gap. Analytical expressions of inclined capacitances, generated electrostatic forces, travel distances before pull-in, spring constants and eventually pull-in voltages are compared with FEA model.

- **Chapter 4** presents the experimental results for dynamic (or resonant) pull-in phenomenon as an actuation method for a variable gap lateral contact RF MEMS switch. The use of the resonant pull-in technique reduces the overall pull-in voltage $V_{DP}(= \sqrt{V_{DC}^2 + \frac{v_{ac}^2}{2}}) < V_{SP}(= V_{DC})$ required to actuate the switch. The reduction in actuation voltage can be greatly enhanced by operating at the optimal non-linear resonant frequency. There are three distinct regions of operations of the lateral switch based on the applied voltages and available travel distances. Finally, the timing response for resonant pull-in is investigated.
- **Chapter 5** reports the design, fabrication and experimental results for a capacitive MEMS shunt switch that employs Resonant Pull-in ($V_{DP}(= \sqrt{V_{DC}^2 + \frac{v_{ac}^2}{2}}) < V_{SP}(= V_{DC})$) as an actuation method. Dynamic pull-in V_{DP} is significantly lower than static pull-in voltage ($V_{SP} = V_{DC}$) that is traditionally used for actuation. The reduction in actuation voltage can be enhanced by operating at the correct nonlinear resonance frequency. To address the high switching times in dynamic pull-in, two switching methods are proposed and simulated switching times are compared to static switching times.
- **Chapter 6** studies the influence of V_{DC} over the effective non-linearity (S) on the resonators and the effect of S on resonators closed loop phase noise performance. First the resonator's periodic response (displacement) is defined by a set of two first-order nonlinear ordinary differential equations that describe the modulation of amplitude and phase of the resonators response as a function of forcing function, damping and the effective non-linearity of the system (S). The phase, frequency, amplitude, forcing and non-linearity S are mapped to each other through the modulation equations and

can be determined for a given phase. The best case resonator phase that maximises Q which leads to better phase noise performance is determined. Two major aliasing schemes were analyzed and was shown that the capacitive force non-linearity is the major source of mixing that causes the up-conversion of $1/f$ frequency into signal sidebands.

- **Chapter 7** summarizes the results and highlights the major conclusions and contributions from this work. Finally, some recommendations for future work are made based on the knowledge gained in this research.

Chapter 2

MEMS Switches and Resonators

Chapter 1 discussed the potential for RF-MEMS as an enabling technology in developing low-power, low cost, miniaturized, reconfigurable RF systems. This chapter focuses further on two of the most important RF MEMS devices: **Switches and Resonators**. The first section discuss the potential strengths and concerns of MEMS switches and then elaborates on series (metal-contact type) and shunt switches (capacitive type). The phenomenon of static pull-in instability for electrostatic MEMS switches is explained, followed by *resonant or dynamic pull-in* where the switch is driven to instability by actuating it at its resonant frequency using a combination of AC and DC signals. With respect to RF MEMS resonators, linear and non-linear models are introduced in the second section with discussions on how the non-linearities can influence phase noise performance. The section concludes with some of the challenges faced by Si based MEMS resonators for timing applications.

2.1 MEMS switches

RF MEMS switch development has seen tremendous growth in the past 10 years due to its potential for commercial and defense applications. RF MEMS switches offer substantial

performance advantages compared to p-i-n or field-effect transistor (FET) diode switches [24]. RF MEMS devices have been proposed for use in phased arrays and reconfigurable apertures for defense and telecommunication systems, switching networks for satellite communications, and switches for wireless applications (portable units and base stations). Several known advantages of RF MEMS are as follows [25]:

- Extremely low loss ($\leq 0.1-0.2$ dB), low on-resistance ($\leq 0.2 - 2 \Omega$ for metal-contact devices, $0.1 - 2 \Omega$ for capacitive devices), low off-state capacitance (2-16 fF), very high isolation up to mm-wave frequencies, and near zero-power consumption for electrostatic and PZT (Piezoelectric-based) switches and varactors.
- Very High Q: A device resistance of $0.1 - 2 \Omega$ results in a Q greater than 50 - 400 at 2 - 100 GHz. This is essential for tunable filters.
- Very high linearity: For identical input powers, RF MEMS IIP_3 are 20-50 dB better than GaAs or CMOS devices, especially when compared to varactors.
- High Power Handling: Capable of handling 1 - 10 Watts for both capacitive and metal-contact switches and varactors [26].
- Can be designed to handle large RF voltage swings ($> 30-50 V_{rms}$). Can be designed as a three or four-terminal device where the RF terminals are independent from the dc actuation pads [26], [27].

However, RF MEMS switches also have some significant concerns :

- Relatively Low Speed: The switching speed of most MEMS switches is around 2-40 μs . Certain communication and radar systems require much faster switches.
- High-Voltage Drive: Most reliable RF MEMS switches operate at 25 - 90 V, and therefore require high-voltage drive circuits.

- Hermetic Packaging: MEMS switches need to be packaged in inert atmospheres (nitrogen, argon, etc.) and in very low humidity, resulting the need for hermetic or near-hermetic seals. Hermetic packages are needed to preserve contact cleanliness (DC contact switches) and to reduce the effect of dielectric charging (capacitive switches) over the switch lifetime and also to protect the switches from dust and debris which may otherwise interfere with the proper functioning of the device. Such packaging tends to increase the cost but several companies and labs have developed hermetic batch fabricated wafer-caps which will greatly reduce packaging cost.
- Reliability: Research on reliability is a very high priority, and better dielectrics, metal-contacts, actuator design and packaging are all contributing to vastly improved reliability results.

RF MEMS switches can be classified according to:

- Actuation Mechanism: electrical, thermal, magnetostatic or piezoelectric
- Contact type: metal-to-metal or capacitive
- Travel Direction: vertical or lateral
- Circuit Configuration: series or shunt

Among the actuation methods, electrostatic actuation is the most prevalent technique due to its virtually zero power consumption, relatively short switching time, 100s of μN of achievable contact forces and relatively simple biasing. However, in most cases, electrostatic actuation requires voltages in the range of 30-80 V, and this requires high-voltage drive circuits. The type of contact determines if the device can be used as switch or a varactor. Typically metal-to-metal (DC) contact switches act as switching devices and perform well from DC to 100 GHz since they have better insertion loss at low frequencies. At high frequencies the isolation of the switch goes down since it is inversely proportional to the up-state capacitance

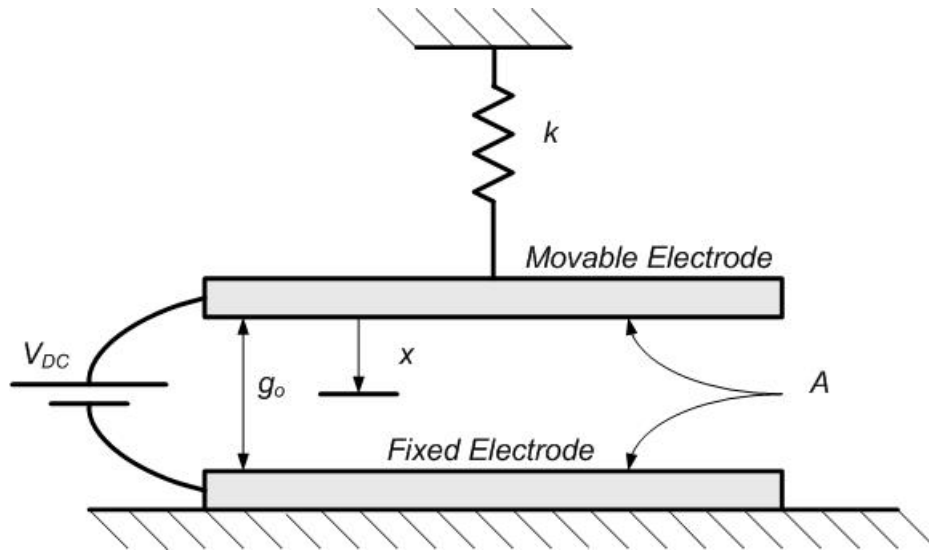


Figure 2.1: 1-D MEMS Switch model.

and the frequency of operation. The capacitive shunt switches typically operate well from 2 GHz to greater than 100 GHz since their insertion loss is better at higher frequencies. Most metal-to-metal contact types switches are series switches, while capacitive switches (varactors) are normally implemented in the shunt configuration. Sections 2.1.2 and 2.1.3 will present basic electrical modeling of shunt and series switches.

2.1.1 Electrostatic Actuation

Figure 2.1 shows a MEMS switch modeled as a parallel plate capacitor with a movable top plate and a fixed bottom plate separated by gap g_0 and an overlap area A . The mechanical part of the microactuator is modeled as a spring-mass-damper system as given in equation 2.1:

$$m\ddot{x} + \gamma\dot{x} + kx = F_e, \quad (2.1)$$

where $F_e = \frac{1}{2} \frac{\epsilon_0 A V_{DC}^2}{(g_0 - x)^2}$ is the electrostatic pull-down force exerted on the movable plate by the applied voltage V_{DC} , k is the mechanical spring constant, γ is the damping factor, m is the

equivalent mass of the movable plate, and x is the deflection of the plate as indicated in figure 2.1.

To derive the expression for pull-in, the total potential energy in system is first written as

$$E_{total} = -\frac{1}{2} \frac{\epsilon_o A V_{dc}^2}{g_o - x} + \frac{1}{2} k x^2 \quad (2.2)$$

where the first term is the electrostatic potential (F_e) and the second term is due to the mechanical energy stored in the spring. The force acting on the movable plate is obtained by differentiating equation 2.2:

$$F_{total} = -\frac{\partial E}{\partial x} = \frac{1}{2} \frac{\epsilon_o A}{(g_o - x)^2} V_{dc}^2 - k \quad (2.3)$$

At static equilibrium, the electrostatic force equals the spring force ($F_{total} = 0$) and equation 2.3 becomes

$$kx = F_e = \frac{1}{2} \frac{\epsilon_o A}{(g_o - x)^2} V_{DC}^2. \quad (2.4)$$

Equation 2.4 can be solved for the equilibrium position x as a function of applied voltage V_{DC} as shown in figure 2.2. Above the pull-in voltage V_{SP} equation 2.4 has no solutions. The solutions above pull-in displacement are shown to be unstable in the following discussion.

A simple expression for the pull-in point is obtained by differentiating equation 2.3 to obtain the stiffness of the system:

$$\frac{\partial F}{\partial x} = \frac{\epsilon_o A}{(g_o - x)^3} V_{DC}^2 - k. \quad (2.5)$$

Substituting equation 2.4 in to equation 2.5 gives stiffness around the equilibrium point:

$$\frac{\partial F}{\partial x} = \frac{2kx}{(g_o - x)} - k. \quad (2.6)$$

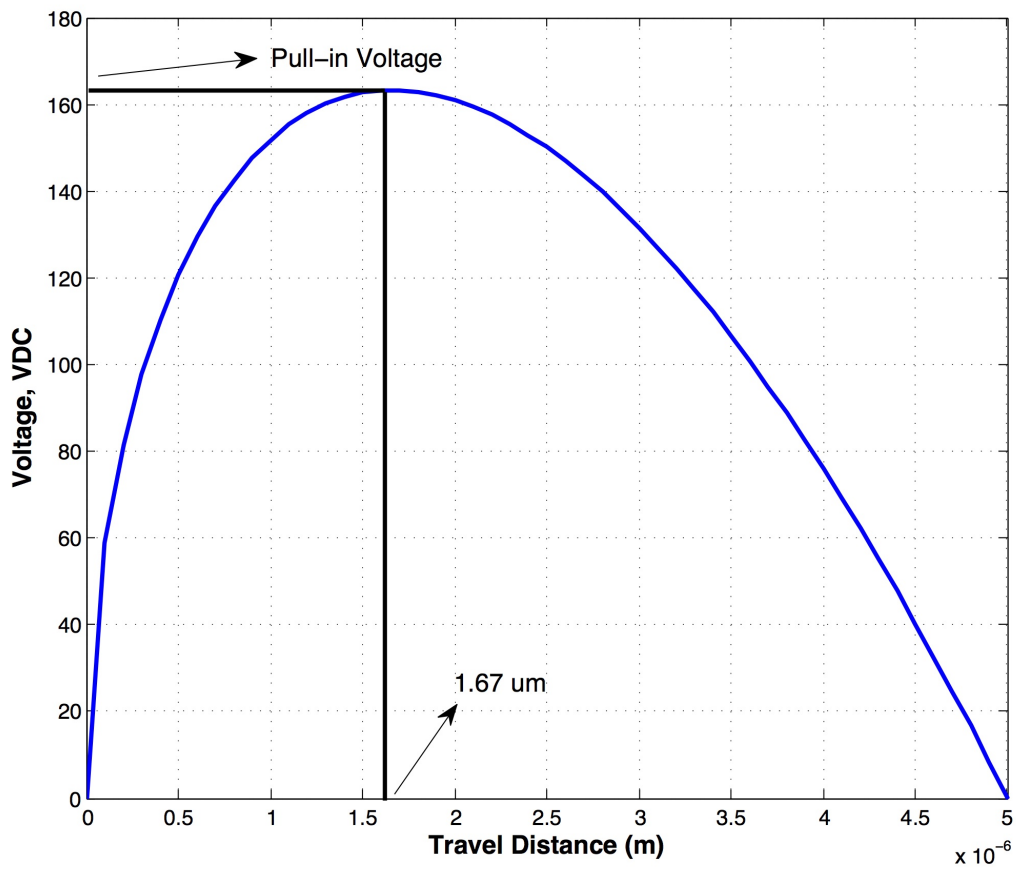


Figure 2.2: Equilibrium relationship between plate displacement and applied voltage.

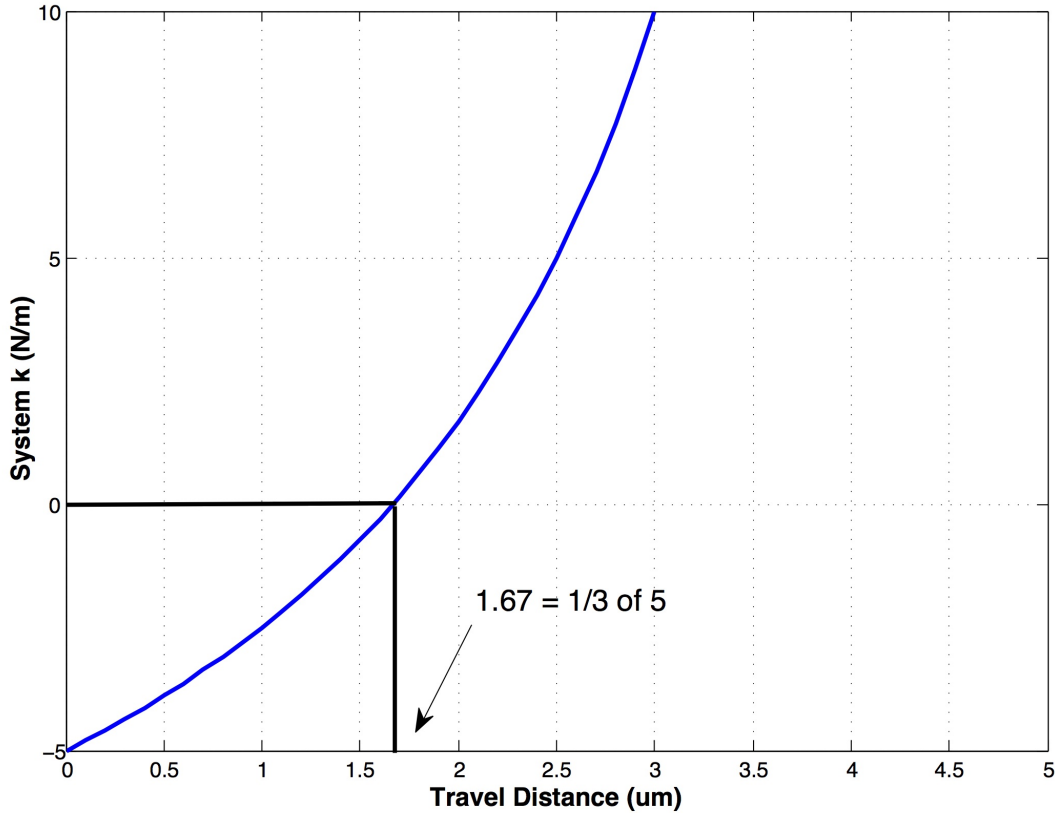


Figure 2.3: The total stiffness as a function of displacement. The simulations shown are for a switch with a gap of $5 \mu\text{m}$. Positive stiffness indicates unstable equilibrium point.

With no applied voltage, equation 2.6 is simply $\frac{\partial F}{\partial x} = -k$; a small positive movement ∂x results in negative force $\frac{\partial F}{\partial x} \partial x = -k \partial x$. Increasing the bias voltage V_{DC} makes the stiffness less negative. The unstable point is given by $\frac{\partial F}{\partial x} = 0$ giving

$$x = \frac{1}{3}g_o. \quad (2.7)$$

Beyond this point the stiffness becomes positive as shown in figure 2.3 and the system is unstable. Even a small positive movement ∂x results in positive force that increase with x .

Substituting equation 2.7 into equation 2.4 gives the static pull-in voltage V_{SP} at which the system becomes unstable

$$V_{DC} = V_{SP} = \sqrt{\frac{8k}{27\epsilon_o A g_o^3}}. \quad (2.8)$$

However, the static analysis of pull-in instability shown above is no longer valid when the applied voltage is a combination of V_{DC} and a time varying sinusoid $v_{ac} \cos(\Omega t)$, where the excitation frequency Ω is close to the natural resonant frequency of the switch. Such an actuation mechanism is called *resonant* or *dynamic pull-in*, because the switch is actuated by resonating it first. Chapters 4 and 5 elaborate on the resonant pull-in phenomenon of metal contact type lateral and capacitive shunt MEMS switches respectively. The frequency response of electrostatic MEMS switches is non-linear due to the presence of cubic and quadratic spring non-linearities that have both mechanical (mid-plane stretching in the case of shunt switch) and electrical (due to electrostatic forcing) origins. The next subsection discusses the two topologies of MEMS switches that have been investigated in this dissertation and presents some basic electrical modeling.

2.1.2 MEMS Series Switches

MEMS series switches can be grouped into two categories: the broadside series switch and the inline series switch, as shown in figure 2.4. The main difference between the two designs is that in the inline switch the RF signal and DC actuation act on the same (actuator) arm whereas in the broadside switch the actuation arm is separated from signal line. As a result, inline switches must be completely fabricated using a low-loss metal layer (Au, Al, Pt, etc.). On the other hand, only the contact portion of the broad-side switch needs to be fabricated using a low-loss metal structure and the actuation portion can be composed of dielectric-only or a dielectric/metal cantilever, or a fixed-fixed beam. DC-contact, laterally actuated type switches also belong in the category of broadside type of metal series switches. In Chapter

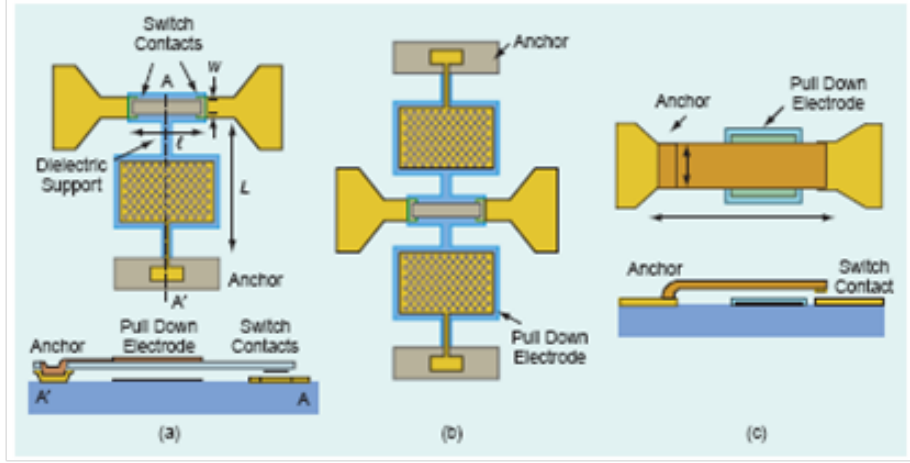


Figure 2.4: Switch Classification: Broadside MEMS-series switches with (a) one electrode, (b) two electrodes, and (c) in-line MEMS-series switches, Copyright 2001 IEEE [28]

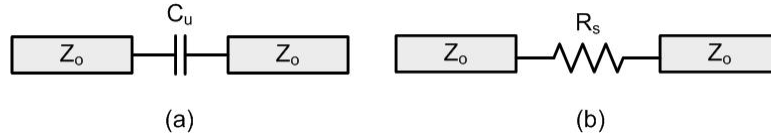


Figure 2.5: Equivalent Electrical model (a) Switch open (b) Switch closed.

3 a variable gap laterally actuated DC-contact type MEMS switch design will be presented.

The electrical model of a MEMS series switch is basically a series capacitance in the open state and a small resistance in the closed state as shown in figure 2.5. The isolation of a series switch in the open state is given by [28]

$$|S_{21}|_{open}^2 = 4\omega^2 C_u^2 Z_o^2, \quad (2.9)$$

where C_u is the open-state up-state capacitance and Z_o is the transmission line impedance.

The insertion loss of the switch in the closed state given by [28]

$$|S_{21}|_{closed}^2 = 1 - R_s/Z_o, \quad (2.10)$$

where R_s is the contact resistance of the switch.

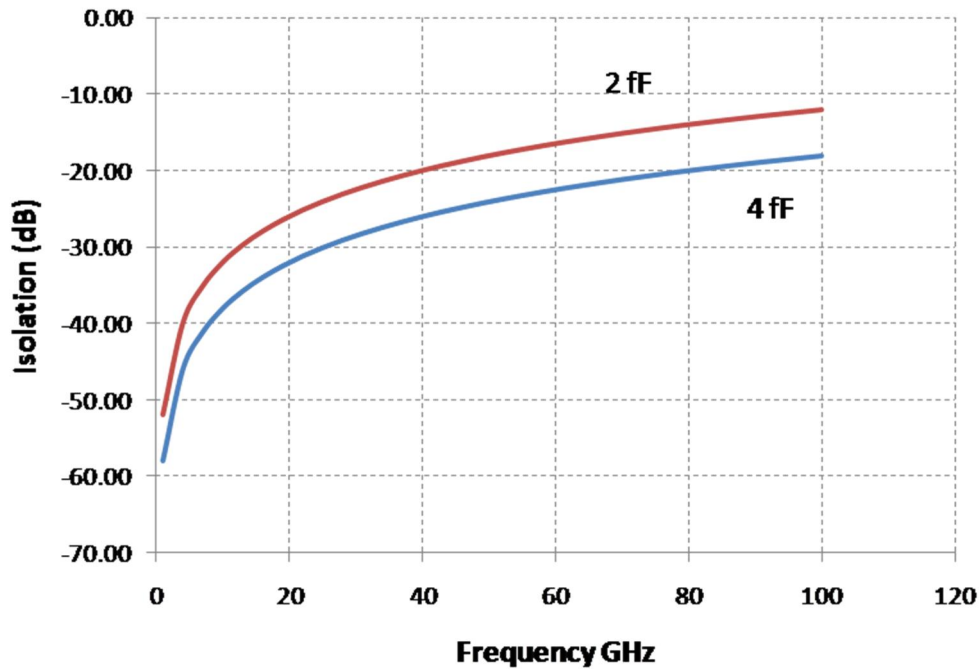


Figure 2.6: Plot showing switch isolation for different open-state capacitances.

It can be seen that an up-state capacitance of 2-4 fF and a contact resistance of 1Ω results in an isolation of -46 to -40 dB at 4 GHz (see figure 2.6) and a -0.1 dB (see figure 2.7) of loss, respectively. At higher frequencies the isolation degrades as shown. However, this represents excellent performance for wireless applications (0.1-10 GHz) with high isolation typically not attained by solid-state devices.

2.1.3 MEMS Capacitive Shunt Switches

Capacitive shunt switches are typically based on a fixed-fixed metal beam design typically anchored to coplanar-waveguide ground planes and therefore electrically at ground potential (figure 2.8a). A thin dielectric layer (silicon dioxide or silicon nitride), also known as the anti-stiction layer, is used to isolate the switch from the pull-down electrode. In this case, the signal line of the coplanar waveguide provides both the electrostatic actuation and the RF capacitance between the transmission line and the switch beam (at ground). When

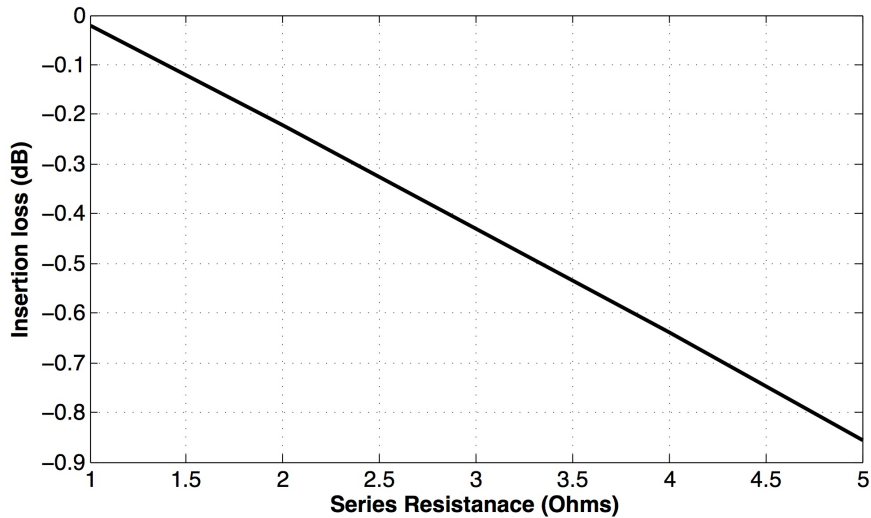


Figure 2.7: Plot showing switch insertion loss for different series contact resistances.

the switch is in the up-state position, it should provide a low capacitance to ground, and have little effect on the impedance of the transmission line. When the switch is actuated in the down-state position, the capacitance to ground increases significantly resulting in an RF short circuit (reflection) and good isolation at microwave frequencies (10 GHz and above). The capacitance ratio (C_d/C_u) is around 40-100 for most published designs. The electrical equivalent circuit is shown in figure 2.8b. The up-state reflection coefficient of a shunt-capacitive switch is given by [28]

$$|S_{11}|_{up}^2 = \omega^2 C_u^2 Z_o^2 / 4, \quad (2.11)$$

where C_u is the upstate capacitance and Z_o is the transmission line impedance.

The down-state isolation (S_{21}) is given by [28]

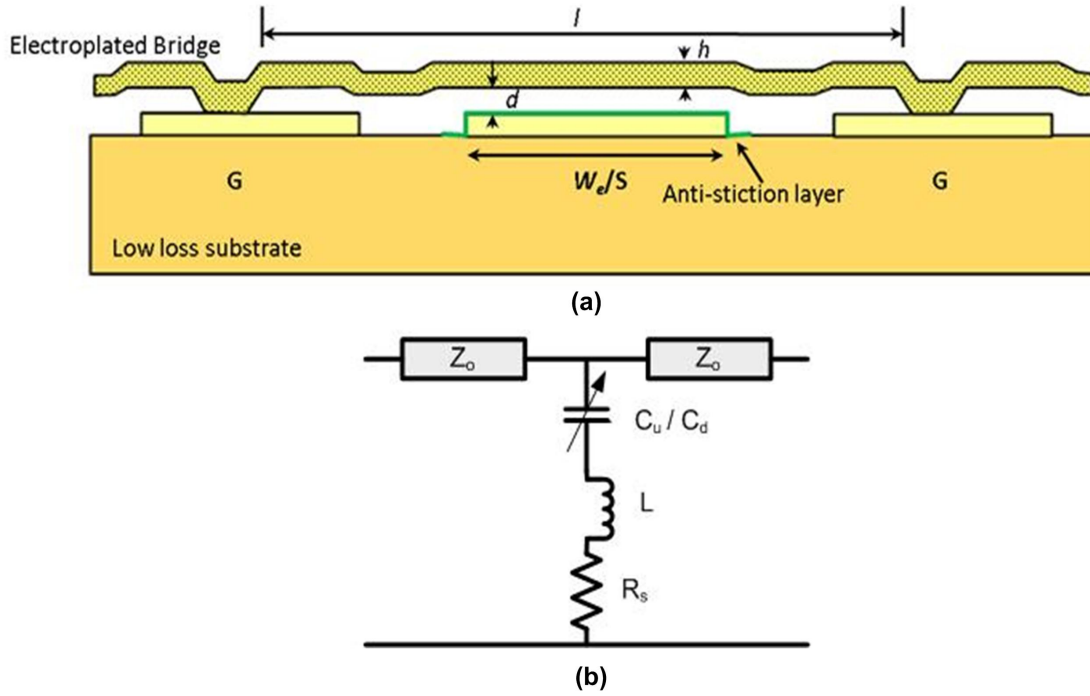


Figure 2.8: Side view of a Shunt Capacitive Switch and its electrical equivalent circuit model

$$\begin{aligned}
 |S_{21}|_{down}^2 &= 4/\omega^2 C_d^2 Z_o^2 \text{ for } f \ll f_o \\
 &= 4R_s^2/Z_o^2 \text{ for } f = f_o \\
 &= 4\omega^2 L^2/Z_o^2 \text{ for } f \gg f_o
 \end{aligned} \tag{2.12}$$

where

$$f_o = 1/(2\pi\sqrt{LC_d}) \tag{2.13}$$

is the down-state resonant frequency of the capacitive switch. Finally, tables 2.1 and 2.2 summarize the performance and reliability of state of the art RF MEMS metal-contact switches, capacitive switches and switched capacitors respectively.

Parameter	RADANT [29]	RFMD [30]	XCOM	OMRON [31]
Actuator Type	Cantilever	Cantilever	Cantilever	Bridge
Actuator Metal	Au	Au	Au	Au
Substrate	Silicon	SOI (CMOS)	Silicon	Silicon
Actuation Voltage (v)	90	90	90	10-20
Switching Speed (μ s)	10	5	30	300
Metal contact R_s (series)(Ω)	4 (2-contact)	1	1	0.5
Package Type	Hermetic Wafer cap	Hermetic Dielectric Cap	Ceramic Hermetic Cap	Wafer package, glass frit
Reliability	>200B at 20 dBm, >1000B at 20 dBm, >10B at 30 dBm, 100B at 30 dBm, 10B at 40 dBm, >200B at 40 dBm	100M - 1000M at 10 dBm	100M-1000M at 10 dBm	100M at 1 mA, 10M at 10 mA

Table 2.1: Reliability and performance summary of RF MEMS metal-contact switches, from 2008.

2.2 MEMS Resonators

In this section, electromechanical modeling of MEMS resonators is presented. Vibrating MEMS are micromachined mechanical structures that vibrate at natural resonant frequencies related to vibration modes induced by external excitations. The external excitations of MEMS resonators can be electrostatic, piezoelectric, laser or magnetic. The most common means of excitation is electrostatic since the capacitive transduction of these devices have inherent advantages. Electrostatic excitation offers easy to draw geometries with CAD-definable frequencies, voltage-controlled reconfigurability and frequency tunability, and finally material compatibility with integrated circuit manufacturing. The other actuation mechanisms lack many of these advantages because the required force is not generated in as simple a manner as applying a voltage across electrodes. Piezoelectric actuation has some similar attributes as the electrostatic actuation but historically has lacked material compatibility with integrated circuit manufacturing.

Parameter	MTT-LL [32]	Raytheon [33]	MEMtronics [34]	Wispry	UCSD [35]	UCSD [36]	LIMOGES [37]
Actuator Type	Cantilever	Bridge	Bridge	Cantilever	Cantilever	Bridge	Cantilever
Actuator Material	Al	Al	Al	Al	Au	Au	Au
Substrate	Silicon	Silicon, Alumina, GaAs, Quartz	Quartz, Glass	Silicon (on CMOS)	Fused Silica	Fused Silica	Fused Silica
Actuation Voltage (V)	55-65	30-40	25-40	35(3V on-chip)	30-40	30-40	60
Switching Speed (μ s)	20	5	10	< 100	0.8,50	1	10-20
Capacitance Ratio	150:1	50:1	10:1-20:1	5-7:1	4-5:1	9:1	
Package Type	Hermetic Wafer cap	Hermetic Wafer cap	Wafer Level Liquid	Thin-film Semihhermetic Wafer Cap	Unpackaged	Unpackaged	Unpackaged
Reliability	≥ 600 B at 0 dBm	≥ 200 B at 20 dBm, ≥ 150 B at 20 dBm, ≥ 100 B at 10 dBm	≥ 100 B at 20 dBm	N/A	2B at 30 dBm, 100B at 30 dBm	≥ 20 B at 20 dBm, ≥ 5 B at 27 dBm	≥ 1 B at 10 dBm, ≥ 20 B at 10 dBm, ≥ 2 B at 33 dBm

Table 2.2: Reliability and performance summary of RF MEMS capacitive switches and switched-capacitors, from 2008.

MEMS resonators targeting oscillator applications ranging from low kHz to GHz in frequency have been published extensively in the literature. The resonator designs can be categorized based on the modes of vibration:

- Flexural mode
 - Folded Beam
 - Clamped-Clamped Beam
 - Free-Free Beam
- Bulk acoustic mode
 - Disk Resonators (contour and wineglass modes)
 - Square/BAW (length, width extentional mode) Resonators
 - Ring Resonators

Typically flexural mode resonators operate at frequencies less than 100 MHz due to the limitations in mechanical stiffness. Bulk acoustic mode resonators are better suited for frequencies above 100 MHz. Table 2.3 illustrates the state of the art resonators and their frequency ranges. In the next two subsections, a linear model of the resonator is reviewed, followed by the analysis of the non-linear model and how non-linearities influence the phase noise performance of the resonator.

2.2.1 Linear Resonator Model

The mechanical vibrations of the resonator can be modeled with a lumped mass-spring-dashpot system as seen in figure 2.9, for which the lumped mass and spring parameters can be derived from the resonator geometry and mode-shape. The coupling to the resonator is provided by the electrostatic transduction over the narrow gap d . The equation of motion for forced oscillations can be written as:

Resonator Structure	Freq Range	Applications	State-of-Art
Comb-drive	1 kHz to 1 MHz	Real Time Clock	Res: $Q \sim 80$ k, $TC_f \sim 2.5$ ppm/ $^{\circ}C$ Osc: 16 & 32kHz, 78 kHz Ni, 1 MHz poly-Si Pkg: Wafer-level vacuum
Clamped Clamped Beam	1 MHz to 100 MHz	Reference Osc.	Res: $Q \sim 4$ k @ 10MHz, $TC_f \sim 0.24$ ppm/ $^{\circ}C$ Osc: 10MHz, OK phase noise (P.N.) Pkg: Wafer-level vacuum
Fixed Fixed Beam	10 MHz to 100 MHz	Reference Osc.	Res: $Q > 10$ k for $f < 100$ MHz Osc: 13MHz, met GSM spec.
Square	10 MHz to 500 MHz	Reference Osc., RF Oscillators	Res: SOI: $Q \sim 130$ k @ 13 MHz. Osc: 13MHz, met GSM spec.
Disk/Wineglass (WG)	20 MHz to 1.5 GHz	Reference Osc., RF Oscillators	Res: $Q \sim 11$ k @ 1.5GHz, $Q \sim 98$ k @ 60MHz Osc: 60MHz, few dB short of GSM spec. Pkg: Wafer-level vacuum
Ring/Square AlN	100 MHz to 5 GHz	RF Oscillators	Res: $Q \sim 2$ k from 200MHz to 656MHz with low impedance.
Ext. WG/Hollow	100 MHz to 5 MHz	RF Oscillators	Res: Hollow: $Q \sim 14$ k @ 1.2 GHz Res: Ext. WG: $Q \sim 2.3$ k @ 1.47 GHz
FBAR	1 GHz to 5 GHz	RF Oscillators	Res: $Q \sim 2$ k @ 1.9 GHz Osc: 1.98GHz, P.N. -112dBc/Hz, 10kHz away from carrier

Table 2.3: Micromechanical Resonators and their applications over the frequency from 2008, after [38]

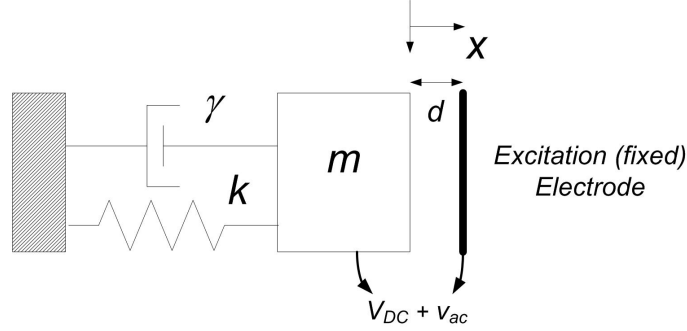


Figure 2.9: Mechanical lumped model for the resonator.

$$m\ddot{x} + c\dot{x} + kx = F_e, \quad (2.14)$$

where m is the lumped mass, c is the damping co-efficient, F_e is the electrostatic force actuating the resonator, and k is the mechanical spring constant. We define the natural frequency $\omega_o = \sqrt{\frac{k}{m}}$ and the mechanical quality factor $Q_m = \omega_o m / c$. The resonator displacement x due to the force F_e is given by [39]:

$$x = H(\omega)F_e, \quad (2.15)$$

where the force-displacement function $H(\omega)$ from equation 2.14 is:

$$H(\omega) = \frac{k^{-1}}{1 - \omega^2/\omega_o^2 + j\omega/Q_m\omega_o}. \quad (2.16)$$

The electrostatic force actuating the resonator is:

$$F_e = \frac{1}{2} \frac{\partial C}{\partial x} (V_{DC} + v_{ac}(t))^2, \quad (2.17)$$

where V_{DC} is the DC bias voltage over the gap, v_{ac} is the AC excitation voltage, and

$$C = \epsilon_o \frac{A}{d - x}, \quad (2.18)$$

is the transducer working capacitance that depends on electrode area A , and the nominal working electrode gap d . The current through the sense electrode is given by

$$i_{sig} = \frac{\partial C(V_{DC} + v_{ac})}{\partial t} \approx \frac{\partial C}{\partial t} V_{DC} + C_o \frac{\partial v_{ac}(t)}{\partial t}, \quad (2.19)$$

where C_o is the capacitance at $x = 0$. In equation 2.19, the first term is due to the capacitance variations (motional current i_m), and the second term is the displacement current through the static capacitance. The electromechanical transduction factor is defined as [40]:

$$\eta = V_{dc} \frac{\partial C}{\partial x} \approx V_{dc} \frac{C_o}{d}. \quad (2.20)$$

The resulting relation between the motional current i_m , the mechanical transducer velocity \dot{x} , the excitation voltage v_{ac} , and the force F_e at the excitation frequency can be written as [39]:

$$\begin{aligned} i_m &\approx \eta \dot{x}, \\ F_e &\approx \eta v_{ac}, \end{aligned} \quad (2.21)$$

where the displacement x is assumed to be small compared to the gap d . By substituting equation 2.21 into equation 2.14, an electrical equivalent circuit shown in figure 2.10a can be derived. The component values are:

$$\begin{aligned} R_x &= \sqrt{km}/Q_m \eta^2 = k/\omega_o Q_m \eta^2, \\ C_x &= \eta^2/k, \\ L_x &= m/\eta^2. \end{aligned} \quad (2.22)$$

An important observation is that, to obtain a small motional resistance R_x , a large electromechanical transduction factor is needed, requiring either a small gap d or a large DC-

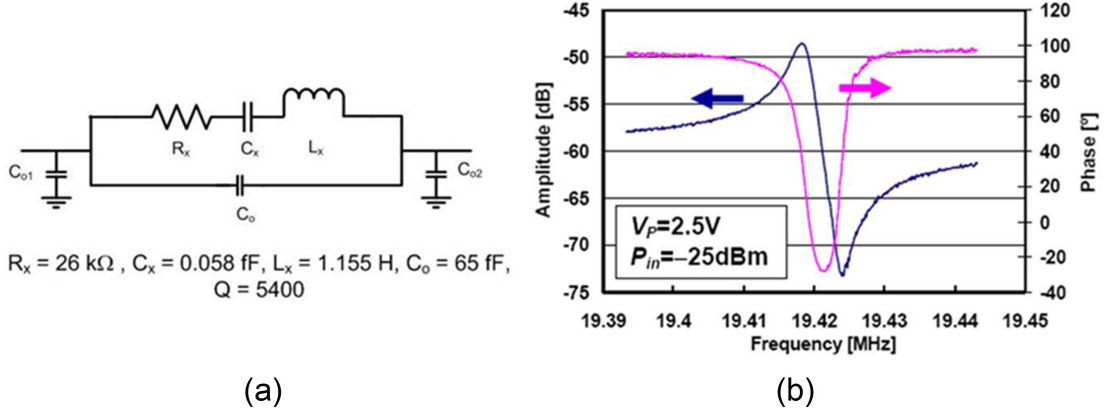


Figure 2.10: (a) Measured spectrum of a MEMS resonator; (b) its equivalent model, Copyright 2008 IEEE [38].

bias voltage V_{DC} . In practice neither V_{DC} can be increased indefinitely, nor can d can be decreased arbitrarily without resulting unwanted non-linear effects. In subsection 2.2.3 below, a non-linear model of the resonator is developed by accounting for cubic and quadratic spring non-linearities in the system that have both electrical (electrostatic spring) and mechanical (geometry and material properties) origins. The unwanted non-linear effects will limit the maximum vibration amplitude of the open-loop resonator.

The electrical Q_e of a series RLC circuit shown in figure 2.10a can be written as $\frac{\omega_m L_x}{R_x}$ and can be related to the mechanical Q_m using equation 2.22 and shown to be equal to it as shown below

$$Q_e = \frac{\omega_m L_x}{R_x} = \frac{\omega_o (m/\eta^2)}{k/(\omega_o Q_m \eta^2)} = Q_m. \quad (2.23)$$

Figure 2.10b is a plot of amplitude and phase response showing both resonance ($\omega_r = \frac{1}{\sqrt{L_x C_x}}$) and anti-resonance ($\omega_{ar} = \frac{1}{\sqrt{L_x C_{ar}}}$, where $C_{ar} = \frac{C_x * C_o}{C_x + C_o}$) of a fixed-fixed beam resonator from [38]. The antiresonance represents the feed through effect due to the static capacitance C_o .

2.2.2 MEMS based Oscillators

Virtually all electronic systems need a clock signal source for synchronization between sub-systems or systems. Over the past few decades, quartz crystals have primarily been used for accurate timing and frequency references in electronic systems. Over the past several years, silicon MEMS resonators (or vibrating MEMS) have been challenging these decade-old quartz based devices. An electrostatically excited resonator in an oscillator implementation is shown in figure 2.11. The oscillator topology uses a series resonant topology in which the micromechanical frequency-setting device (MEMS resonator) is in a positive feedback loop with a transresistance sustaining amplifier possessing sufficient gain to initiate and sustain oscillations. All the oscillator systems are self starting after a DC bias is applied to them. The criteria governing start-up and sustainment of oscillation are given by

- (a) For Start-Up: $R_{amp} > R_x + R_i + R_o$
- (b) In Steady-State: $R_{amp} = R_x + R_i + R_o$ (Also means loop gain equals to 1)
- (c) Loop Phase Condition: 0° around the positive feedback loop

where R_{amp} , R_i and R_o are the gain, input resistance, and output resistance, of the transresistance sustaining amplifier, respectively; and R_x (also referred as the motional resistance) represents the loss in the resonator. The two-port micromechanical resonator can be modeled as a equivalent LCR electrical circuit shown in part (a) of the figure 2.11. The L_x , C_x , and R_x are related to the effective mass, stiffness, and damping, respectively. C_o is the feed-through capacitance and C_{oi} and C_{oo} are input and output parasitic capacitances.

2.2.3 Nonlinear Resonator Model

The sources of non-linear effects in the resonator are both mechanical and electrical. The mechanical non-linearities arise from the geometry and the material properties of the resonator.

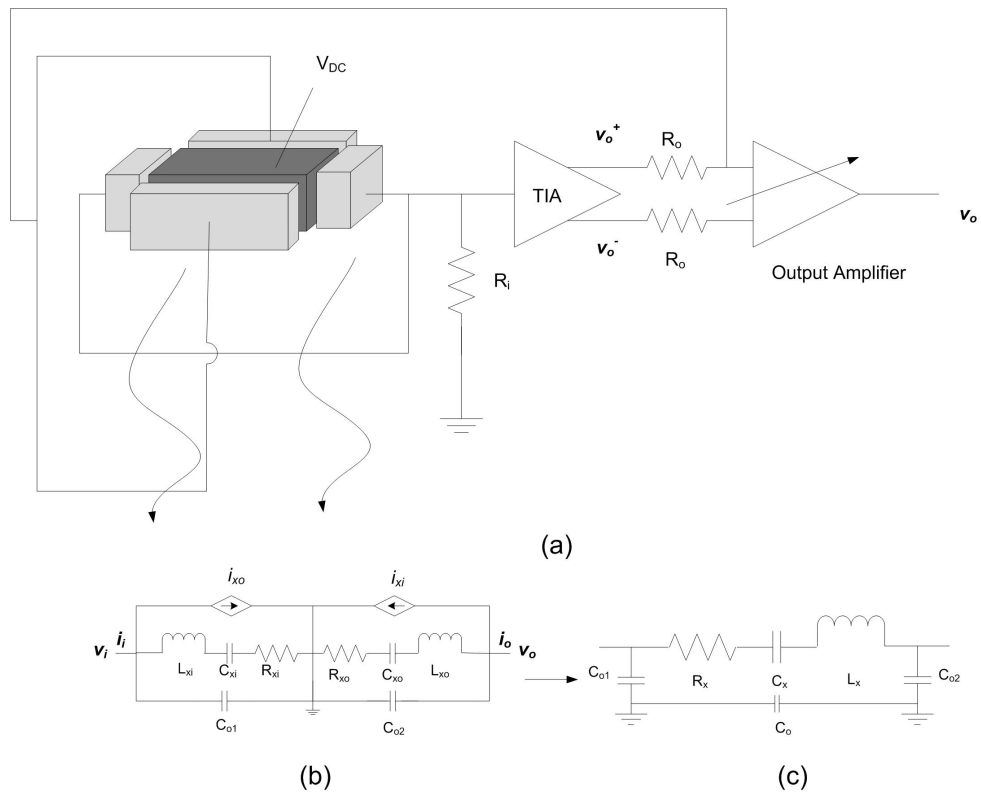


Figure 2.11: Implementation of a MEMS based reference Oscillator. b) Equivalent circuit for both drive and sense electrodes separately. c) Equivalent circuit combining both drive and sense electrodes.

The electrical non-linearities are due to the electrostatic spring that arises due to the inverse relationship between force and displacement as described in equation 2.17. Substituting equation 2.18 in equation 2.17 and expanding the non-linear capacitance gives

$$F_e = \frac{1}{2} \frac{\epsilon_o A (V_{DC} + v_{ac}(t))^2}{d^2} \left(1 + \frac{2x}{d} + \frac{3x^2}{d^2} + \frac{4x^3}{d^3} + \dots \right) \quad (2.24)$$

where V_{DC}^2 multiplied by $\frac{2x}{d}$ subtracts from the linear spring and $\frac{3x^2}{d^2}$ and $\frac{4x^3}{d^3}$ subtracts from the mechanical quadratic and cubic counterparts respectively. In most resonators the electrical component (dependent on V_{DC}) is more dominant than the mechanical spring and the co-efficients of quadratic and cubic non-linearities are negative when taken to the left hand side of the of equation 2.14. Substituting equation 2.24 into equation 2.14 and keeping the terms around the natural resonant frequency, the equation of an externally forced, viscous damped non-linear micro-resonator can be written as

$$m\ddot{x} + c\dot{x} + k_l x + k_q x^2 + k_c x^3 = F_\Omega \cos(\Omega t), \quad (2.25)$$

where x is the displacement of the lumped mass m , c is the damping coefficient, k_l , k_q and k_c are the effective linear, quadratic and cubic spring constants, respectively, and $F_\omega = 2V_{DC}v_{ac} \cos(\Omega t)$ is the magnitude of forcing term close to the natural frequency ω_o . Equation 2.25 can be normalized with respect to m and rewritten as

$$\ddot{x} + \mu\dot{x} + \omega_o^2 x + \alpha_q x^2 + \alpha_c x^3 = F \cos(\Omega t), \quad (2.26)$$

where μ , α_q , α_c and F are the normalized damping, quadratic and cubic non-linearities and forcing respectively. An approximate response to the above non-linear system to a resonant excitation ($\Omega \approx \omega_o$) can be obtained using the perturbation method of multiple scales [41]. This method allows for the steady-state solution of 2.26 to be written (to first approximation) as

$$x = a \cos(\Omega t - \gamma) + H.O.T \quad (2.27)$$

where H.O.T means Higher Order Terms, and the amplitude (a) and phase (γ) of the response are governed by two first order differential equations, also known as modulation equations, which are given as

$$\begin{aligned} \dot{a} &= -\mu a + \frac{F}{\omega_o} \sin \gamma \\ \dot{\gamma} &= \sigma - \frac{S a^2}{\omega_o} + \frac{F}{a \omega_o} \cos \gamma, \end{aligned} \quad (2.28)$$

where S is the effective non-linearity of the system and σ is a frequency detuning parameter ($\sigma = \Omega - \omega_o$). S is a function of the natural frequency, and cubic and quadratic non-linearities, and is given as

$$S = \frac{9\alpha_c \omega_o^2 - 10\alpha_q^2}{24\omega_o^3}. \quad (2.29)$$

It follows from equation 2.27 that periodic solutions of equation 2.26 correspond to constant values of a and γ ; the fixed points (a_{dc} , γ_{dc}) of equation 2.28. Thus letting $\dot{a} = \dot{\gamma} = 0$ in equation 2.28 and elimination γ_{dc} from the resulting equations, we obtain the following frequency-response equation:

$$a_{dc}^2 \left[\mu^2 + \left(\sigma - \frac{S a_{dc}^2}{\omega} \right)^2 \right] = \frac{F^2}{\omega^2} \quad (2.30)$$

that is qualitatively plotted as function of the detuning parameter σ (which is a representation of frequency) in figure 2.12. When the harmonic force F is small, the response of the curve of the resonator retains a single valued function. However, as F exceeds a certain limit, the non-linearity increases (increasing the frequency shift towards the left or the right) and eventually the amplitude-frequency relationship shows discontinuity due to hysteresis

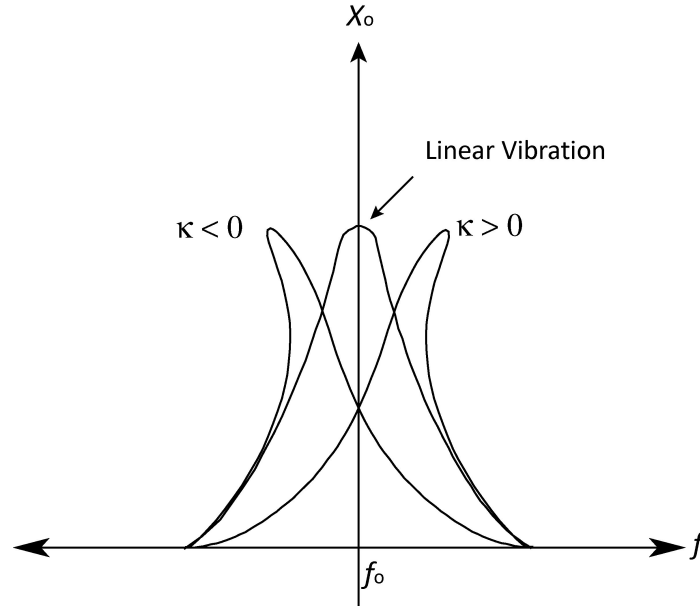


Figure 2.12: The effect of nonlinear stiffness on the resonator frequency.

in a range of frequencies (also termed as bifurcation). The response shows an amplitude-dependent peak resonant frequency as indicated in equation 2.31. The orientation of the peak (non-linear) resonant frequency (Ω_r) shift is determined by the effective non-linearity S/ω_o , indicated as κ in equation 2.31 [41]:

$$\Omega_r = \omega_o + \kappa a_{dc,max}^2 \quad (2.31)$$

where Ω_r is the non-linear resonant frequency, and $a_{dc,max}^2$ is the maximum vibration amplitude at resonance. A negative κ causes the resonance to tilt to a lower frequency where as positive κ results in a higher resonant frequency. At hysteresis point, the maximum vibration amplitude for the system described in equation 2.25 is given by

$$x_m = \sqrt{\frac{4\omega_o}{3\sqrt{3}Q\kappa}}. \quad (2.32)$$

The maximum linear vibration amplitude in an open loop excitation is limited by non-linearity and the non-linear effects set the upper limit to the resonator's dynamic range (the

lower limit being set by noise). The energy stored in the resonator at the this vibration amplitude is given by

$$E_c = \frac{1}{2}k_o x_m^2 \quad (2.33)$$

and the drive level defined as power dissipated in the resonator is

$$P_c = \frac{\omega_o E_c}{Q}. \quad (2.34)$$

Equation 2.34 also gives the maximum output power that can be obtained from the resonator from an open loop response. Phase noise of the oscillator (feedback system) is inversely proportional to the maximum signal power as defined by equation below [42]

$$L(\Delta\omega) = 10 \log \frac{2FkT}{P_c} \left[1 + \left(\frac{\omega_o}{2Q\Delta\omega} \right)^2 \right] \left(1 + \frac{\omega_{1/f}}{\Delta\omega} \right) \quad (2.35)$$

where F is the empirically derived constant included to take into account broadband noise sources other than resistor thermal noise (such as transistor shot noise), and $\omega_{1/f}$ is an empirically determined constant related to the $1/f$ corner frequency, i.e. the frequency at which the current source noise transitions from being dominated by $1/f$ noise to being dominated by shot noise. Leeson's modified equation for phase noise can be split into three regions: the $1/f^3$ region dominated by upconverted $1/f$ noise, the $1/f^2$ region created by filtered broadband noise, and a zero slope region to account for the absolute noise floor of the oscillator. From the equation it is apparent that phase noise in all regions can be decreased by increasing the output power of the oscillator, P_c . Equations 2.32, 2.33 and 2.34 show that the maximum allowable vibration amplitude and hence the output power is limited by the nonlinearities.

In Chapter 6 the concept of phase feedback and how it can be used overcome the limitations arising from the non-linearities in MEMS resonators will be discussed.

2.2.4 Issues with MEMS oscillator solutions

- All Silicon MEMS resonators exhibits an inherent $-20 \sim -30$ ppm/C frequency-temperature stability. To achieve the frequency stability for oscillator applications, compensation over a wide temperature is needed. The extra programming and compensation steps add costs.
- Digital temperature compensation can bring stability to ± 10 ppm or even lower. However, perturbation (frequency pulsation) of a few ppm is observed. This results in poor short term stability with excessive phase noise and jitter
- Startup time is longer when compared with similar crystal oscillators.

2.3 Summary

This chapter discussed the basic electrical modeling of the series and shunt MEMS switches and presented the current status in terms of reliability and performance of state of art MEMS switches. In MEMS resonators, linear and non-linear models of the MEMS resonator were presented with a brief discussion of the phase noise in such resonators. The next set of chapters focuses on work done in this dissertation and attempt to overcome some of the critical issues in RF MEMS switch and resonator performance and applications.

Chapter 3

Design, Modeling and Measurement Results of a Laterally Driven Variable Gap DC Contact Series Switch

This chapter details the design, modeling and measurement results of a laterally driven metal-to-metal contact series switch. The influence of process non-idealities on the variable gap electrostatic actuator is studied by developing an analytical model for actuation voltage and displacement. Fabrication challenges involved in designing a MEMS device in a commercially available foundry technology are discussed, and the impact of contact contamination in MEMS switches is investigated.

3.1 Introduction

Metal-to-metal contact switches typically have high isolation compared with capacitive switches since their contact area along the signal path is smaller, and they also have lower insertion loss at low frequencies since the contact is purely resistive, which makes them par-

ticularly useful for wireless applications in the 1 to 5 GHz range. A key benefit of lateral actuation is the ability to co-fabricate the actuator, contacts, conductor paths and support structures in one lithographic step [28]. The lateral metal contact switch design under study here (see figure 3.1) includes set of movable electrodes are mechanically connected to, but electrically isolated from the contact head by means of a Silicon Nitride card as seen in figure 3.1a. A set of fixed electrodes is interleaved with the movable electrodes. Electrostatic forces developed by the application of the actuation voltage between the fixed and movable electrodes cause the contact head to move to a closed switch state position [43]. Compliant springs support the movable electrode and the contact head for actuation in a lateral direction, parallel to the substrate, when a bias voltage is applied to bring the switch to its closed position. There is standoff gap between the fixed and movable electrodes so that they do not short-circuit each other when the head has made contact with the signal line as seen in figure 3.2.

The performance of an electrostatic actuator depends on the absolute capacitance between the fixed and movable electrode and the distribution of electrostatic forces. Lateral actuators are normally High Aspect Ratio (HAR) structures, so as to increase the overlap area between the electrodes, which in turn reduces the actuation voltage without increasing overall die area occupied by the switch. For such HAR structures, it is difficult to fabricate side-walls that are exactly parallel to each other, particularly when they are electroplated. The resist profile and the stresses involved in electroplating typically causes the width of the electrode fingers to increase linearly with the depth, and the cross-section takes on a trapezoidal profile, resulting the actuators acting as non-parallel plate capacitors [44]. Understanding the effect of non-parallel plate capacitors in such actuators is important since capacitances, net forces, switch displacement and pull-in voltage vary with the angle α of the non-parallel plate side-walls. The sidewall angle also causes the *spring* cross-sections to become trapezoidal instead of rectangular. The effect of such non-rectangular cross-sections on spring constants has yet to be studied.

In section 3.2, theoretical expressions for mechanical spring constant, capacitance, net forces,

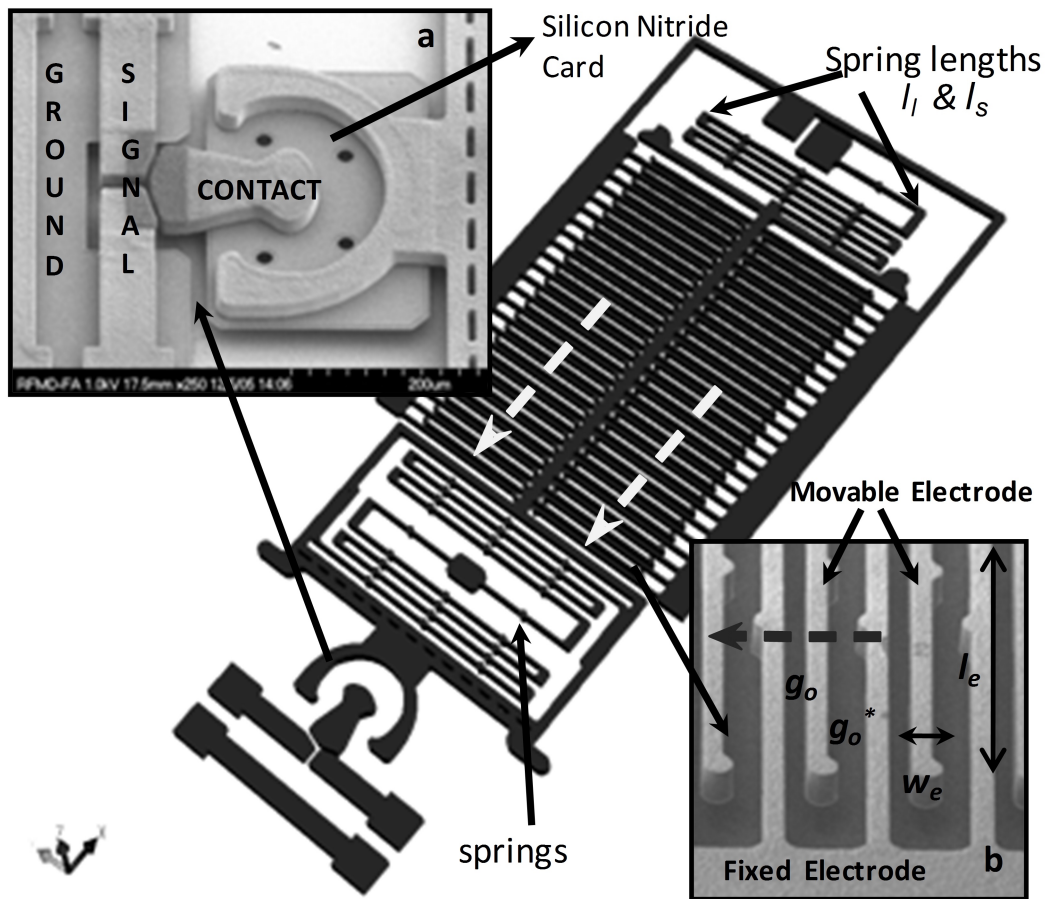


Figure 3.1: 3D switch model. Insets show SEMs of switch: a) contact. b) asymmetric electrode spacing. The dotted arrows in the figure indicate the direction of motion.

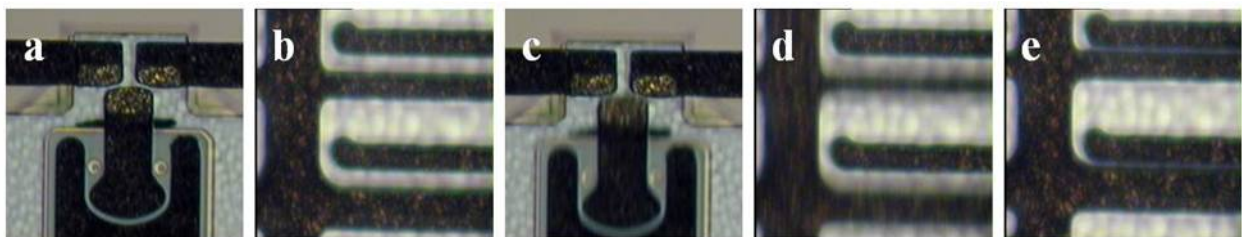


Figure 3.2: Optical images of the contact head and electrodes when no voltage is applied (a, b). Matching images when the switch is in motion during pull-in (c, d). Finally, the standoff gap at the electrodes is seen when the switch is closed (e).

switch displacement and pull-in voltage of parallel and nonparallel-plate capacitors and rectangular and trapezoidal springs, are derived and the results are compared to electromechanical finite-element analysis (FEA). The out of plane deformation or droop of the fixed and movable electrodes is also considered via FEA analysis. In section 3.3 some of the fabrication challenges that were overcome by design are presented. In section 3.4 analytical/FEA model is matched to the experimental results and the combined influence of the side-wall angle (α) on the net forces (F_{net}), spring constant (K_x), switch displacement (Δ_{PI}) and pull-in voltage (V_{PI}) are studied. Section 3.5, finally summarizes the conclusions of this work.

3.2 Design and Modeling

The lateral switches in this work were built in the MetalMUMPS technology at MEMSCAP [1]. The process flow is described in detail in chapter 1 under section 1.3.1. In this technology, very tall structures of electroplated nickel, between 18-22 μm tall, can be built on top of polysilicon and nitride with a deep, KOH-etched trench underneath. Electroplated nickel is used as the primary structural material, and also as the electrical interconnect layer. Doped polysilicon can be used for resistors, additional mechanical structures, and/or cross-over electrical routing. Silicon nitride is used as an electrical isolation layer. Deposited oxide (PhosphoSilicate Glass, PSG) is used for the sacrificial layers. The trench layer in the silicon substrate can be incorporated for additional thermal and, or electrical isolation. Gold overplate can also be used to coat the sidewalls of nickel structures with a low contact resistance material. Mechanical design of an electrostatic pull-in actuator starts with a spring constant K_x , electrode spacings g_o and g_o^* , and the area of electrode overlap A (See figure 3.1b). The specific actuator under study relies on unidirectional motion due to the asymmetric electrode spacings g_o^* and g_o as shown in figure 3.1b. The movable electrode is supported by three folded springs, one anchored at the electrode end and two anchored at the top, each with a spring constant of k_x , as shown in figure 3.1. Each of the folded spring includes four long beams (l_l) and one or two short beams (l_s) in series. Modeling the

beam as a fixed-guided end, and assuming simple bending, the stiffness along the direction of motion for each of the long and short beams can be written as [45]

$$k_l \approx \frac{Ew_s^3t}{l_l^3} \text{ and } k_s \approx \frac{Ew_s^3t}{l_s^3} \quad (3.1)$$

and hence the effective spring constant of one of the folded springs can be written as

$$k_x \approx \frac{4k_l \times 2k_s}{4k_l + 2k_s} \approx \frac{Ew_s^3t}{(2l_s^3 + 4l_l^3)} \quad (3.2)$$

where E is the Young's modulus and w_s , t , l_s and l_l are the width, thickness, and length of short arm and long arm of the spring, respectively. The stiffness K_x of the system is three times k_x , since the three springs are employed in parallel to each other. Folded springs were used to substantially lower the spring force along the direction of motion while conserving die area. To mitigate lateral stiction, the length of an electrode is chosen such that its stiffness is much larger than K_x . Table 3.1 gives the drawn dimensions and material constants for the switch design under consideration. The switch was designed such that the pull-in voltage is below 40 V.

Equation 3.3 describes the force balance which predicts net force (F_{net}) as a function of switch displacement (Δ) and bias voltage (V) applied between the fixed and movable electrodes:

$$F_{net}(\Delta) = -K_x\Delta + \frac{\epsilon_o V^2 A}{2} \left[\frac{1}{(g_o - \Delta)^2} - \frac{1}{(g_o^* + \Delta)^2} \right] \quad (3.3)$$

where A is the overlap area between the movable and fixed electrodes and g_o and g_o^* are the electrode and non-electrode gaps of the lateral actuator as shown in figure 3.1b. The first term is the linear spring force (spring constant, K_x , multiplied by the switch displacement, Δ) which opposes the electrostatic force (second term) in the equation. The electrostatic force across the variable capacitor can be obtained by differentiating the potential energy ($E = CV^2/2$) stored in the capacitor, with respect to the variable gap.

Ni Young's Mod. (E)	200 GPa
Si ρ (high/low)	5000/2 Ωcm
Ni thickness (t)	20 μm
Contact gap	$\sim 5.25 \mu\text{m}$
Gold overplate/side	$\sim 1\text{-}2 \mu\text{m}$
Electrodes	
Width (w_e)	10 μm
Length overlap (l_e)	350 μm
Decreasing gap (g_o)	13 μm
Increasing gap (g_o^*)	21 μm
Spring	
Width (w_s)	8 μm
Long section (l_l)	670 μm
Short section (l_s)	300 μm

Table 3.1: Physical dimensions and material constants of the lateral switch in discussion.

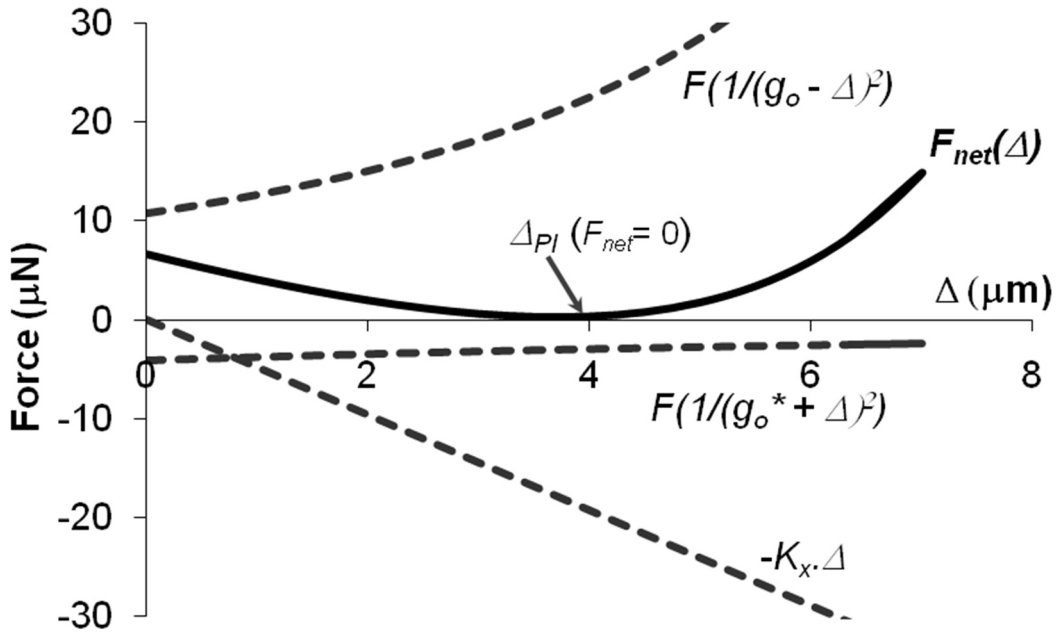


Figure 3.3: Plot shows switch forces, F_{net} in μN as function of electrode travel, Δ in μm .

Figure 3.3 is a plot of equation 3.3. It is evident from the graph that attractive electrostatic forces ($F/(g_o - \Delta)^2$) between the electrodes separated by the smaller gap g_o are far higher than the opposing force ($F/(g_o^* + \Delta)^2$) between electrodes separated by the larger gap g_o^* . When the applied voltage is V_{PI} (pull-in voltage), the switch travels a distance of Δ_{PI} that results in the net force F_{net} equal to zero. This represents the last stable equilibrium where spring forces balance the electrostatic forces, beyond which, the switch becomes unstable and pulls-in.

As shown in figure 3.3, for the design parameters in Table 3.1, when the electrode travels 3.7 μm , the electrostatic force balances the spring force and the switch is ready to pull-in. The pull-in travel, Δ_{PI} , for a simple parallel plate capacitor switch would be 4.33 μm or $1/3^{rd}$ of the gap ($g_o = 13 \mu\text{m}$, see Table 3.1). The actual pull-in travel for this switch, however, is less than this value because of its asymmetric electrode configuration as shown in figure 3.1b [46].

F_{net} in equation 3.3 is plotted as function of displacement for a given voltage. The voltage for which the minima of the curve F_{net} corresponds to zero force is the pull-in voltage ($V_{PI} = 33.6$ V) of the switch. The spring constant K_x obtained using equation 3.2 is equal to 4.8 N/m. In order to find analytical expressions for Δ_{PI} , the net force $F_{net}(\Delta)$ is differentiated in equation 3.2 with respect to Δ to determine the point at which the minimum occurs:

$$\Delta_{PI} = \left[\frac{a^3b - b^3a}{2(a^3 + b^3)} \right] \quad (3.4)$$

where $a = g_o^* + \Delta_{PI}$ and $b = g_o - \Delta_{PI}$. The above equation can then be solved for a given set of electrode gaps. Finally, the pull-in voltage (V_{PI}) is obtained by substituting equation 3.4 into equation 3.3 and solving for V :

$$V_{PI} = \sqrt{\frac{2K_x\Delta_{PI}}{\epsilon A} \frac{a^2b^2}{(a^2 - b^2)}} \quad (3.5)$$

The above analytical model includes expressions for spring constant (K_x), net force (F_{net}), travel before pull-in, and pull-in voltage (V_{PI}). These expressions are derived under the assumption of a parallel plate capacitor; however in reality the sidewalls are inclined at a small angle (α) as a result of fabrication non-idealities. Figure 3.4 depicts the Scanning Electron Microscope (SEM) pictures of Focused Ion Beam (FIB) cross-sections of a typical spring and electrode for the switch under study showing the inclined sidewalls on the electrodes and springs. The side wall angle (α) can be extracted from the SEM cross-sections of various electrode and spring structures from across the die.

Figure 3.5 shows a 3-D cross- section of the FEA model of electrodes and springs. In section 3.2.1 a more accurate model for the serpentine springs is derived using the energy method [47]. The influence of side-wall angle on the springs is also studied and an analytical spring model is developed for trapezoidal cross-sections and the results are matched to the FEA-simulated values.

A more accurate model for the actuator is developed in section 3.4.1 by accounting for the

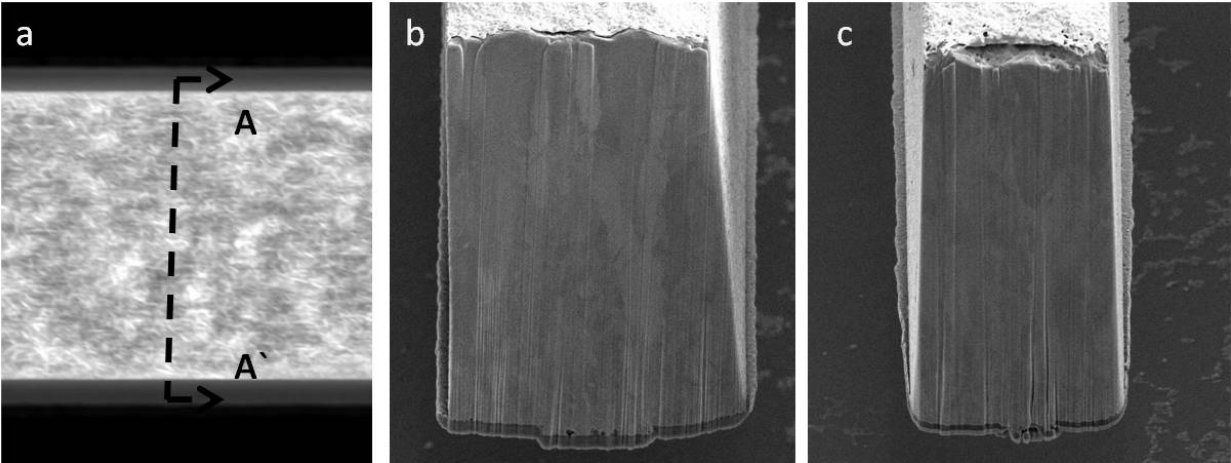


Figure 3.4: SEM pictures a) Top-view of the electrode, b) Electrode cross-section ($A - A'$) and c) Spring cross-section depicting trapezoidal profiles. The cross-sections were obtained using Focused Ion Beam (FIB).

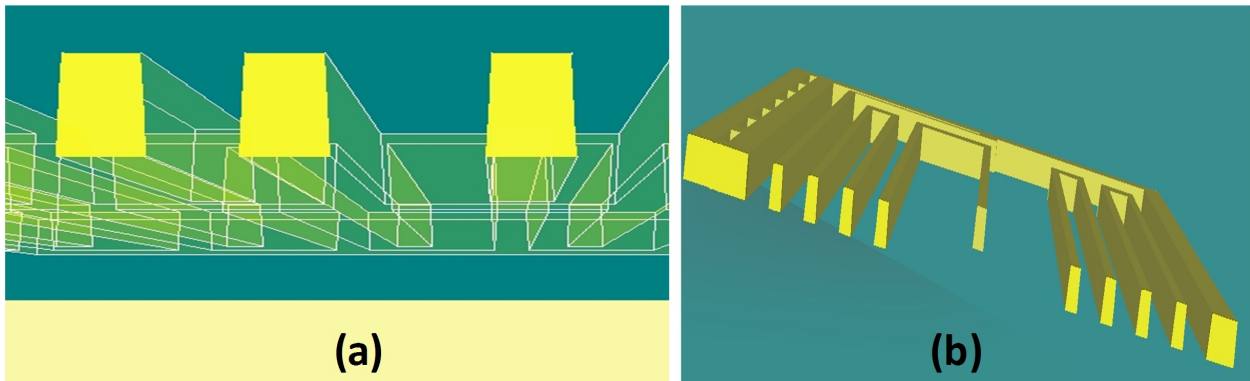


Figure 3.5: 3D Cross sections: a) Electrodes and b) Springs with Trapezoidal Profile.

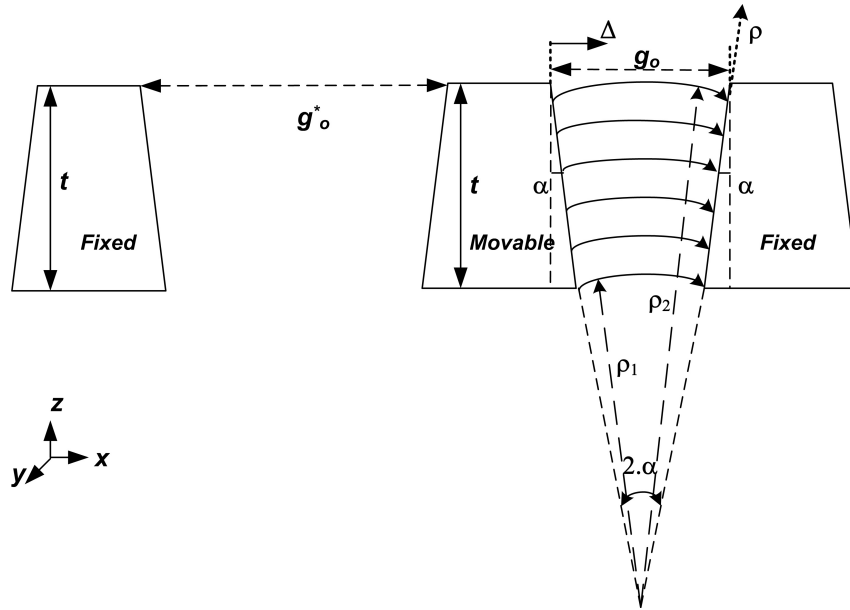


Figure 3.6: Schematic representation of the asymmetric electrode spacing in the actuator.

inclined capacitor and electrostatic fringing as a function of the moving gap, and analytical expressions for travel before pull-in (Δ_{PI}) and the pull-in voltage (V_{PI}) as a function of α are derived and matched to the FEA model. Figure 3.6 shows a schematic representation of a typical electrode and spring structure with a trapezoidal cross-section and side-wall angle (α).

3.2.1 Modeling the Spring

There are three serpentine springs that operate in parallel to actuate the lateral switch as shown in figure 3.1. Figure 3.7 shows a free body diagram of one serpentine spring with 6 meanders. Expressions for spring constant are derived using Castigliano's energy method [48]. Castigliano's energy method allows for the determination of displacements of a linear-elastic system based on the partial derivatives of the strain energy. Castigliano's first theorem is used for determining forces by differentiating energy with respect to generalized displacement in an elastic structure. The second theorem is used for determining displacements along the

direction of applied force by differentiating energy with respect to generalized force in a linearly elastic structure. The strain energies for each of the horizontal and vertical beam sections are given by [47]

$$U = \sum_{i=1}^n \int_0^{L_a} \frac{M_a^2}{2EI_a} d\xi + \sum_{j=1}^n \int_0^{L_b} \frac{M_b^2}{2EI_b} d\xi \quad (3.6)$$

where: $M_{a,b}$, $L_{a,b}$ correspond to the applied moment, and the length respectively; and $I_{a,b}$ correspond to the cross-sectional moments of inertia at any point along the horizontal and vertical segments; and ξ is the distance variable along each of the beam segments. The cross-sectional moments of inertia are computed for both rectangular and trapezoidal cross-sections as shown in figure 3.5. A detailed definition of the side-wall angle is given in section 3.2.2 while defining the actuator. To determine the x -directed spring constant, the displacement of the spring end in the y -direction ($\delta y = \partial U / \partial F_y$) and the rotation of the spring end ($\delta \theta_o = \partial U / \partial M_0$) are constrained to be zero. Application of Castigliano's second theorem produces three equations in three unknown variables (F_x , M_0 and δ_x), where δ_x is the displacement in the x -direction. Some assumptions are made in this derivation, such as linearity, small deflection, slender beam, negligible shear and pre-strain energies. The derived stiffness expression for the spring in figure 3.7 is given in equation 3.7. This expression assumes the moments of inertia for both x and y directed sections of the spring, I_a and I_b , are equal to I .

$$k_x = \frac{EI(10368a^2 + 22752ab + 12360b^2)}{14625a^3b^2 + 37368a^2b^3 + 29379ab^4 + 6089b^5} \quad (3.7)$$

The actual stiffness expressions for all the three springs are calculated using the above procedure based on the dimensions of each of the sections and also accounting for the moment of Intertia (I) for both rectangular and trapezoidal cross-sections. A trapezoidal cross-section defined by the side-wall angle α is shown as an inset it in figure 3.8. Since the actual expressions are too large to present here, figure 3.8 summarizes the stiffness values

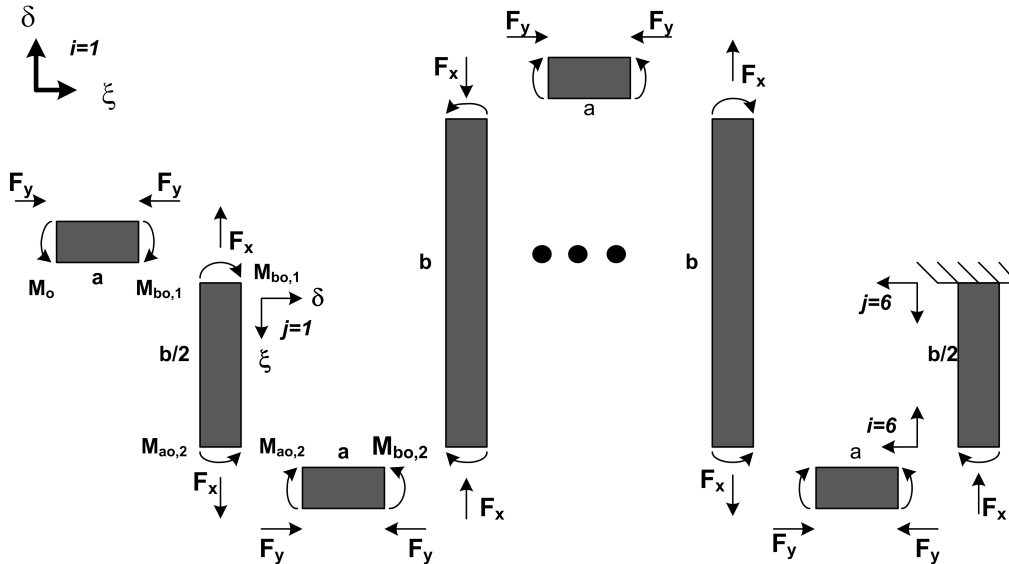


Figure 3.7: Free-body diagram of a serpentine spring (after [47])

of the spring calculated analytically versus simulations done with Coventor FEA software [49]. Both the analysis and the FEA model do not account for the intrinsic stresses in the structure in the spring constant calculation. It can be seen from the graph that Castigliano's Energy method matches well with the FEA (without intrinsic stress) when the sidewall angle is zero and the percentage error at 1.5 degrees of side-wall angle is about 6 % as compared to 22.2 % error when calculated using the simple bending method.

3.2.2 Modeling the Actuator

In section 3.2 analytical expressions for the force (F_{net}), pull-in voltage (V_{PI}) and distance traveled before pull-in (Δ_{PI}) were derived for electrodes that are perfectly parallel to each other. In this section, the sidewall angles are accounted for by modeling the actuator as a *non-parallel* plate capacitor, and the above mentioned parameters are recalculated to develop a more accurate model for predicting the performance of the switch. First, analytical expressions for a single-sided inclined capacitor are derived and the analysis is then extended to a double-sided case.

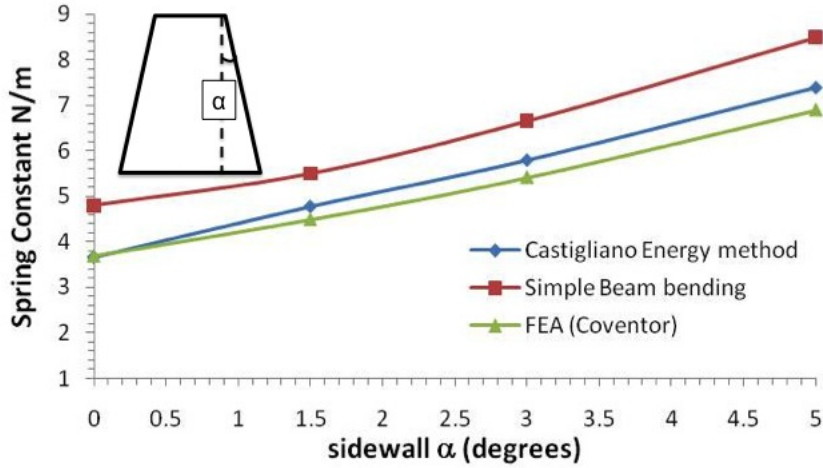


Figure 3.8: Plot of spring constant values as function of sidewall angle α calculated analytically and compared with FEA. Castigliano's energy method models the spring stiffness more accurately than the simple bending analysis.

The theoretical expressions for the non-parallel plate case are derived based on the schematic in figure 3.6. The derivation of the non-parallel plate capacitance is adapted from [50]. Once the capacitance value is obtained, analytical expressions for force, pull-in travel and, finally, the pull-in voltage are derived. The effect of the fringing fields of the non-parallel plate capacitor is initially neglected but is subsequently accounted for by multiplying the capacitance with a constant fringe factor. For the gap between the inclined electrodes, a top gap of g_o or (g_o^*) is used since it can be more easily measured; it should also be noted that the top gap is slightly different from the drawn size and is accounted for in the model. Increasing α brings the bottom edges of the electrodes closer together.

From the geometry in figure 3.6, the charge per unit area ϕ , can be expressed as :

$$\phi = \frac{\epsilon V}{2\alpha\rho} \quad (3.8)$$

where V is the applied voltage, α is the side-wall angle, ρ is the distance in the radial direction and $\varepsilon = \varepsilon_o\varepsilon_r$ is the permittivity of free space times the relative permittivity. Using the relation $C = Q/V$, the total capacitance between the inclined plates can be written as:

$$C = \frac{1}{V} \int \phi dA = \frac{l}{V} \int_{\rho_1}^{\rho_2} \frac{\varepsilon V}{2\alpha\rho} d\rho = \frac{\varepsilon l}{2\alpha} \ln \left(\frac{g_o}{g_o - 2t(\tan\alpha)} \right) \quad (3.9)$$

where A ($l(\rho_2 - \rho_1)$) is the overlap area and l is the length of the electrode. For movable plates the above equation can be re-written as,

$$C_s = \frac{\varepsilon l}{2\alpha} \left[\ln \left(\frac{g_o - \Delta}{(g_o - \Delta) - 2t(\tan\alpha)} \right) \right] = \frac{\varepsilon l}{2\alpha} \left[\ln \left(\frac{g_o - \Delta}{(g_o - \Delta) - 2t\alpha} \right) \right] \quad (3.10)$$

where g_o is the electrode gap at the top of the electrode, t is the thickness, and Δ is the electrode travel in the positive x -direction. For small α , $\tan\alpha = \alpha$. The electrostatic force can be obtained by differentiating the energy, $E(= CV^2/2)$ with respect to the gap. The capacitance derived in equation 3.10 is used to calculate the electrostatic force as shown in equation 3.11

$$F_e = \frac{\partial(CV^2)}{2\partial\Delta} = \frac{\varepsilon AV^2}{2(g_o - \Delta)(g_o - \Delta - 2t\alpha)} \quad (3.11)$$

Equation 3.12, below, describes the force balance which predicts net force (F_{net}) as a function of switch displacement (Δ) and voltage (V) for a single-sided inclined capacitor.

$$F_{net} = -K_x\Delta + \frac{\varepsilon AV^2}{2(g_o - \Delta)(g_o - \Delta - 2t\alpha)} \quad (3.12)$$

When the applied voltage is V_{PI} , the spring forces ($K_x\Delta$) balance the electrostatic force (F_e) and F_{net} is zero which is the condition for pull-in. In order to find analytical expressions for Δ_{PI} the net force $F_{net}(\Delta)$ in equation 3.12 is differentiated with respect to Δ to compute the point at which the minimum occurs. This gives us the distance traveled before pull-in:

$$\Delta_{PI} = g_o - g_{PI} = \frac{g_{PI}(g_{PI} - 2t\alpha)}{2(g_{PI} - t\alpha)} \quad (3.13)$$

It can be seen from equation 3.13 that when $\alpha = 0$, the distance traveled before pull-in, is equal to $1/3$ of g_o , which is the standard result for a parallel plate actuator. Equation 3.13 is used to explicitly solve for g_{PI} as shown in equation 3.14 and the travel before pull-in (Δ_{PI}) would simply be $g_o - g_{PI}$.

$$g_{PI} = \frac{(4t\alpha + 2g_o) \pm \sqrt{(4t\alpha + 2g_o)^2 - 24t\alpha g_o}}{6} \quad (3.14)$$

This analysis can now be extended to a double sided electrode configuration (Figure 3.6) with gaps g_o and g_o^* . The double sided inclined capacitance for movable plates can be written as two single-sided capacitances in parallel as shown below:

$$C_d = \frac{\epsilon l}{2\alpha} \left[\ln \left(\frac{g_o - \Delta}{(g_o - \Delta) - 2t\alpha} \right) + \ln \left(\frac{g_o^* + \Delta}{(g_o^* + \Delta) - 2t\alpha} \right) \right] \quad (3.15)$$

Since the motion is in the positive x -direction as shown in figure 3.6, the switch travel adds to the non-electrode gap ($g_o^* + \Delta$) and subtracts from the electrode gap ($g_o - \Delta$) as can be seen from equation 3.15. The capacitance (shown in Figure 3.9) always increases with increasing α . The F_{net} for the inclined double-sided actuator can be modeled as shown in equation 3.16.

$$F_{net}(\Delta) = -K_x \Delta + \frac{\epsilon_o V^2 A}{2} \left[\frac{1}{[(g_o - \Delta)^2 - 2t(g_o - \Delta)]} - \frac{1}{[(g_o^* + \Delta)^2 - 2t(g_o^* + \Delta)]} \right] \quad (3.16)$$

The first term is the spring force and the second term is the electrostatic force (F_e) that opposes the spring force. When α is set to zero the forces are equivalent to the parallel plate actuator as described by equation 3.16. An analytical expression for the distance traveled before pull-in can be derived as described earlier and is given as:

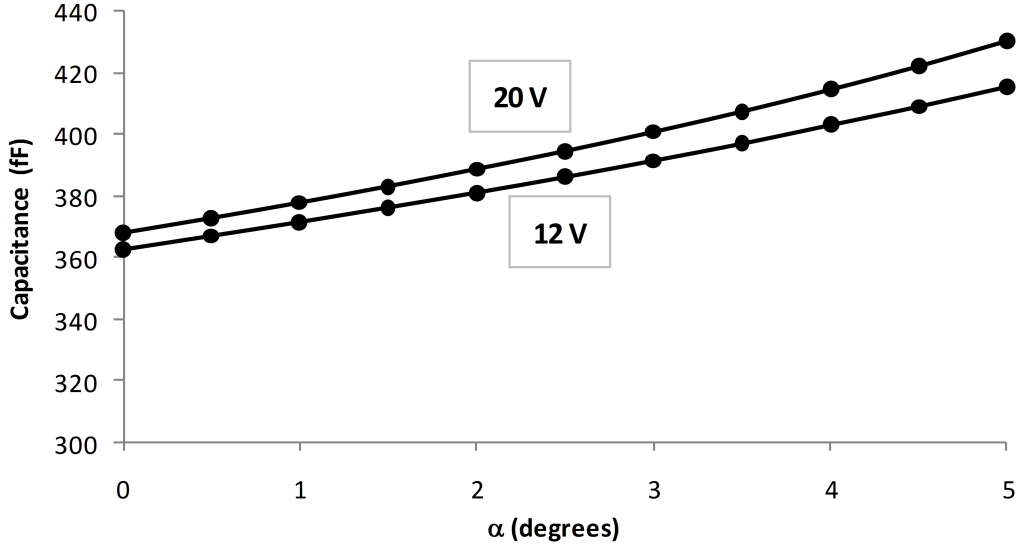


Figure 3.9: Capacitance as a function of α when the applied Voltage = 12 V and 20 V.

$$\Delta_{PI} = \frac{1}{2} \left[\frac{a^2 b (a - 2t\alpha)^2 (b - 2t\alpha) - b^2 a (b - 2t\alpha)^2 (a - 2t\alpha)}{a^2 (a - 2t\alpha)^2 (b - t\alpha) + b^2 (b - 2t\alpha)^2 (a - t\alpha)} \right] \quad (3.17)$$

where $b = g_o - \Delta_{PI}$ and $a = g_o^* + \Delta_{PI}$. It should also be noted that Δ_{PI} is independent of K_x , area (A) and applied voltage (V), but is a function of electrode (g_o) and non-electrode gaps (g_o^*). Figure 3.10 is a plot of travel before pull-in as a function of sidewall angle α for both single and double sided capacitance. It can be seen from the plot that, for a double-sided capacitor, for an increase in α (0 to 5 degrees, 5.5 % change), the pull-in travel decreases by $0.55 \mu\text{m}$ (14 % change). It should also be noted from the plot that the pull-in travel for a double sided capacitor is lower than the single sided case irrespective of the sidewall angle α . The parallel capacitance due the wider gap g_o^* has the effect of weakening the linear spring term (K_x). This can be illustrated by expanding equation 3.3 in a Taylor series and retaining the linear terms as shown below:

$$F_{net}(\Delta) = -K_x \Delta + \frac{\epsilon_o V^2 A}{2} \left[(g_o)^2 - (g_o^*)^2 + 2\Delta \left(\frac{1}{g_o} + \frac{1}{g_o^*} \right) \right] \quad (3.18)$$

The third term (co-efficient of Δ) inside the brackets subtracts from the spring force (K_x).

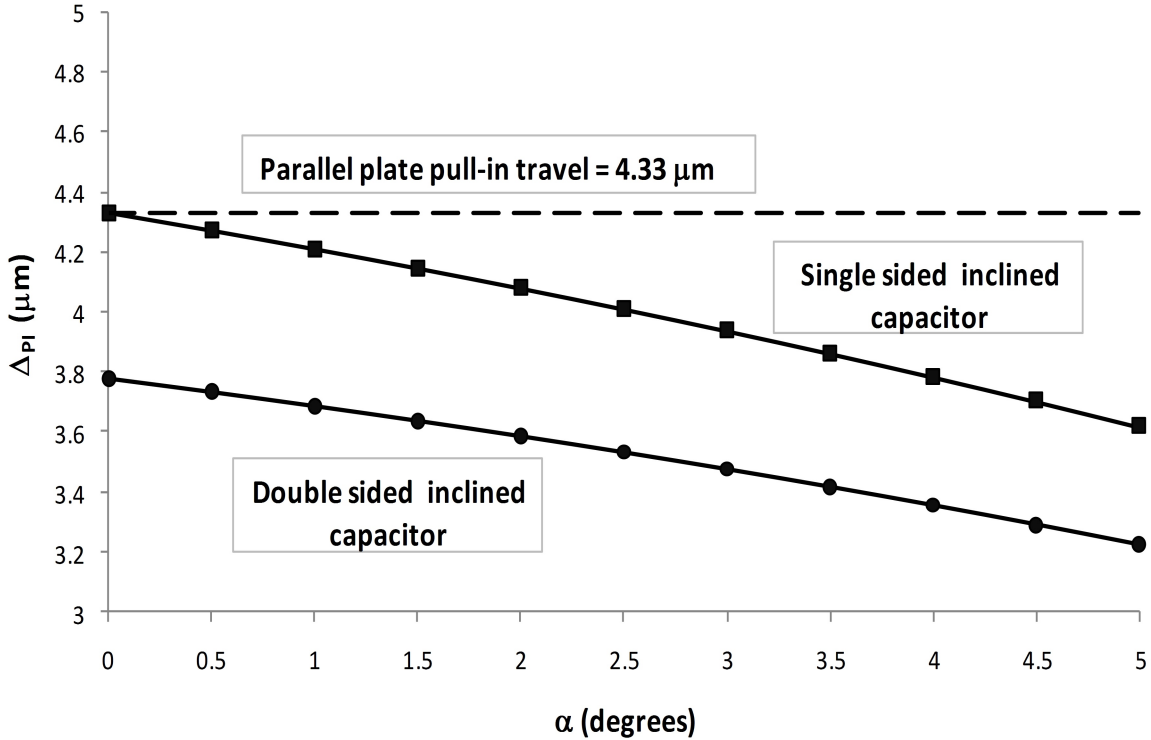


Figure 3.10: Plot of maximum switch travel (Δ_{PI}) before pull-in as a function of sidewall angle α . The plot shows the travel for a single sided capacitor (squares) and a double sided capacitor (circles) as a function of the sidewall angle α .

The addition of the $1/g_o^*$ term weakens it further and hence the pull-in travel is smaller for double sided capacitance, where the capacitance due to the wider gap is essentially parallel to the narrow gap actuating capacitance. On the other hand the pull-in instability in the electrostatic actuation can be reduced or even eliminated by the addition of a series capacitor in the DC path of the MEMS capacitor [24], [51].

Finally, the pull-in voltage as a function of α can be found as described earlier:

$$V_{PI} = \sqrt{\frac{2K_x \Delta_{PI}}{\epsilon A} \frac{a(a - 2t\alpha) b(b - 2t\alpha)}{a(a - 2t\alpha) - b(b - 2t\alpha)}} \quad (3.19)$$

As would be expected, increasing α increases both K_x and C_d . These two factors have opposite effects on the pull-in voltage of the actuator, as illustrated in figure 3.11, a plot of

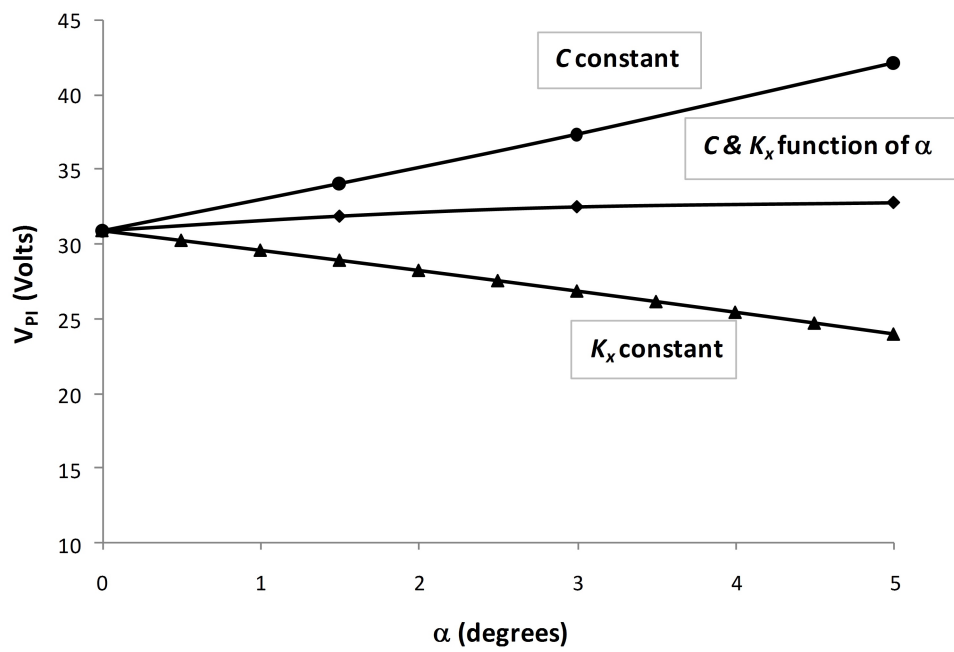


Figure 3.11: Plots of Pull-in voltage (V_{PI}) as a function of side-wall angle (α) by keeping K_x as constant (triangles), by keeping Capacitance as a constant (circles) and finally varying both Capacitance and K_x as a function of α (squares).

V_{PI} as function of the side-wall angle α . To show the two effects of α on V_{PI} , K_x is first kept constant at 3.7 N/m (this is the value of K_x when α equals zero) while allowing α to change capacitance decrease in V_{PI} is observed. Next, the capacitance is kept constant (when alpha equals zero) while allowing α to change K_x (see figure 3.8), and observing the expected increase in V_{PI} . Finally to predict the overall change in V_{PI} with respect to α , both capacitance and stiffness are calculated as α varies over a range from 0 to 5 degrees. The two effects largely counter each other and V_{PI} increases only slightly over a significant range of side wall angle as shown in figure 3.11.

Figure 3.12 illustrates the variation of electrostatic force as a function of side-wall angle (α) for the dimensions of the switch given in Table 3.1. As shown in the figure, electrostatic force increases with α . The electrostatic force was computed using equation 3.16 (without the spring force) for applied voltages of 12 and 20 V. The travel (Δ) in equation 3.17 is calculated when the applied voltage is equal to 12 or 20 V for each of the corresponding α values. The value of the spring (K_x) is held constant for these calculations. To compute the true influence of α on force, the influence of α on K_x is included in computing the travel (Δ) for the above voltages the electrostatic force is recalculated (dashed lines in figure 3.12). It can be seen from the plot that including the influence of α on K_x decreases the electrostatic force (F_e) at higher voltages, but its effect is minimal at lower voltages. However, F_e still increases modestly overall with increasing α . The above trend in the influence of α on net the force (F_e) is similar to the variation of capacitance C_d due to the sidewall angle as seen earlier in figure 3.9. Hence, for applications that rely on capacitive sensing (force, acceleration etc.), not accounting for the sidewall angle leads to incorrect estimation of forces, pull-in travel and their pull-in voltages.

3.2.3 Modeling Fringing fields

Finally, the effect of electrostatic fringing fields as a function of the moving gap is modeled. The increase in capacitance due the fringing fields is accounted in the model by increasing

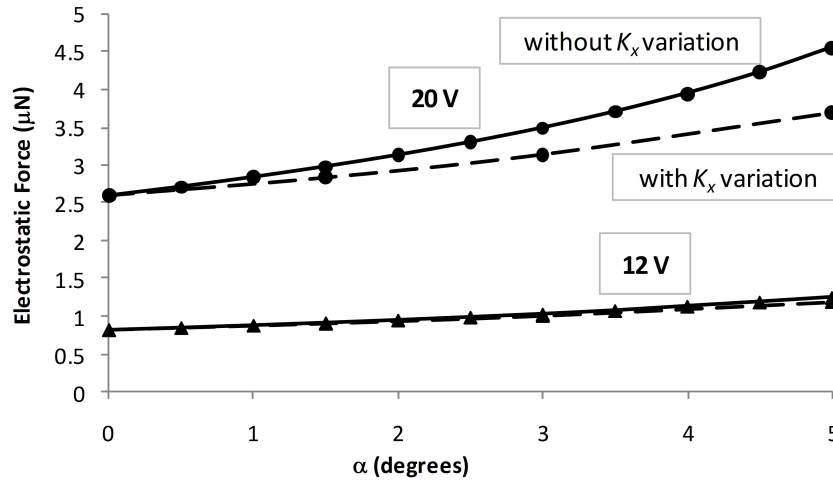


Figure 3.12: Electrostatic forces as a function of α when Voltage = 12 V and 20 V (solid lines) by not accounting for the influence of α on K_x (is held constant). The dotted lines in both the graphs correspond to the electrostatic forces after accounting for the influence of α on K_x in computing the travel for the above voltages.

the effective area between the plates. If the plates are close to each other ($g_o \ll l, t$), the effect of the fringing fields is less than if they are slightly farther apart ($g_o \approx t$). Hence, to account for fields as a function of the gap, half of the gap (g_o) to either side of the thickness (t) and the length (l) is added as shown in the figure 3.13. For a regular parallel plate capacitor the effective capacitance after accounting for the fringing field is written as:

$$C_f = \frac{\epsilon(t+g)(l+g)}{g} \approx \frac{\epsilon A}{g} \left(1 + \frac{g}{t}\right) \text{ for } g \ll l \quad (3.20)$$

where g , t and l are the gap, thickness and the length of the electrodes and A is the area of overlap given by t times l . It should be noted in the above equation that the fringe factor given by g/t is no longer a constant and varies with the gap. As implied by the equation, the effect of fringe field for smaller gaps is less compared to increasing gaps. Similarly, for a double sided inclined capacitor with a varying gap (given by equation 3.15) the fringing fields are modeled as:

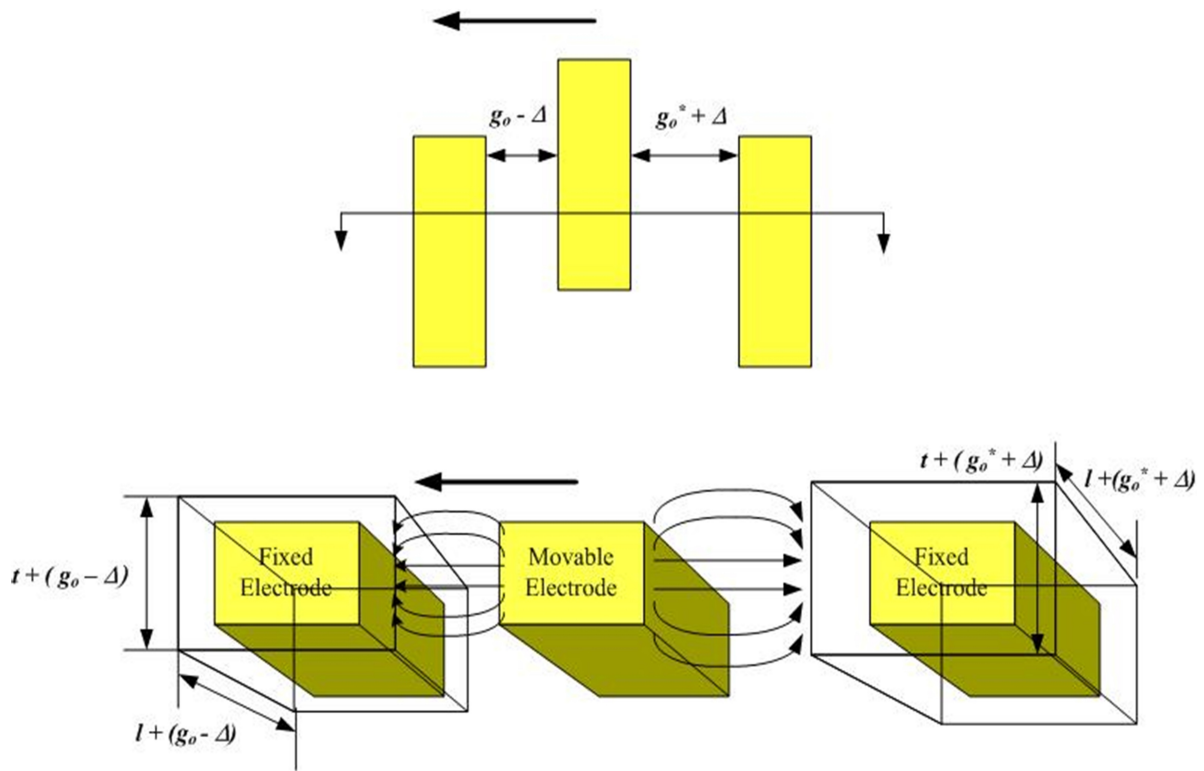


Figure 3.13: Electrode cross-section showing the increased capacitance area between the electrodes accounting for increased capacitance due to the fringing fields.

$$C_{fd} = \frac{\varepsilon l}{2\alpha} \left[\ln \left(\frac{g_o - \Delta}{(g_o - \Delta) - 2t\alpha} \right) \left(1 + \frac{g_o - \Delta}{t} \right) + \ln \left(\frac{g_o^* + \Delta}{(g_o^* + \Delta) - 2t\alpha} \right) \left(1 + \frac{g_o^* + \Delta}{t} \right) \right] \quad (3.21)$$

As can be seen in equation 3.21, the fringe factor multiplying the electrode gap (g_o) is smaller compared to the non-electrode gap (g_o^*) because g_o^* is greater than g_o . The force generated after accounting for the fringe field can be easily calculated by differentiating the energy ($C_{fd}V^2/2$) stored in the capacitor. After further simplification, the new net force $F_{net,f}$ including the effects of fringing can be written as:

$$F_{net}(\Delta) = -K_x\Delta + \frac{\varepsilon_o V^2 A}{2} \left[\frac{1}{(g_o - \Delta)^2} \left(1 + \frac{g_o - \Delta}{t} \right) - \frac{1}{(g_o^* + \Delta)^2} \left(1 + \frac{g_o + \Delta}{t} \right) \right] \quad (3.22)$$

Comparing equations 3.12 and 3.22, it can be observed that the $F_{net,f}$ will be lower than F_{net} for a given voltage (V) because the opposing force due the non-electrode gap (the second term inside the braces) is larger in $F_{net,f}$ than in F_{net} (equation 3.12). This is because of the larger multiplying fringe factor $(1 + (g_o^* + \Delta)/t)$. Hence, the constant fringe case will under-predict the pull-in voltage of the switch. Figure 3.14 plots CV curves predicting the pull-in voltages for both cases. It can be seen that the constant fringe case (blue curve) underestimates the pull-in voltage. The analytical model is compared to the FEA simulations (red curve) and their pull-in voltages match closely. The FEA over predicts the zero bias capacitance by about 6 fF.

3.2.4 Contact Head Design

The contact head is mechanically coupled but electrically isolated from the movable electrode by means of a SiN membrane as shown in figure 3.2a. The membrane provides DC to RF isolation. The Ni sidewalls on the head and signal lines are overplated with gold to enable low contact resistance.

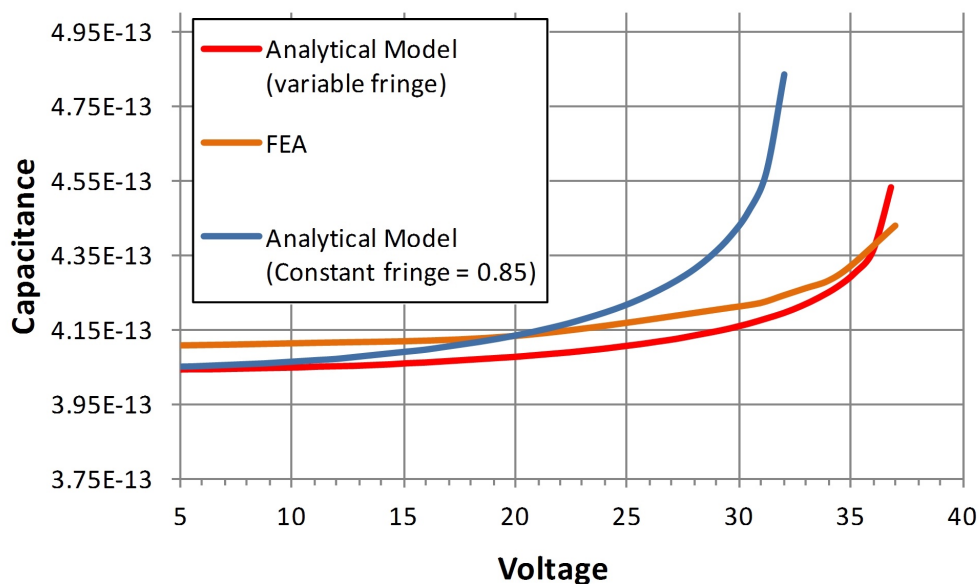


Figure 3.14: Plot of CV curves comparing, Analytical models: Constant fringe (blue) and Variable fringe (red). FEA model (orange) agrees well with the variable fringe model.

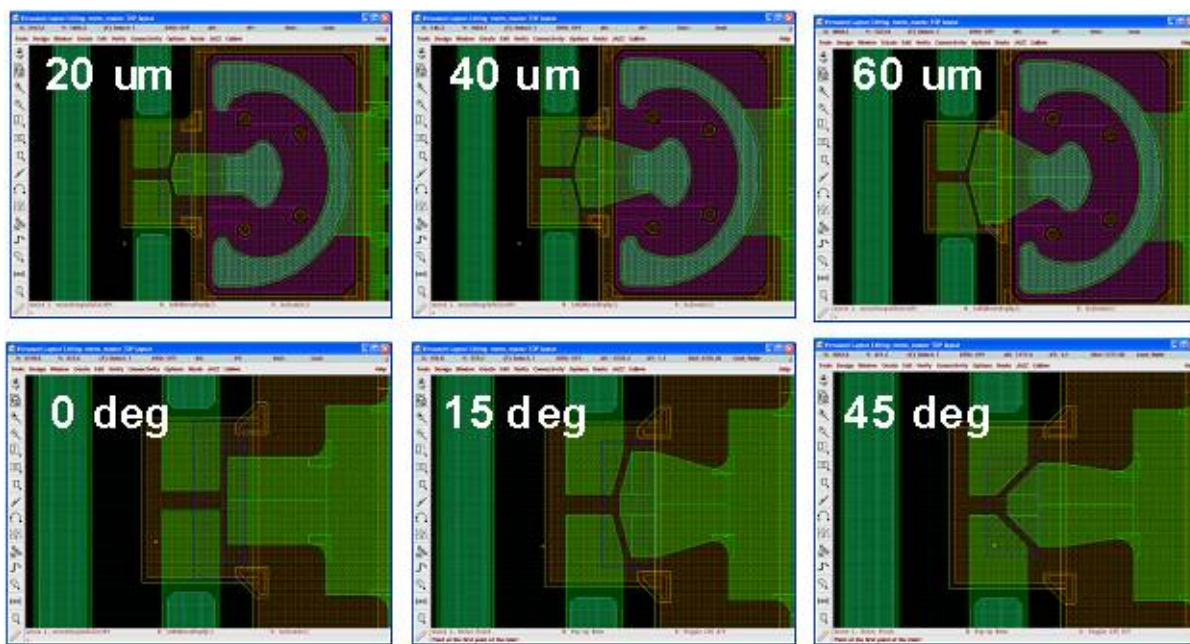


Figure 3.15: Different configurations of the head with width and angle variations.

Contact resistance of the switch is a function of force and area [52]. To study this, the width and contact angle of the head were varied as shown in figure 3.15. The variation of the width and contact angle did not have any substantial effect on the contact resistance. This experimental results for this exercise is discussed in more detail in section 3.4.2.

3.3 Fabrication Challenges

In the initial fabrication run, the actuator electrodes were designed with a $3.8 \mu\text{m}$ drawn standoff gap between them when the switch was closed (contact gap = 0). However, following fabrication, designed gap was found to be insufficient, causing the electrodes to short before head contact due to the following:

- (a) The sidewall Au overplate between contacts was thinner and more non-uniform than expected (figure 3.16 a), reducing the actual stand-off gap between the electrodes;
- (b) A positive Ni sidewall slope combined with a protruding electroplating seed layer at the electrode base (figure 3.16 b) further reducing this standoff gap; and,
- (c) stress gradient in the Ni resulted in a downward deflection of the contact head (figure 3.16 c) combined with 2), further reducing the actual standoff gap.

In the second fabrication run, the sidewall Au was thicker and much more uniform (fig. 3.16 d) and a drawn standoff of $4.8 \mu\text{m}$ was sufficient to prevent this electrode shorting and realize working actuators. The fixed and movable electrodes will not self pull-in up to approximately 100 V, since electrode spring constants are much greater than the spring constant of the serpentine spring.

The topography of the switch was measured using a profilometer and the contact head was found to be drooping down by an average of $6 \mu\text{m}$ for multiple devices across several die (fig. 3.16 c). Coventor [49] was used to simulate this effect by introducing stress gradients in

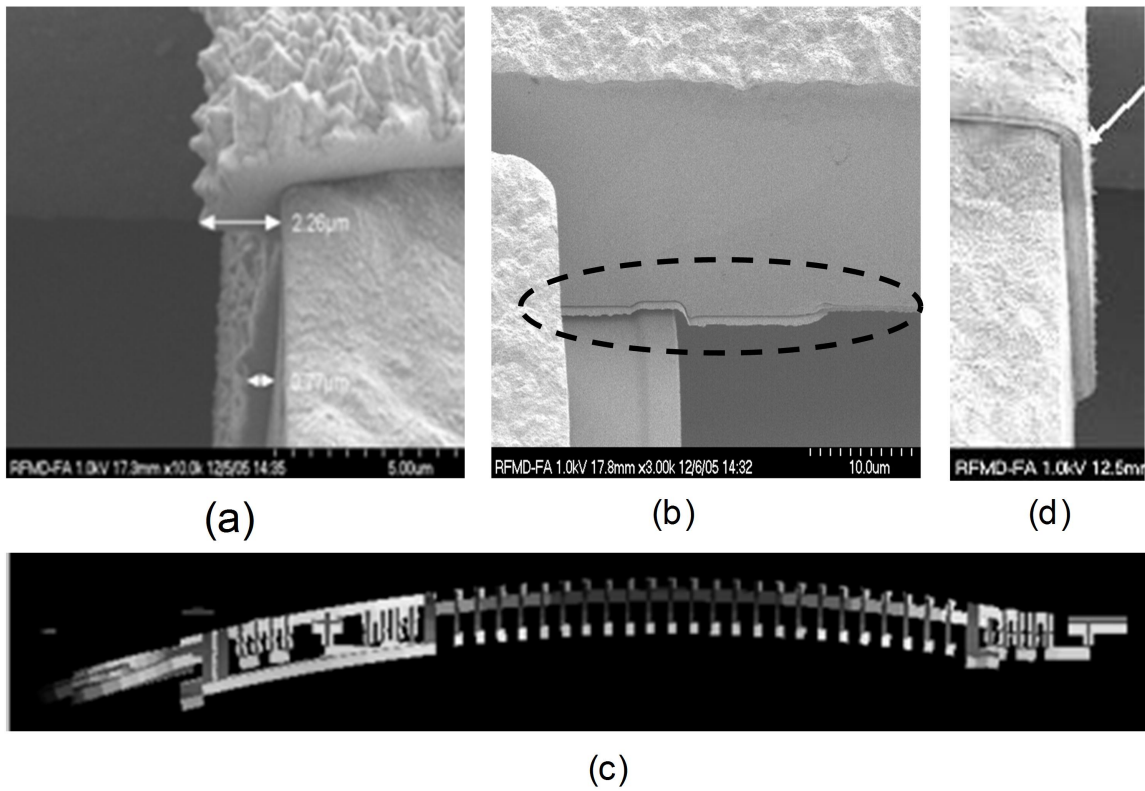


Figure 3.16: a) Au overplate on Ni sidewall b) bottom of Ni electrode showing electroplating seed layer c) Coventor FEA simulation of stress gradient d) uniform overplate.

x and y thru the thickness of the switch metal layer. The amount of droop in the simulation was matched to the measured value by varying the value of stress gradients. The fringe capacitance was then extracted from the experimental results after accounting for the stress gradients and the proximity of the Si surface 25 μm beneath the switch after KOH etch. This conductive ground plane underneath the switch has a significant influence on the fringe capacitance. This information was used to more accurately model the fringe factor in the analytical model.

3.4 Electrical Performance

The analytical model presented in section 3.2 accounts for the influence of side-wall angle on the performance of an electrostatic lateral actuator. The measurement results are discussed in the next few sub-sections.

3.4.1 Actuation Voltage Measurements

The new analytical model (that accounts for both sidewall angle in the electrodes and in the springs, as well as the effect of variable electrostatic fringing) was compared with an FEA model as shown in figure 3.14. The sidewall angles, α , used in the model for electrode and spring are 2° and 1.5° respectively. These angles were estimated by taking cross-sections using Focused Ion Beam (FIB) on different switches across the die (see figure 3.4). The difference in side-wall angle for the electrodes and springs may be attributed to the difference in their aspect ratios or local plating line/space density. The drawn width of the electrode was 10 μm and that of the spring was 8 μm . The height of the structure was 20 μm . The drawn electrode and non-electrode gaps were 13 and 21 μm respectively. The measured top gaps after fabrication were about 13.25 μm and 21.25 μm . This is consistent with a measured electrode top width of about 9.75 μm compared with the drawn width of 10 μm . Figure 3.17 illustrates the drawn dimensions versus actual dimensions. The spring constant of the

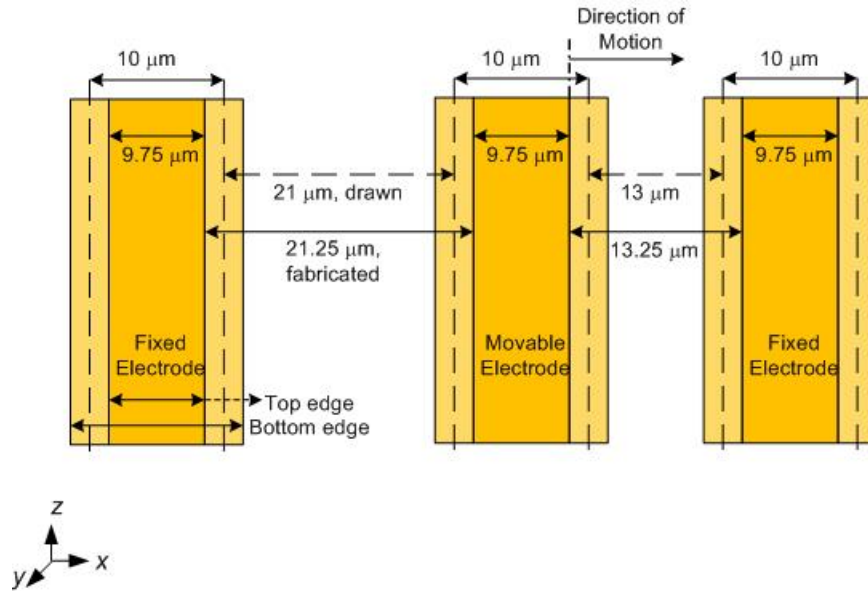


Figure 3.17: The above schematic depicts the top view of the movable and fixed electrodes. The dashed edges are the drawn mask dimensions and the solid edges are the fabricated switch dimensions.

switch is calculated to be $4.8\ \text{N/m}$ after taking into account the side-wall angle of 1.5° and an adjusted top-width of $7.8\ \mu\text{m}$ instead of the drawn $8\ \mu\text{m}$.

Figure 3.18 compares the measured, analytical, ideal (drawn dimensions) and FEA generated CV curves of the switch under study. The ideal model under predicts the pull-in voltage as compared to the other methods used. The measured result (black) falls somewhat short of the analytical and FEA results (red, orange). Possible explanations include differences in the sidewall angles and electrode gaps used in computation compared to that of the measured device. Also, no attempt was made to measure the Young's Modulus of the electroplated Nickel and the assumed magnitude may vary significantly from the actual value. Future work could include more accurately characterizing the Young's modulus of electroplated Ni to improve the fit between modeled and measured CV curves.

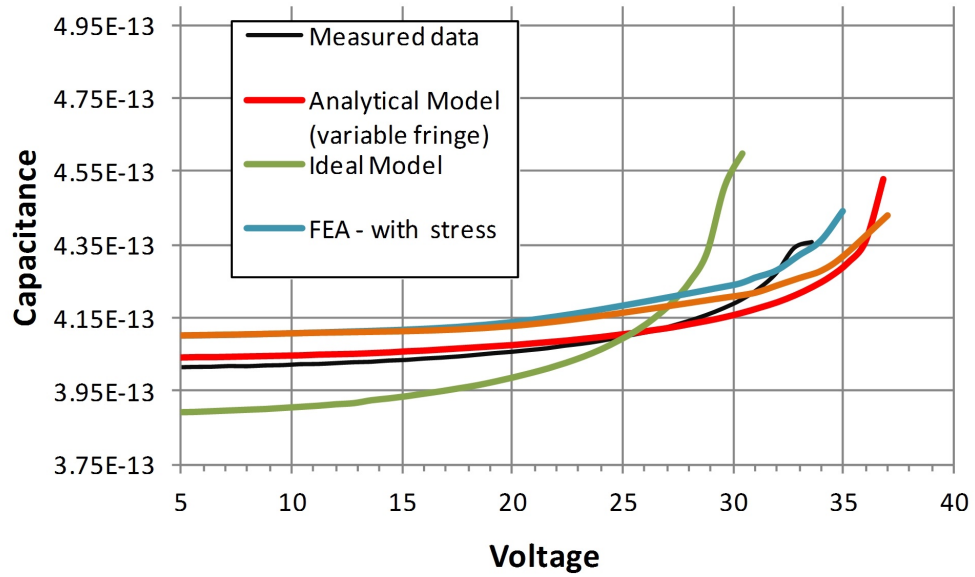


Figure 3.18: Plot of CV curves comparing, Measured data (blue), Ideal Model (green), Analytical Model (red) and FEA models with and without stress (blue and orange).

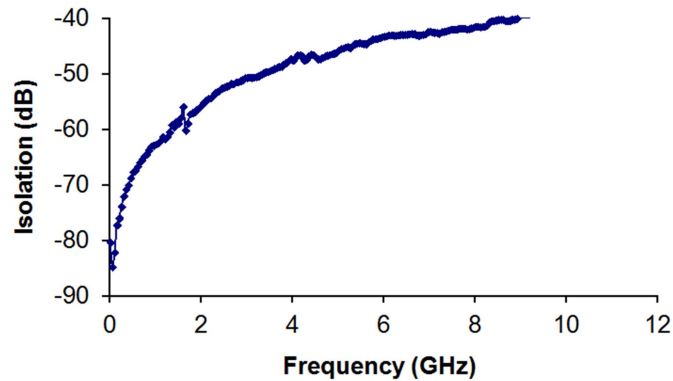


Figure 3.19: Switch Isolation with Si undercut on a high ρ substrate.

		ρ (Ωcm)	
		5000	2
Si Undercut	yes	-55	-32
	no	-50	-26
# contact heads (no actuator)	1	-45	-27
	2	-53	-29
	4	-63	-30

Figure 3.20: Isolation study of multiple heads: Varying Si undercut and substrate resistivity (ρ) measured in dB at 2 GHz.

3.4.2 Isolation and Insertion Loss Measurements

Variations of contact angle and width had very little impact on signal isolation. A typical isolation plot for a single head design is shown in figure 3.19. Multiple heads in series improve isolation by 8 dB per head for high substrates. Substrate coupling is more dominant in low ρ substrates as summarized in figure 3.20. Si undercut improves isolation for both high and low ρ substrates by more than 3 dB. Variations in design of contact area did not have measurable impact on contact resistances as mentioned in section 3.2.4. One possibility is that contact surfaces exhibit surface roughness and when two surfaces are brought together, they make contact at discrete asperities (high points) [53]. The number of asperities of similar height and applied force determines the contact resistance. Studies of contact physics suggest that asperity radii are on the order of $0.1 \mu\text{m}$ [54]. Contact at only a few asperities presents a contact area much less than the drawn head area. After fabrication the switches had very high contact resistances ($K\Omega$). The contact had to be conditioned in order to reduce the resistance. The initial high contact resistance is attributed to surface contaminants from the ambient (moisture) and also from wet chemical processing steps. To clean the contact, the switches were subjected to O_2 plasma for 10 minutes. After that, a current of 1 mA was forced through the contact with the voltage compliance set to 50 V. The measurements were made in an N_2 ambient. Based on the applied actuation voltage, the I-V curves of the switches had

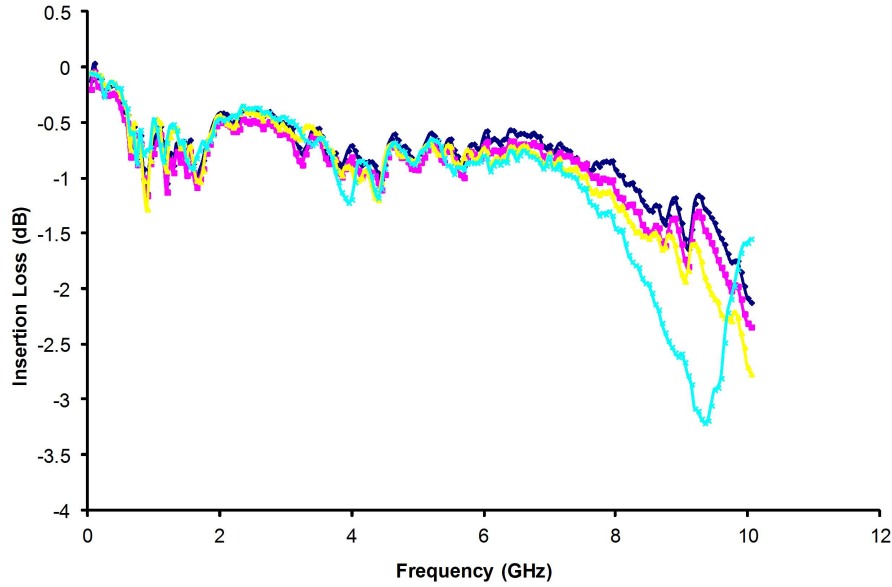


Figure 3.21: Insertion loss plots of actuators with different contact heads.

sharp break down voltages (voltage peaks labeled B.V as shown in figure 3.22). The surges in voltages constitute a cleaning mechanism at the contact for which the physics is not fully understood [54]. It is possible that high voltages force charge through the contaminant layer creating a conduction path on the asperity in contact. Similar measurements were reported by Kurabayashi *et al.* [54]. They also conditioned the contact with voltage and current before resistance measurements. For metal contacts, Holm has expressed the contact spot temperature T_c as a function of contact voltage V_c as

$$T_c = \sqrt{\frac{V_c^2}{4L} + T_o} \quad (3.23)$$

where $L = 2.45 \times 10^{-8} W\Omega/K^2$ is the Lorentz constant and T_o is the ambient temperature [53]. A 450 mV drop at the contact corresponds to $1063^\circ C$, the melting point of gold. The observation of high breakdown voltages shown in figure 3.22 along with a lack of observed ablation or welding of the Au contact implies that material at the contact is not only metal but also may include some contaminants. Detailed studies of contact contamination can be

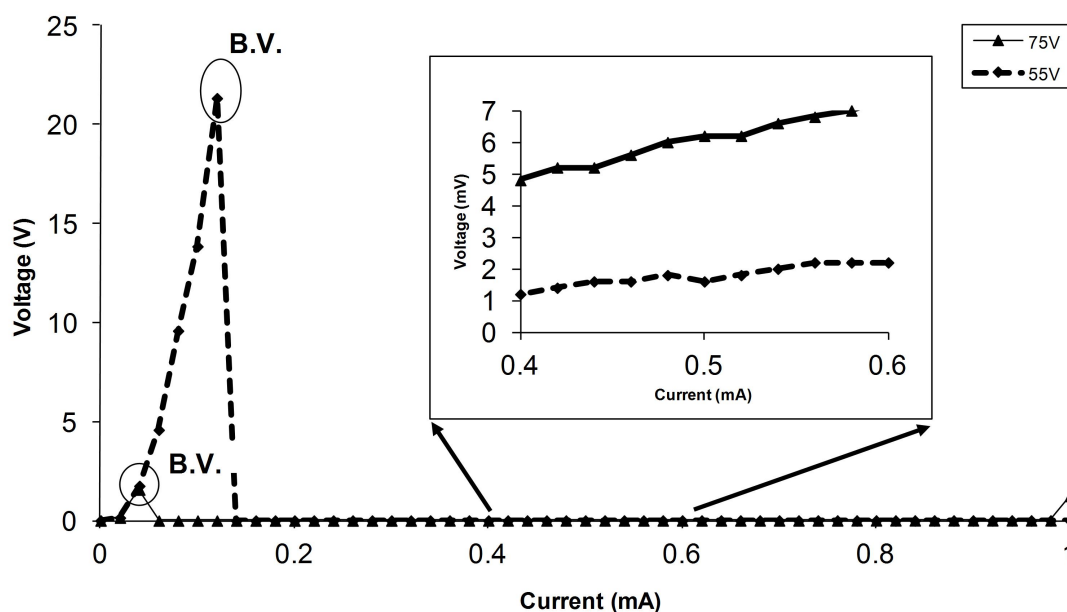
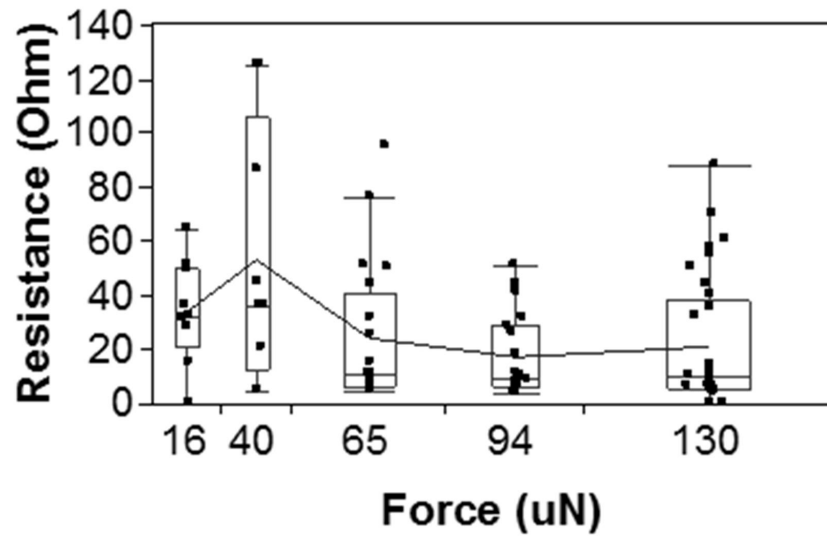
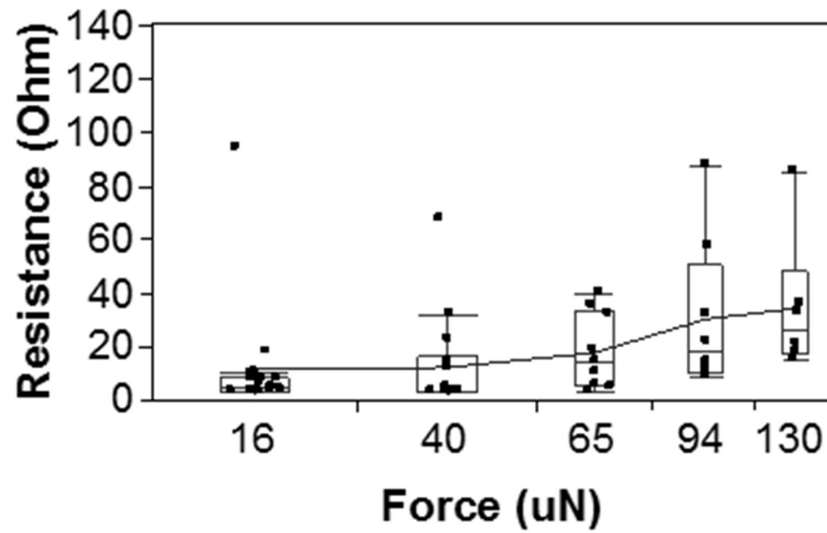


Figure 3.22: I-V curves showing Break down Voltages (B.V) at the contact for high and low actuation voltages.

found in [55], [56]. Best case insertion loss after conditioning is shown in figure 3.21. There is little or no difference between different contact heads. Figure 3.23 is a plot of contact resistance versus force. Measurements were made after conditioning the contact. In figure 3.23a, the mean values of resistance generally decrease with increasing force. This is the expected trend for metal to metal contact [57]. Figure 3.23b summarizes devices that had breakdown voltage peaks on the IV curves even after conditioning. Mean resistance tends to increase with increased force. The cause for this behavior is not well understood at this point. However, measured break down voltages were higher with lower contact forces and lower with higher contact forces. The lowest resistance measured reported in figure 3.23a was about 1Ω for a two sided contact.



(a)



(b)

Figure 3.23: Force vs contact resistance without (a) and with (b) an observed breakdown voltage.

3.5 Summary

An analytical model for a variable gap lateral contact MEMS switch that accounts for the process non-idealities has been developed. The process non-idealities considered are the trapezoidal cross-sections (sidewall angle α) for electrodes and springs (instead of rectangular) and the droop in the switch carriage and fixed electrodes along their length due to gradients of in-plane stress thru the thickness of the released layer combined with the conductor plane underneath the switch. The effect of electrostatic forces due to fringing fields was also modeled as a function of the time varying gap instead of a constant fringe factor.

Equations 3.10 & 3.15 predict the influence of side-wall angle on the single sided and double sided capacitance of the switch. The electrostatic forces can be modeled using equations 3.12 & 3.16 for both single sided and double sided electrode configuration, respectively. As expected, both the forces and capacitances increase with the increase in α . The serpentine spring is modeled using the principles of simple beam bending and Castigliano's Energy method. The energy method matches with the FEA simulations for rectangular cross-sections better than the simple bending method. The effect of sidewall angle on the spring is also modeled analytically and the energy method matches with the FEA within 6 % accuracy. The spring constant K_x increases with the increase in α .

The influence of side-wall angle on the switch displacement can be modeled using equations 3.13 & 3.17 for a single sided and double sided cases respectively. The effect of side-wall angle on pull-in voltage is modeled taking into account the trapezoidal cross-sections of both electrodes and springs. For the given switch dimensions and angles of electrodes and springs it is shown that V_{PI} decreases with increase in α when K_x is held constant, but if the influence of α on K_x is accounted for, V_{PI} increases with α .

Finally the effects of fringing fields on the values of capacitance, electrostatic forces and pull-in voltage are modeled as a function of the moving gap in addition to the sidewall angles and are presented in equations 3.21 and 3.22. By accounting for electrostatic fringing as a

constant, the model under predicts the value of pull-in voltage as compared to modeling the fringing fields as a function of the variable gap (equation 3.22).

The developed model helps designers predict the capacitances, forces, travel distances before pull-in, spring constants and eventually pull-in voltages of electrostatically actuated structures with inclined side-wall angles. The analytical model estimates the above parameters and matches well with the FEA simulations. This considerably reduces the simulation time for such analysis. Finally, the contact resistance measurements of these unpackaged switches show that the contact contamination is a detrimental issue, and packaging of MEMS switches in a hermetic environment is essential for high performance RF applications.

Chapter 4

Dynamic Pull-in Phenomenon in a Variable Gap Lateral Contact RF MEMS Switch

Pull-in constitutes the transition between the ON- and OFF-states of MEMS switches. In the context of microswitch actuation, the two methods of actuation are static and dynamic actuation. In the static actuation case, the structure is actuated by a DC voltage and pull-in voltage is referred to as the *static pull-in* V_{SP} . Pull-in is caused due to the departure from system equilibrium once the applied voltage exceeds the pull-in voltage. The assumption here is that the DC voltage is applied gradually and not applied instantaneously as a step-function. It is a broader term used to describe the device pull-in when dynamics of the device are being considered. Dynamics can change the device response through transients in switch motion due to a sudden disturbance, a magnification of switch motion due to a resonant external excitation, or both. Application of a sudden disturbance (a step voltage) can decrease the pull-in voltage by 8 % - 16 % below the static pull-in [58]. It refers to applying an AC signal whose frequency is equal to the natural frequency of the switch. Pull-in occurs because the transients in the system drive the state vector (displacement and

velocity) close to the stable manifold of the saddle, which is referred to as Resonant pull-in. Resonant pull-in involves actuating the switch with an AC waveform ($V_{AC} = v_{ac} \cos \Omega t$), where Ω ($2\pi f$) is close to the resonant frequency of one of the vibrating modes of the switch.

In this chapter the variable gap lateral switch introduced in Chapter 3 is actuated by sweeping the amplitude and/or frequency close to its mechanical resonant frequency. Studies indicate that actuating a parallel plate actuator with an AC waveform increases the travel range and reduces the dynamic pull-in voltage, $V_{DP} = \sqrt{V_{DC}^2 + \frac{v_{ac}^2}{2}}$ compared to $V_{SP} = V_{DC}$ (static pull-in voltage) [59]. V_{DC} in the expressions represents the amount of DC voltage required to enable pull-in and its value is different in both the cases.

In [59], an actuation frequency determined from the 1st mode of resonance is employed, and is kept fixed as the actuating voltage conditions are varied. In this work, the non-linear resonant frequency of the system, which varies with the applied V_{DC} and v_{ac} voltages, is used for the switch actuation. The applied V_{DC} value sets the overall non-linearity co-efficient and increasing v_{ac} shifts the resonant frequency further to the left of the linear resonant frequency, since the electrostatic softening non-linearity dominates. Actuating the switch by sweeping the frequency around its non-linear resonance, drives the switch to pull-in with the smallest AC amplitude v_{ac} . The following sections elaborate on the experimental results showing voltage savings while operating as a resonant switch. For a certain range of DC and AC voltages the switch operates as an impact oscillator which is illustrated in section 4.1.3. Such an impact oscillator could have potential applications as a switching device in a class E PA (Power Amplifier). Finally, for the first time, the timing response of the resonant pull-in phenomenon is reported.

4.1 Experimental Results

The lateral contact switch under study is a variable gap actuator with an asymmetric electrode configuration [46] to facilitate motion in one direction. The switch, as described in

Chapter 3, includes fixed and movable electrodes, springs, and a contact head. The voltages (DC and/or AC) are applied between the fixed and movable electrodes to actuate the switch. The material properties and the dimensions of the switch are given in Table 3.1.

The nominal resonant frequency of the switch at various V_{DC} values are determined by observing the resonance under a microscope, while simultaneously applying v_{ac} amplitudes (\approx 100s of mV to 2 volts). The microscopic images of one set of measurements are shown in figure 4.1. The AC frequency (Ω) was swept while looking for small amplitude lateral oscillations. The first three modes of resonance are visually observed by carefully sweeping the AC frequency (Ω). Figure 4.2 shows Coventor (FEA) [49] simulations of the first three resonant modes of the switch which match with the experimentally observed values of resonant frequency. Figure 4.3 is a plot of experimentally observed values of resonant frequency vs. V_{DC} and it can be seen that resonant frequency decreases with increasing V_{DC} and static pull-in is highlighted as a point on the curve when the natural frequency is zero.

4.1.1 Regions of Operation

Depending on the amount of travel between the contact head and signal lines and the values of actuating voltages, the actuator operates in one of the following regions:

- (a) Resonator: The mechanical structure oscillates at a frequency that corresponds to a resonance mode.
- (b) Resonant or Dynamic Switch: The mechanical structure begins to oscillate, but quickly the oscillations become unstable and the pull-in ensues.
- (c) Impact Oscillator: The mechanical structure is oscillating at a frequency while opening and closing a switch path.

For any sinusoidally excited electrostatic actuators, the amplitude of oscillation is a function of the sinusoidal forcing function ($\propto V_{DC} \cdot v_{ac}$). Given a V_{DC} value, the oscillation amplitude

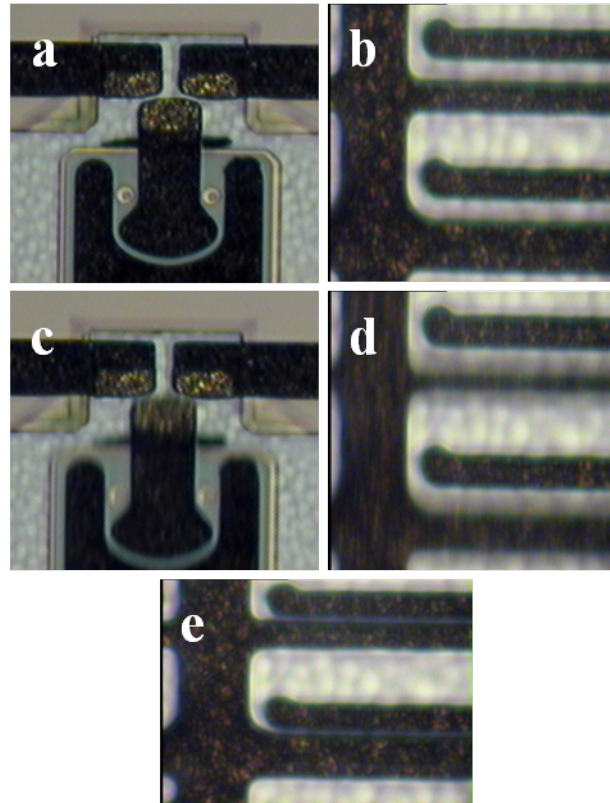


Figure 4.1: (a, b) Optical images of the contact head and electrodes when no voltage is applied. (c, d) Matching images with V_{DC} (20 V) and v_{ac} RMS (1.8 V) applied to resonate the switch before pull-in. (e) Finally, images of pull-in after sweeping the frequency around resonance when DC (20 V) and v_{ac} RMS (1.82 V). The standoff gap at the electrodes is seen when the switch is closed.

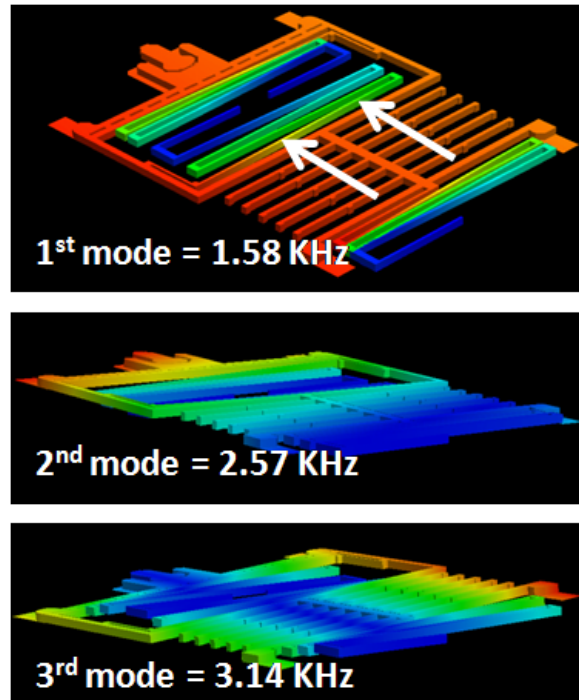


Figure 4.2: First three resonant modes of the switch under study. Finite Element Simulations were done using Coventor [60].

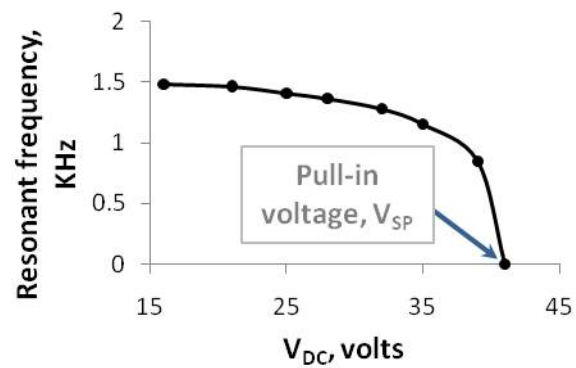


Figure 4.3: Linear resonant frequency vs. V_{DC} for the first mode of resonance.

increases linearly with small v_{ac} but increases non-linearly for larger v_{ac} based on the amount of non-linearities present in the system [41]. Also, when the switch is actuated with a sine wave, the travel range is beyond $1/3^{rd}$ of the gap before pull-in. It is believed the kinetic energy of the system during AC excitation allows the system to travel beyond the static equilibrium, reaching large amplitudes of motion without pulling in [59]. Hence for the case of AC excitation, the amount of switch travel before pull-in is determined by the values of applied voltages, both DC and AC. It was observed that the gap at the contact head w.r.t to that of the electrodes, along with the applied voltages, determines if the switch acts as an impact oscillator or as a resonant switch. Two different switches are tested for this study; one with a $V_{SP} = 36 V$ and another with a $V_{SP} = 41 V$. The second switch was observed to have less travel between the contact head rest position (when no voltage is applied) and the signal line compared to the first switch and hence has a higher probability of working as an impact oscillator. This is because of the variation in the thickness (1 - 3 μm) of the sidewall plating at the contact head (see Figure 3.16a & d). Figure 4.4 is a plot of V_{DC} vs. v_{ac} that maps different regions of operation of the switch with $V_{SP} = 41 V$. For low v_{ac} values the switch acts as a simple resonator responding to AC excitations as indicated in figure 4.4. The resonance is easily observed under a microscope as explained earlier. At higher values, it acts as either a resonant switch or an impact oscillator. The operation and actuation voltages (DC and AC) to enable resonant switching and impact oscillations are discussed in subsequent subsections.

4.1.2 Resonant Switch

Two methods were used to achieve resonant pull-in:

- (a) Amplitude sweep
- (b) Frequency sweep

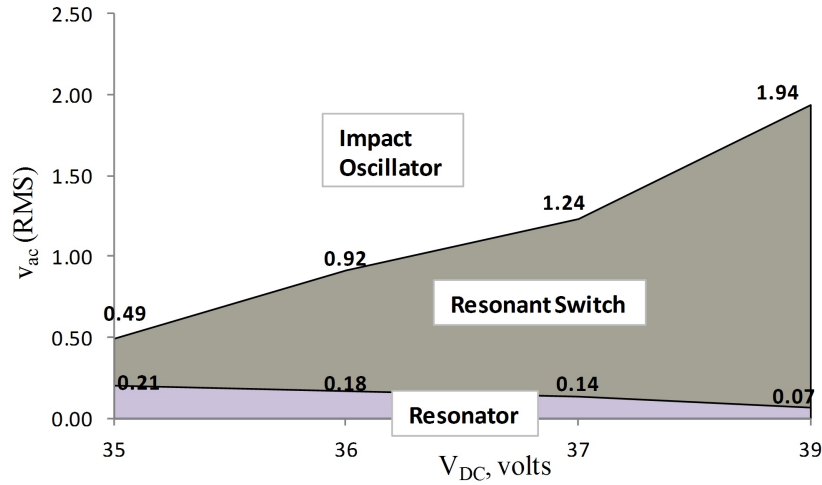


Figure 4.4: Different regions of operation for the switch with $V_{SP} = 41$ V. The combination of V_{DC} and v_{ac} values maps to different regions of operation. The frequency of operation corresponds to the first mode of resonance. The numbers on the plot correspond to the different v_{ac} (RMS) values.

In method (1), a fixed V_{DC} voltage was applied while the amplitude v_{ac} was increased till the switch pulled in while holding the excitation frequency Ω constant, approximately equal to the natural (linear) frequency of the switch. This was the actuation method reported in [59]. The linear resonant frequencies of the switch for the first mode of resonance for various V_{DC} values are given in figure 4.3. However, in method (1) the switch is not actuated at these exact frequencies for different V_{DC} values, instead a nominal frequency is chosen for the different V_{DC} values while only varying the amplitude slowly until pull-in is reached. The value of the frequency is set by either sweeping it up (low to high) or down (high to low) to that point and then the amplitude is slowly varied until pull-in occurs.

In method (2) the same V_{DC} was applied but the excitation frequency Ω was swept (both high to low and low to high) while holding the amplitude v_{ac} constant. v_{ac} was incrementally increased in small steps and the above process repeated until pull-in occurred. Figure 4.5 plots the combination of (V_{DC}, v_{ac}) values that cause dynamic (resonant) pull-in using both the methods mentioned above.

To illustrate the amount of $v_{ac,RMS}$ saved at a given applied V_{DC} in method (2) as compared to method (1), a V_{FOM} is defined:

$$V_{FOM} = V_{DC} + v_{ac,RMS} \quad (4.1)$$

The percentage savings in method (2) compared to method (1) is computed using $(V_{SP} - V_{FOM})/V_{SP}$ % is shown in figure 4.6. $V_{FOM}(= V_{DC} + v_{ac,RMS})$ is used in illustrating savings of $v_{ac,RMS}$ applied instead of $V_{DP}(= \sqrt{V_{DC}^2 + \frac{v_{ac}^2}{2}})$ for the following reason. Table 4.1 shows the values of V_{FOM} and V_{DP} for an applied voltage of 16 V V_{DC} and the corresponding v_{ac} values that cause pull-in using both the methods. Method (1) requires 16.2 V of v_{ac} amplitude while method (2) requires only 4.5 V of v_{ac} amplitude (71 % reduction), resulting in V_{DP} values equal to 19.7 and 16.3 V (17 % reduction) respectively. Even though the net V_{DP} values are less than V_{FOM} , V_{DP} does not reflect the true reductions achieved in v_{ac} values and hence V_{FOM} is used to illustrate these reductions.

<i>Method</i>	V_{DC}	v_{ac}	$v_{ac,RMS}$	V_{FOM}	V_{DP}
(1)	16 V	16.2 V	11.4 V	27.4 V	19.7 V
(2)	16 V	4.5 V	3.2 V	19.2 V	16.3 V

Table 4.1: V_{FOM} vs. V_{DP}

Both the resonant actuation methods accrue voltage savings compared to static pull-in. The V_{SP} for the switch in figure 4.5 was measured to be 36 V. In figure 4.5 the dotted curve was obtained by method (1), keeping the frequency constant ($f = 1.216$ KHz) and the solid line was obtained by method (2), increasing the amplitude of v_{ac} in small steps and also sweeping the AC frequency around the resonance at specific V_{DC} values until pull-in. The frequency values denoted in figure 4.5 indicate the values at which pull-in occurred during the frequency sweep. The frequency values increase with decreasing V_{DC} . The reason for this two fold; a linear (spring) and a non-linear (spring) effect. The linear phenomenon is purely due to the effect of V_{DC} multiplying the linear term (x) in the Taylor series expansion

of capacitance as shown in 2.24 and plotted in figure 4.3 [61]. It should be noted that, the v_{ac} frequency values for the solid line in figure 4.5 are lower than the one's shown in figure 4.3 for the corresponding V_{DC} values. This is due the non-linear spring effect which results in a negative electrostatic non-linearity that shifts the peak frequency to the left as shown in figure 2.12. The final point on the dotted curve, does not follow the overall trend, because the frequency was swept up (low to high) instead of down (high to low) to obtain pull-in.

From figure 4.5 it seems that for the frequency value of 1.216 KHz, the curves (solid and dotted) have different values of v_{ac} for the same V_{DC} value. The reason for this is three fold. First, the solid and the dotted curves in figure 4.5 are generated for discrete V_{DC} values and are joined together by a dotted line as shown in the figure. Second, the bottom curve is tuned to the appropriate frequency to achieve maximum displacement for the set V_{DC} values. If the value of V_{DC} in the top curve was swept in extremely small steps, there will be a value that corresponds to v_{ac} at that frequency which will be closer to the bottom curve. Third, apart from the frequency value, the very act of sweeping the frequency also has an effect on the pull-in, which is why the switch pulls in for a lower value of v_{ac} . The rate of frequency sweep does not allow the switch transients to settle before the next frequency is reached and this might have role in triggering pull-in [58]. In this case, the sweep was done manually and was not a controlled for a certain specific rate. This concept of sudden change in frequency or frequency sweep in switch pull-in is further addressed in chapter 5. Finally, figure 4.7 plots the percentage savings of pull-in voltage $V_{DP}(= \sqrt{V_{DC}^2 + \frac{v_{ac}^2}{2}})$ compared to $V_{SP}(= V_{DC})$ operating at the optimal non-linear resonant frequency proposed in method (2).

4.1.3 Impact Oscillator

The operation of the lateral switch as an *impact oscillator* is explained in this subsection. When the switch is actuated with a sine wave, the travel range is beyond $1/3^{\text{rd}}$ of the gap before pull-in and will increase with the increase in V_{AC} amplitude. The switch was tested using method (2) described in subsection 4.1.2. If the amount of possible travel between

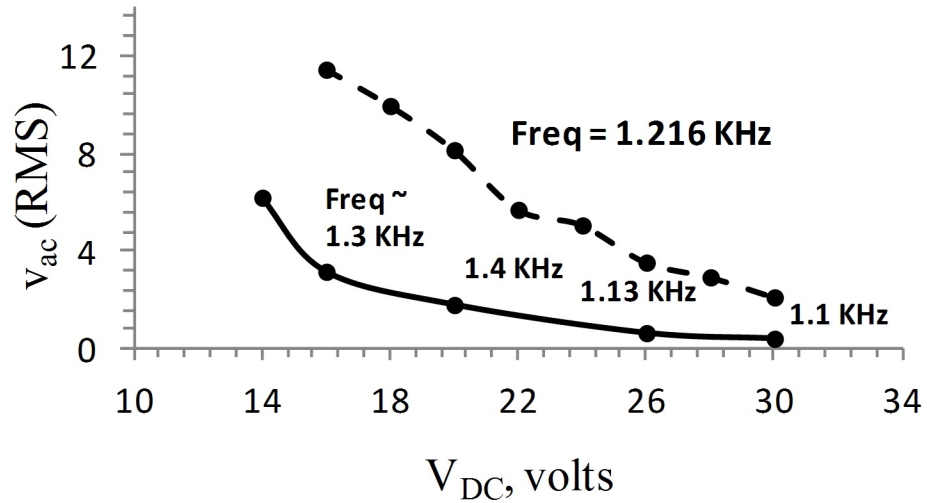


Figure 4.5: a) Combination of V_{DC} and v_{rmax} values for a constant frequency (dotted line) and for varying frequency (solid line).

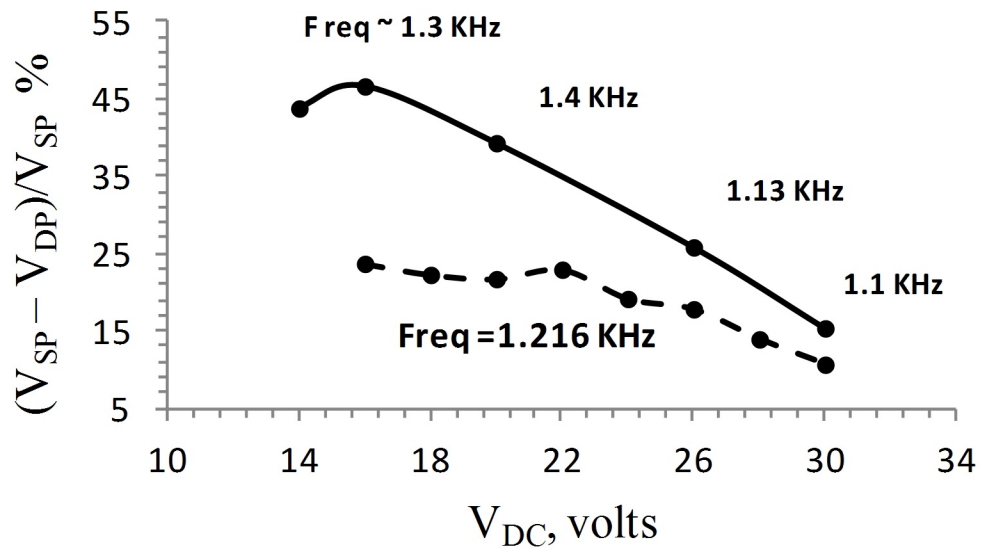


Figure 4.6: Shows the percentage savings of V_{FOM} w.r.t static pull-in for varying amplitude (dotted line) and varying frequency (solid line).

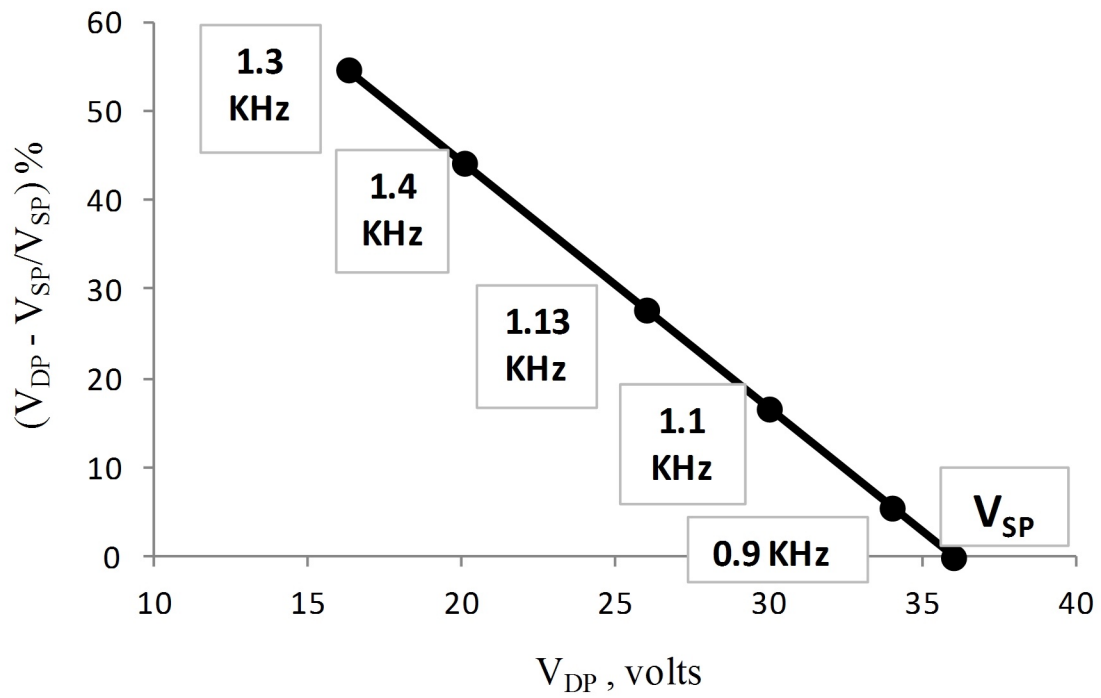


Figure 4.7: Shows percentage savings w.r.t to V_{DP} and V_{SP} .

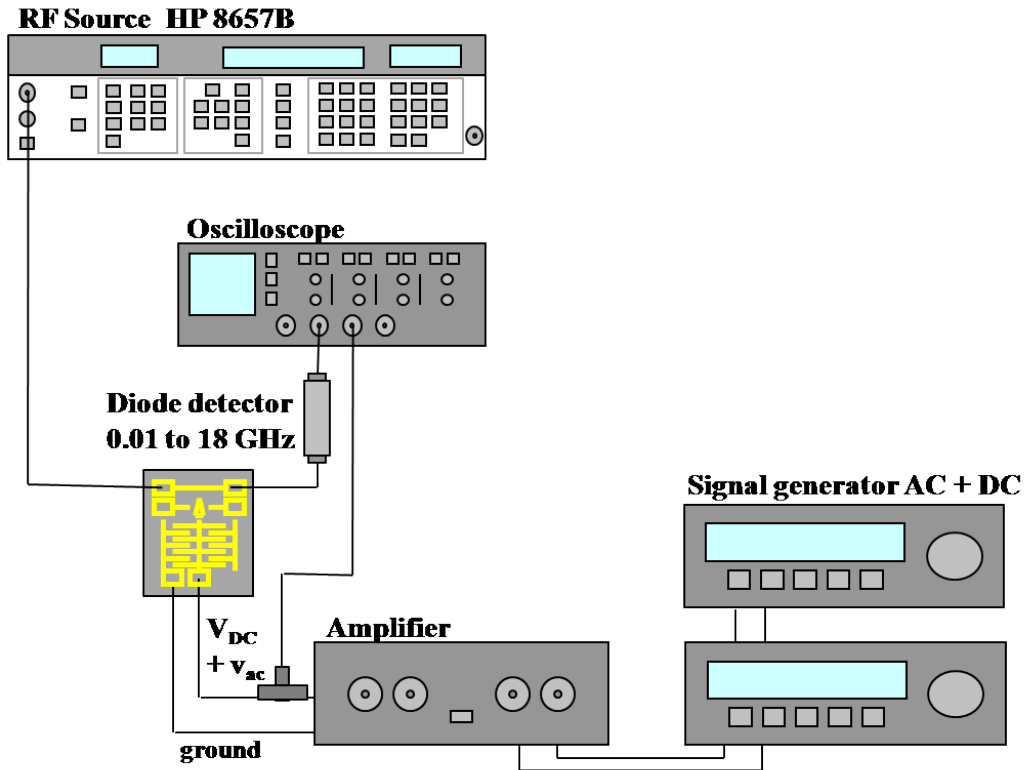


Figure 4.8: Timing measurement set-up also used to capture switch response as an impact oscillator.

contact head in the rest position and the signal lines is smaller than the travel needed to reach instability for a given DC + AC bias condition, the switch will not pull-in. In this case, the contact head travels across the gap and bounces against the signal lines but the switch does not remain closed; rather, it continues to oscillate. Since the excitation frequency (Ω) is equal to the non-linear resonant frequency of the switch; the head will open and close the contact gap at this frequency. Figure 4.8 shows the experimental set-up for the measurement. Figure 4.9 is an oscilloscope screen capture of the switch's response at the output of the diode detector shown in figure 4.8. The frequency of AC excitation and the diode detector output are equal to 1.45 KHz for the plot in figure 4.9. The impact oscillator described above is similar to the *resoswitch* presented in [62]. Figure 4.4 maps V_{DC} values under which the switch operates as an impact oscillator or as a resonant switch.

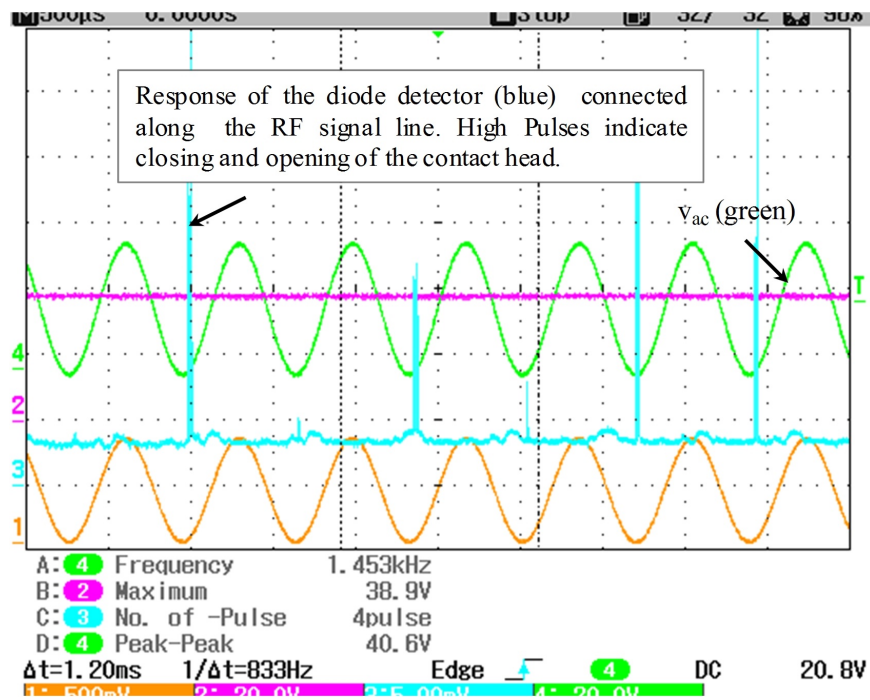


Figure 4.9: Oscilloscope capture of the switch's response at the output of the diode detector. The switch is resonating while opening and closing the contact head.

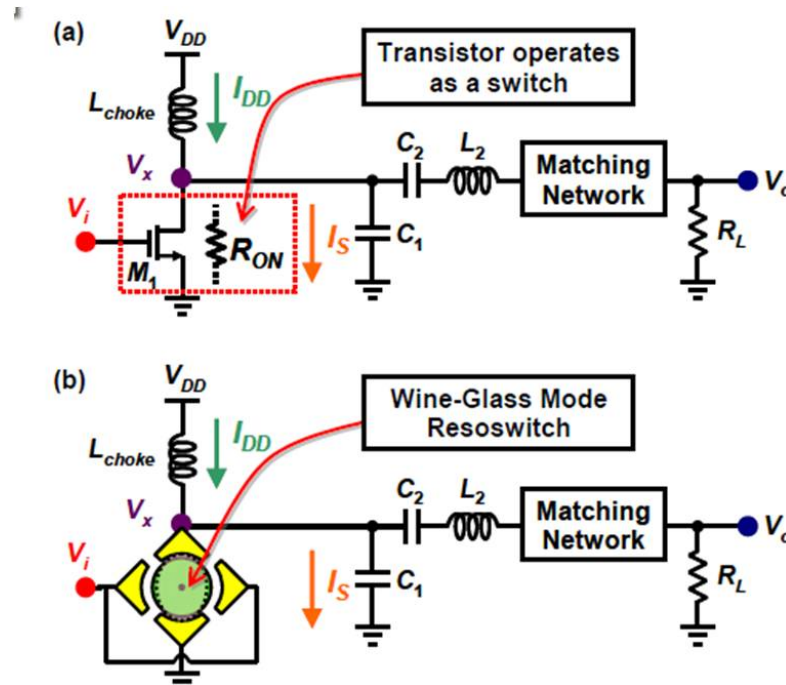


Figure 4.10: Circuit topologies of (a) a conventional Class E amplifier using a transistor switch device; and (b) one simplified rendition of the proposed Class E amplifier utilizing a “resoswitch” as driven by the input ac signal v_i after [62].

The impact oscillator is capable of switching on and off at the excitation frequency of v_{ac} . It could be used as a resonant switch as a part of a Class E Power Amplifier (PA) as demonstrated in [62]. Figure 4.10 shows a schematic implementation of a similar switch in a Class E PA [62]. The disk resonator in figure 4.10 can be replaced with the impact oscillator described above.

4.1.4 Timing Response

Finally, the timing response of the lateral switch is experimentally investigated for the case of resonant pull-in. The experimental setup is the same as in section 4.1.3 shown in figure 4.8. Figure 4.11 shows plots of response times of the switch for both static actuation and (V_{DC} only) and dynamic actuation ($v_{ac} + V_{DC}$). Since the force exerted on the switch is

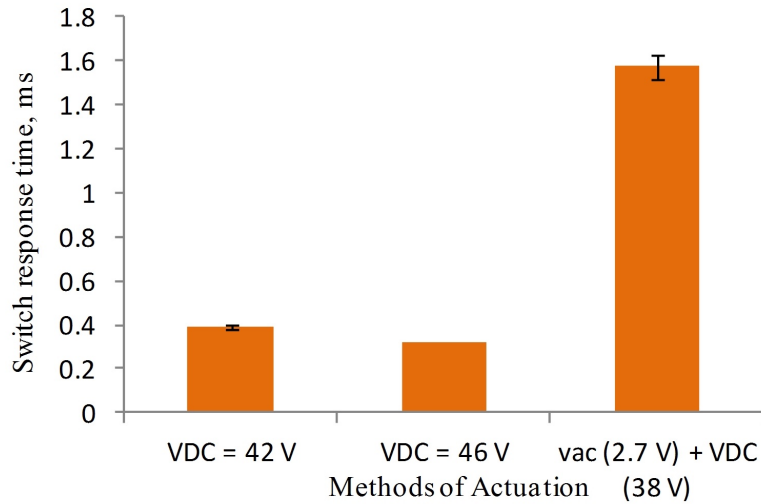


Figure 4.11: Average values of switch response times for different methods of actuation.

directly proportional to voltage squared, the switching time is inversely proportional to this value. For a pure DC actuation, the switching time will be inversely proportional to V_{DC}^2 . Hence, the response time for DC actuation voltage of 46 V is smaller than that for 42 V as seen in figure 4.11. For the case of AC + DC actuation (resonant pull-in), oscillatory motions precede the actual pull-in as seen in figure 4.11, and hence the switching times are slower. The response times are measured as the difference between the time $V_{DC} + v_{ac}$ is applied and the level change in the diode detector output.

4.2 Summary

The dynamic or resonant pull-in phenomenon has been demonstrated for a variable gap lateral contact switch that was designed and built in a commercially available MEMS foundry technology as described in Chapter 3. The use of the resonant pull-in technique reduces the overall voltage required to actuate the switch. There is an additional reduction of in $v_{ac,RMS}$ by applying an AC actuation signal at the correct non-linear resonant frequency. The best case savings using this method is $\approx 50\%$ compared to the static case. However, the timing

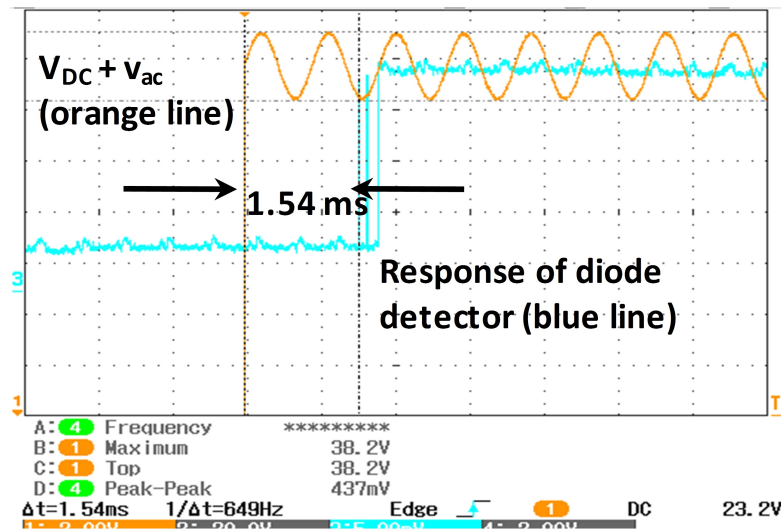


Figure 4.12: Scope capture of the switch’s response when a $V_{DC} + v_{ac}$ is applied. An RF signal is switched through a diode detector to measure the response time.

response for resonant pull-in has been experimentally shown to be slower than the static actuation, which represents a trade off in the use of resonant actuation to lower voltage requirements. For adjacent bias conditions to the resonant pull-in condition, the switch will act as an impact oscillator which could have applications in switching RF power amplifiers.

In the next chapter design fabrication and measurement results of dynamic pullin of shunt capacitive switches are discussed.

Chapter 5

Dynamic Actuation of Shunt Capacitive MEMS Switches

This chapter focuses on the fabrication of shunt capacitive MEMS switches followed by detailed experimental and modeling results of resonant or dynamic switching of these switches. The fabrication process was developed using Virginia Tech's MicrON clean room facilities. The switches were fabricated on high resistivity Si substrates. Nayfeh, *et al.* [63] have previously presented a theoretical analysis on the behavior of fixed-fixed microbeams and showed that dynamic pull-in occurs at a much lower voltage than static pull-in. Fargas-Marques, *et al.* [59] studied pull-in under resonant excitation to derive analytical expressions for static and dynamic pull-in voltages and validated their results experimentally using a parallel-plate actuator configuration. In this prior work, the excitation frequency was fixed in the experiments and simulations. In this chapter, it is shown that the net voltage reduction with dynamic actuation can be enhanced by tuning the excitation frequency.

The shunt capacitive switch design is detailed in section 5.1 followed by the fabrication process in section 5.2. A mathematical model is developed to describe the response of the switch to electrostatic (dynamic) actuation in section 5.3. The model accounts for the effects of midplane stretching of fixed-fixed microbeams and the associated non-linearities. In

section 5.4 a parameter estimation method is introduced as a method to estimate the bridge dimensions, internal axial stresses, and system damping. Finally, a measurement procedure is presented with experimental results showing voltage savings in section 5.5. Practical methods for implementation of dynamic pull-in and estimates of the associated switching time are presented in section 5.7.

5.1 Shunt Capacitive Switch Design

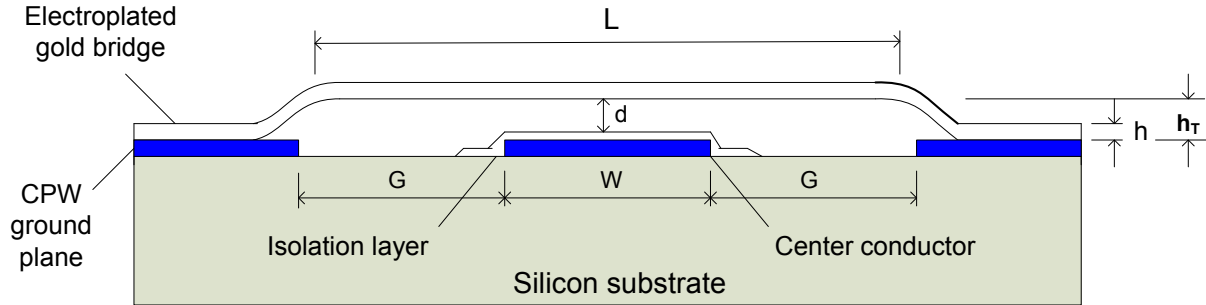


Figure 5.1: A cross-section schematic of the shunt microswitch structure.

The switch structure in figure 5.1 is composed of an electroplated gold bridge fabricated on top of a 50-ohm CPW line on a 500 μm Si substrate with a 2 μm thick LPCVD silicon nitride isolation layer. The CPW signal line (width W) carries both the actuation signal and the RF signal. The gap between the signal line of the CPW and each of the ground lines is denoted as G . An SEM picture depicting the switch and CPW is shown in figure 5.2. In the case of dynamic pull-in, the actuating signal is a combination of both DC and AC waveform. A bias-T is used to combine DC and AC voltage components from separate power sources and obtain an overall waveform. Table 5.1 below describes various switch designs that were fabricated by varying the dimensions of the CPW center conductor (W), shunt bridge (length L , width b) and the gap (d) between the bridge and the signal line, while maintaining the characteristic impedance (Z_o) of the CPW line around 50 ohms. All the electromagnetic simulations were done using Zeland IE3D [64] software package.

d (μm)	b (μm)	Z_o (Ohm) for W = 75 μm	Z_o (Ohm) for W = 60 μm	Z_o (Ohm) for W = 40 μm
1	20	48.9	49.0	-
	35	47.8	47.9	-
	50	46.0	46.8	47.2
2	20	49.2	49.0	-
	35	48.4	48.1	-
	50	47.1	47.8	-
3	20	49.4	49.0	-
	35	48.8	48.5	-
	50	47.7	48.1	48.1

Table 5.1: Tabulation of various switch designs.

5.2 Fabrication process

Figure 5.3 illustrates the fabrication procedure developed in-house. The CPW lines were first defined by using a liftoff process by evaporating 500/4500 Å thick layer of Cr/Au. A positive resist was used to create a lift-off profile by pre-dipping the soft baked photo-resist in the TMAH based developer solution. This creates a light insensitive layer on top of the photo-resist which does not develop at the same rate as the rest of the resist. This creates a lip along the developed outer edges as seen in figure 5.4 that facilitates clean lift-off.

A 1000 - 1200 Å SiN dielectric (PECVD) layer was then deposited using a dual-frequency Trion system. Silicon Nitride was deposited from Silane (SiH_4) and ammonia (NH_3) forming Si_3N_4 as shown in equation 5.1. The PECVD process parameters for deposition of Si_xN_y are shown in table 5.2.

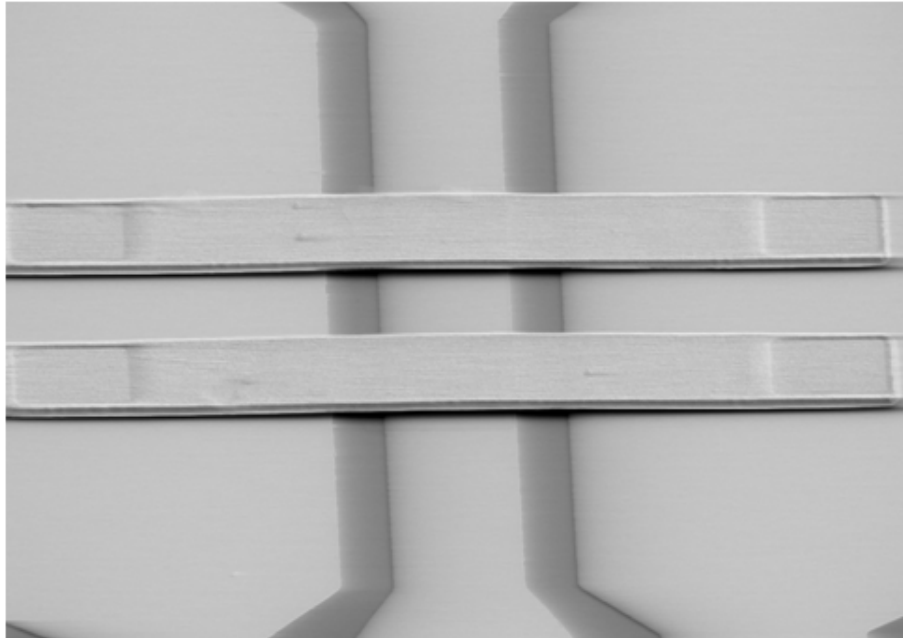
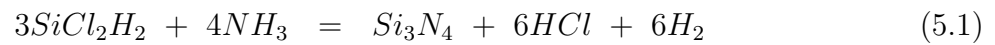


Figure 5.2: A schematic of the shunt microswitch.



Pressure (mT)	600
RF Power(13.56 MHz)	175
Low Frequency (LF) Power (100 KHz)	50
Temperature (°C)	350
Flow rate (Silane/Ammonia) (sccm)	600 / 15
Deposition Rate (Å / min)	500

Table 5.2: Process parameters for nitride deposition on a TRION PECVD system.

A Trion RIE system was used to dry etch the and pattern the nitride on top of the signal line using an SF_6 plasma. The RIE process parameters used for etching the nitride are shown in table 5.3.

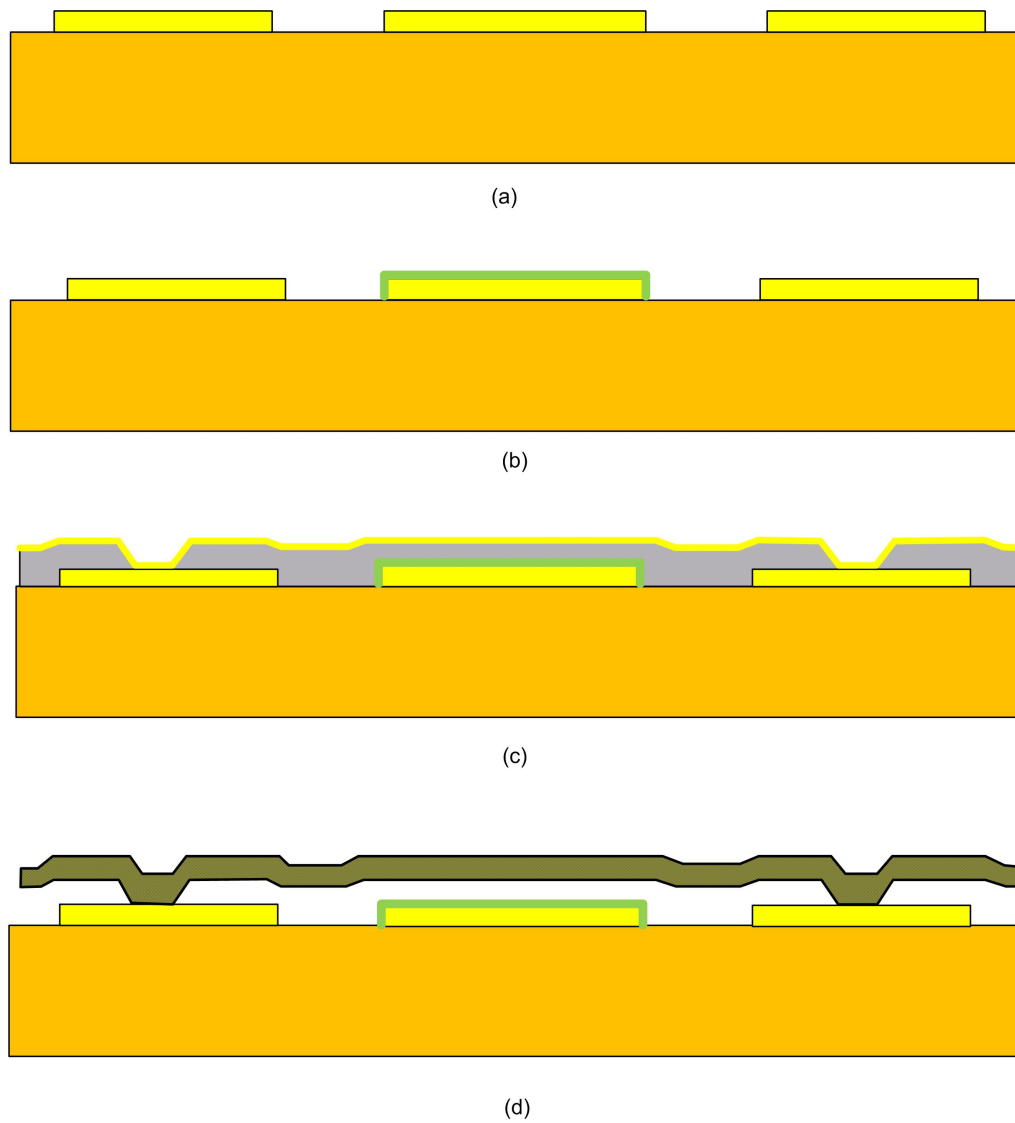


Figure 5.3: Fabrication procedure of the capacitive shunt switch. (a) CPW patterning (b) Dielectric layer - PECVD SiN deposit and patterning (c) Sacrificial S1813 layer with anchor patterning; seed layer (Ti/Au) by evaporation (d) Au electroplating and sacrificial layer removal followed by Critical Point Dryer release.

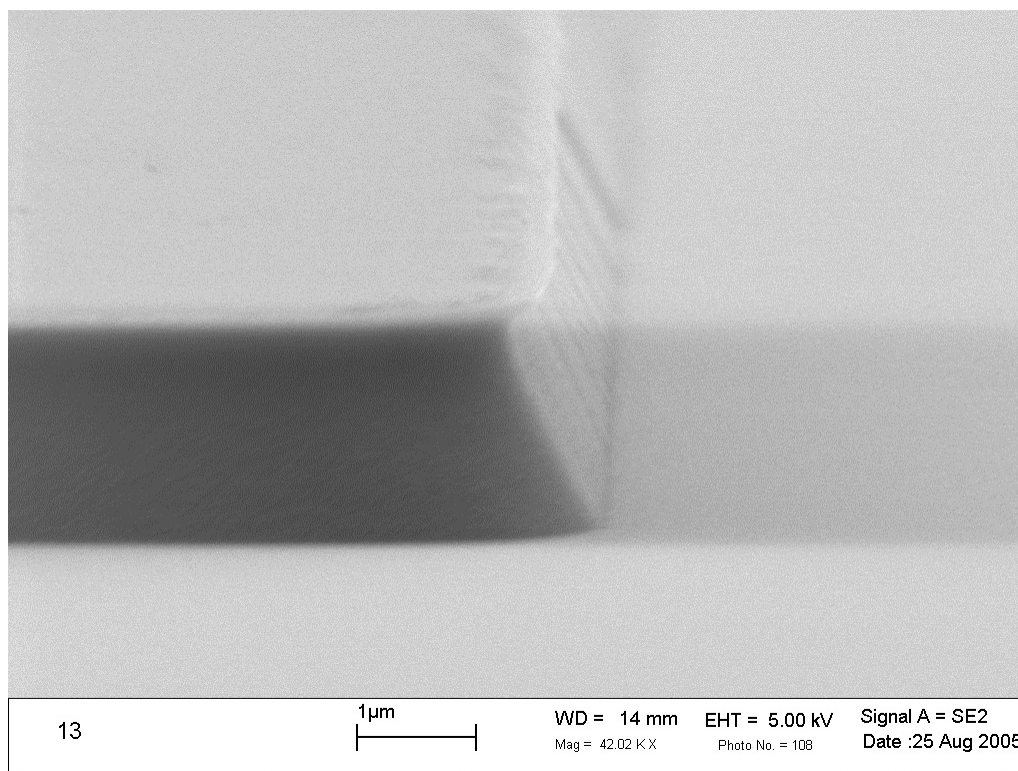


Figure 5.4: An SEM picture of a positive photo-resist with a lift-off profile.

Following that, a 1.5 - 2.0 μm -thick sacrificial layer of photo-resist (S1813) was deposited and patterned. This sacrificial layer defines the gap (d) between the switch membrane and the signal line and also defines the anchors as shown in figure 5.3(c). A blanket deposition of 450/750 \AA Ti/Au seed layer was then evaporated and the photo-resist was patterned on top to define the switch thickness and its width. The beams were then electroplated using a Au electroplating station with the wafer as the cathode and platinum electrodes as an anode in a commercially available Au plating bath (TSG-250 from Transene). A constant current source was used to make sure that the plating current, and hence the plating current density, remained a constant. To ensure uniformity and smooth plating surfaces, the plating current density was maintained between 5 – 10 mA/cm^2 . The plated thickness of the Au layer was limited to between 1.5 to 2.0 μm , since thicker beams require higher V_{DC} values to pull-in. After electroplating the bridges, the seed layer (Ti/Au) was wet etched before removing the sacrificial layer using a photo-resist stripper. Finally the switches were released

Pressure (mT)	150
RF Power(13.56 MHz)	350
Low Frequency (LF) Power (100 KHz)	50
Temperature (C)	350
Flow rate (SF_6 / O_2) (sccm)	45 / 5
Etch Rate ($\text{Å} / \text{min}$)	2000 Å

Table 5.3: Process parameters for nitride deposition on a TRION RIE system.

using a Critical Point Dryer from Tousimis to avoid switch failure from high forces exerted at the bottom of the microbeam due to surface tension during drying (stiction). To avoid this effect, the sample can be brought from the liquid phase to the gas phase without crossing the liquid-gas boundary on the phase diagram (figure 5.5). Supercritical drying moves around the transition, on the high-temperature, high-pressure side. This path from liquid to gas does not cross any phase boundary, instead passes through the supercritical region, where the distinction between gas and liquid ceases to apply. Densities of the liquid phase and vapor phase become equal at critical point of drying. In this process, the switches were gently rinsed in DI water immediately after removing it from photoresist stripper. Isopropyl alcohol (IPA) is first used to wash away all the water, exploiting the complete miscibility of these two fluids. The IPA is then washed off with methanol which is essentially the liquid inside the critical point dryer. The methanol is then washed away with high pressure liquid carbon dioxide. The liquid carbon dioxide is then heated until its pressure goes beyond the critical point, at which time the pressure can be gradually released, allowing the gas to escape and leaving a fully dried structure. Figure 5.6 shows SEM pictures of switches released with and without using a critical point dryer.

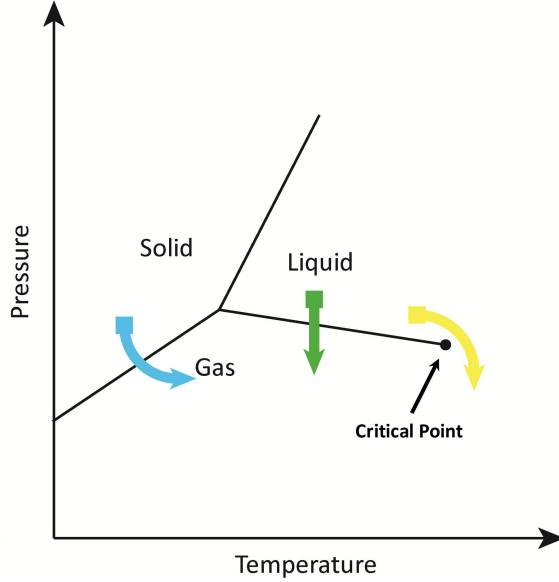


Figure 5.5: Supercritical drying (yellow arrow) goes beyond the critical point of the working fluid in order to avoid the direct liquid-gas transition seen in ordinary drying (green arrow).

5.3 Shunt Switch Model

The MEMS shunt switch is modeled as a straight beam of uniform cross-section and homogeneous material with mass per unit length m , length L , thickness h , width b , cross-sectional area A and moment of inertia I , and modulus of elasticity E . The bridge is anchored to two ground lines on either side of a co-planar waveguide (CPW) transmission line of width W and held at a distance d above the CPW as shown in figure 5.1. The theoretical modeling work in this chapter is an extension of the work in [63], [65].

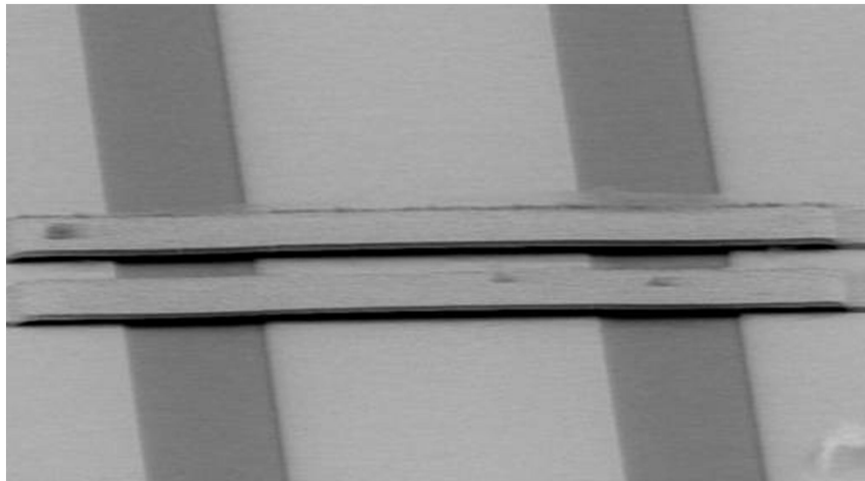
The equation of motion governing the response of a clamped-clamped microbeam to electrostatic actuation is given by [63]

$$m \frac{\partial^2 \hat{w}}{\partial \hat{t}^2} + \hat{c} \frac{\partial \hat{w}}{\partial \hat{t}} + EI \frac{\partial^4 \hat{w}}{\partial \hat{x}^4} = \left[\hat{N} + \frac{EA}{2L} \int_0^L \left(\frac{\partial \hat{w}}{\partial \hat{x}} \right)^2 d\hat{x} \right] \frac{\partial^2 \hat{w}}{\partial \hat{x}^2} + \frac{1}{2} \frac{\epsilon b_e v^2}{(d - \hat{w})^2} S_t \quad (5.2)$$

where $\hat{w}(\hat{x}, \hat{t})$ is the transverse deflection of the microbeam, \hat{N} is the axial tensile force. The sources of damping in the switch are energy losses through supports and acoustic losses to air, as well as structural damping represented by the viscous damping coefficient and



(a)



(b)

Figure 5.6: SEM pictures showing switches released a) without and b) with critical point dryer.

squeeze-film damping due to the air trapped under the bridge, represented by the coefficient \hat{c} . The voltage difference between the bridge and the CPW is defined as

$$v(\hat{t}) = V_{\text{DC}} + V_{\text{AC}} \cos(\hat{\Omega}\hat{t}) \quad (5.3)$$

The unit-step function $S_t(\hat{x})$ accounts for the incomplete overlap between the CPW and the bridge. $\hat{x} = 0$ when $L = 0$.

$$S_t(\hat{x}) = \begin{cases} 1 & \text{for } \frac{L-W}{2} \leq \hat{x} \leq \frac{L+W}{2} \\ 0 & \text{elsewhere} \end{cases} \quad (5.4)$$

To account for the electrostatic fringing field, the width of the microbeam \hat{b} is replaced with an effective width b_e [66] in the electrostatic force term

$$b_e = \left(1 + 0.65 \frac{d - \hat{w}}{\hat{b}}\right) \hat{b} \quad (5.5)$$

The non-dimensional variables used in this work are as follows,

$$x = \frac{\hat{x}}{L}, \quad w = \frac{\hat{w}}{d}, \quad \text{and} \quad t = \frac{\hat{t}}{T} \quad (5.6)$$

where T is a time scale, into eqns. (5.2) and (6.3), and obtain the non-dimensional equation governing the transverse motions of the bridge

$$\frac{\partial^2 w}{\partial t^2} + c \frac{\partial w}{\partial t} + \frac{\partial^4 w}{\partial x^4} = [N + \alpha_1 \Gamma(w, w)] \frac{\partial^2 w}{\partial x^2} + \alpha_2 \frac{v^2}{(1-w)^2} \left(1 + 0.65 \frac{1-w}{b}\right) S_t \quad (5.7)$$

subject to the boundary conditions

$$w(x, t) = 0 \quad \text{and} \quad \frac{\partial w(x, t)}{\partial x} = 0 \quad \text{at} \quad x = 0 \quad \text{and} \quad x = 1 \quad (5.8)$$

The integral operator $\Gamma(f_1, f_2)$ is defined as

$$\Gamma(f_1, f_2) = \int_0^1 \frac{\partial f_1}{\partial x} \frac{\partial f_2}{\partial x} dx \quad (5.9)$$

The non-dimensional parameters appearing in the equation are

$$\begin{aligned} b &= \frac{\hat{b}}{d}, & c &= \frac{\hat{c}L^4}{EIT}, & \alpha_1 &= 6\left(\frac{d}{h}\right)^2, \\ \alpha_2 &= \frac{6\epsilon L^4}{Eh^3d^3}, & N &= \frac{\hat{N}L^2}{EI}, & T &= \sqrt{\frac{mL^4}{EI}}, & \Omega &= \hat{\Omega}T \end{aligned} \quad (5.10)$$

The system equation, eqn. (5.7), is a nonlinear partial differential equation. The sources of nonlinearity in the system are midplane stretching and the electrostatic force. They are proportional to the nondimensional parameters α_1 and α_2 , respectively.

The Galerkin method is used to discretize the equation of motion into a set of nonlinearly coupled ordinary-differential equations [63]. First, the equation is multiplied by $(1-w)^2$ and the solution is assumed to be of form

$$w(x, t) = \sum_{i=1}^N \psi_i(x) q_i(t) \quad (5.11)$$

where $\psi_i(x)$ is a mode shape of the unactuated bridge, $q_i(t)$ is the corresponding generalized coordinate, and N is the number of modes retained in the expansion. The orthogonality condition between the mode shapes was used in the resulting equation to obtain the discretized system.

5.4 Experimental setup

A Polytec MSV-400 laser vibrometer [67] (figure 5.7) was used to measure the bridge motions. The laser vibrometer system uses the Doppler effect to measure the velocity or displacement of a point on the bridge. A helium neon laser beam is pointed at the target point and the back scattered laser light is measured using a photodetector. The spot size of the beam was 2 - 5 μm in diameter. The motion of the target point modulates the frequency or shifts the phase of the scattered laser beam. The frequency or phase shift is then measured and used to calculate the velocity or displacement, respectively, of the target point. The vibrometer is mounted on a Micromanipulator test station (as seen in figure 5.7). A vacuum port is

used to fix the test specimen to the chuck of the test station. A probe is used to carry the actuation signal to a pad at the end of the transmission line, while another probe is used to ground a pad connected to the two ground lines.

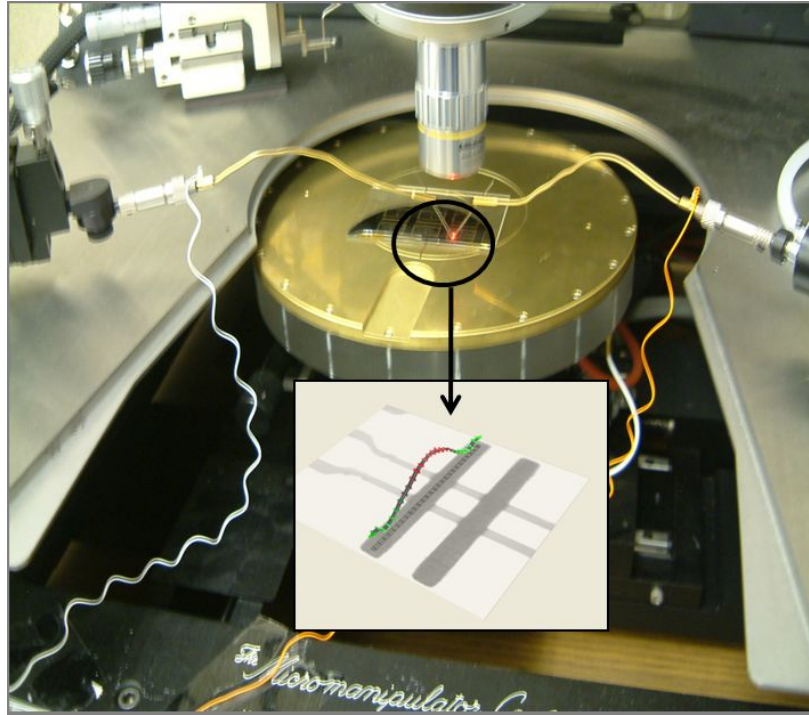


Figure 5.7: Shunt switch under testing.

5.4.1 Parameter Estimation

The model discussed in section 5.3 requires estimates of the beam dimensions and axial load to predict the switch behavior. A white light optical profilometer, Wyko-NT1100 [68], was used to obtain the beam surface topography shown in figure 5.8. The beam length and width listed in Table 5.4 were measured from this profile. The combined beam thickness and capacitor gap was also measured to be $h_T = h + d = 3.4 \mu\text{m}$. Further, initial estimates of the beam thickness \tilde{h} and capacitor gap \tilde{d} were obtained by measuring the height of the structural gold layer over the ground lines in the post or the anchor area.

The use of electroplating leads to surface roughness and uncertainties in the thickness h and

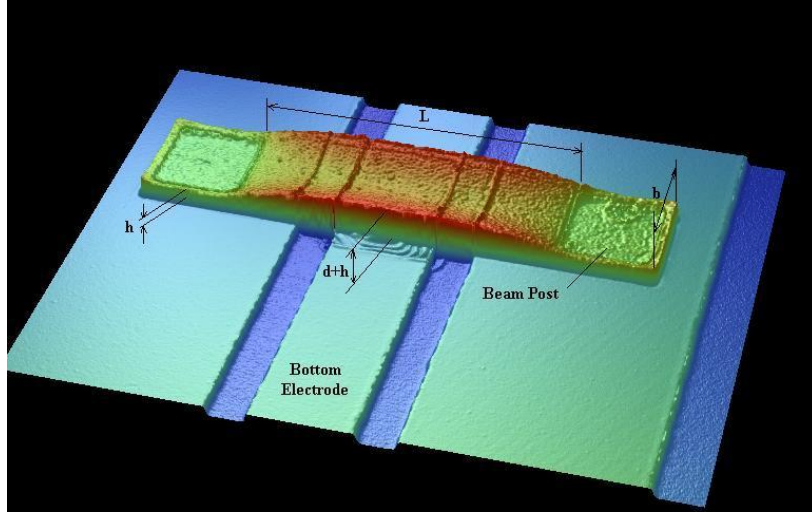


Figure 5.8: A 3-D picture of the beam profile using a white light profilometer.

vertical gap distance d . Residual stresses σ may also occur during fabrication resulting in axial forces in the bridge. A parameter identification routine, discussed below was developed to estimate these parameters by matching the experimental results to model predictions of the natural frequency as a function of the DC voltage.

To obtain the natural frequency-DC voltage curve experimentally, the switch was excited with a small AC voltage and a fixed DC bias V_{DC} . As the beam vibrated around the corresponding static equilibrium $w_s(x)$, the laser vibrometer was used to measure the velocity of the bridge midpoint. To take advantage of the reduced noise floor in the frequency domain, the amplitude of the midpoint velocity was obtained from the peak in the FFT at the excitation frequency Ω . The frequency of excitation was increased in discrete steps and when the maximum velocity amplitude was obtained, the excitation frequency was recorded as the natural frequency ω at V_{DC} . The bias voltage was then increased and this process was repeated sequentially to obtain the curve shown in figure 5.9.

The eigenvalue problem describing the free vibrations of the beam around a statically deflected position $w_s(x)$ is given by [65]

$$\phi_n^{iv} - [N + \alpha_1 \Gamma(w_s, w_s)] \phi_n'' - 2\alpha_1 \Gamma(w_s, \phi_n) w_s'' = \left(\omega_n^2 + \frac{2\alpha_2 V_{DC}^2}{(1 - w_s)^3} \right) \phi_n \quad (5.12)$$

where ϕ_n and ω_n are the mode shape and natural frequency of the n^{th} bending mode around the equilibrium position $w_s(x)$ subject to the boundary conditions, N is the axial tensile force and α_1, α_2 are defined in equation 6.4.

$$\phi_n = 0 \quad \text{and} \quad \phi_n' = 0 \quad \text{at} \quad x = 0 \quad \text{and} \quad x = 1$$

The second term on the right-hand side of equation (5.12) accounts for the drop in the natural frequency with increasing DC voltage seen in figure 5.9. For an unactuated bridge ($V_{DC} = 0$), equation (5.12) reduces to

$$\phi_n^{iv} - N\phi_n'' - \omega_n^2\phi_n = 0 \tag{5.13}$$

Inspection of equation (5.13) shows that the natural frequency ω_n depends solely on the axial force N at $V_{DC} = 0$. Therefore, N can be estimated by matching the natural frequency predicted numerically to that measured experimentally at the y-intercept of the natural frequency-DC voltage curve, figure 5.9. Assuming average gold density of $\rho = 19320 \text{ kg/m}^3$ and modulus of elasticity of $E = 80 \text{ GPa}$, the tensile stresses σ in the process was estimated as 17 MPa.

The initial estimates of the beam thickness \tilde{h} and capacitor gap \tilde{d} were used in the model described by equation (5.12), to calculate ω_n as a function of V_{DC} . The curve representing this function was then compared to the experimentally obtained curve and the values of \tilde{h} and \tilde{d} were updated iteratively until the difference between the experimental and numerically predicted curves fall within a predefined tolerance, Fig. 5.9. At this point, the values of \tilde{h} and \tilde{d} , shown in Table 5.4, were adopted as a refined estimate of the beam thickness h and capacitor gap d .

To summarize the previous results, the dimensions of the beam and the underlying fixed electrode measured using the white light profilometer in addition to the other estimated parameters are given in Table 5.4.

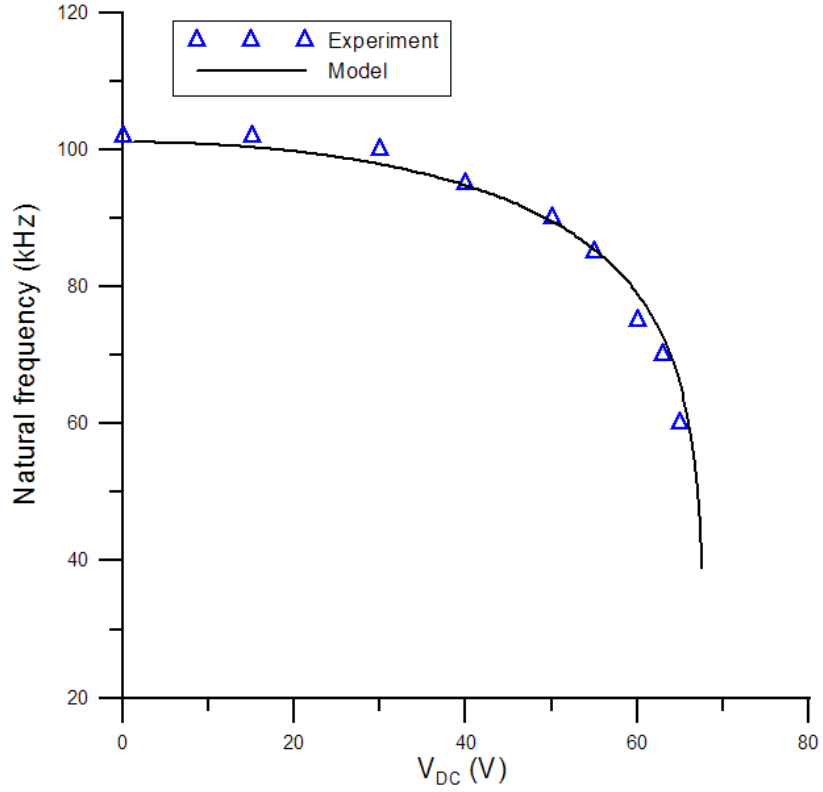


Figure 5.9: Variation of the fundamental natural frequency with DC voltage.

Table 5.4: Switch properties and dimensions.

L (μm)	b (μm)	h (μm)	d (μm)	E (GPa)	ρ (kg/m^3)	σ (GPa)
225	20	1.7	1.7	80	19320	17

5.4.2 Estimation of Q

The mechanical quality factor Q of the switch is the ratio of the energy stored in the bridge to the energy lost in one cycle of oscillation. The quality factor can be estimated experimentally from the frequency-response curve as the ratio of the resonance frequency (f_r) to the bandwidth at half-power level (Δf):

$$Q = \frac{f_r}{\Delta f} \quad (5.14)$$

Figure 5.10 shows the experimentally obtained frequency-response curve for the waveform ($V_{DC} = 10$, $v_{ac} = 17$) V. The curve was obtained by sweeping the excitation frequency from 75 to 130 kHz in small discrete steps. The velocity of the bridge midpoint was measured using the laser vibrometer after the transient part of the response due to the frequency shift had decayed. The FFT was obtained with the midpoint velocity averaged over 30 periods of the excitation frequency. The root-mean square of the velocity v_{RMS} was obtained from the peak in the FFT at the excitation frequency Ω . The quality factor was calculated to be 12.5 from this data using equation (5.14). This estimate lumps together all dissipation mechanisms in the switch.

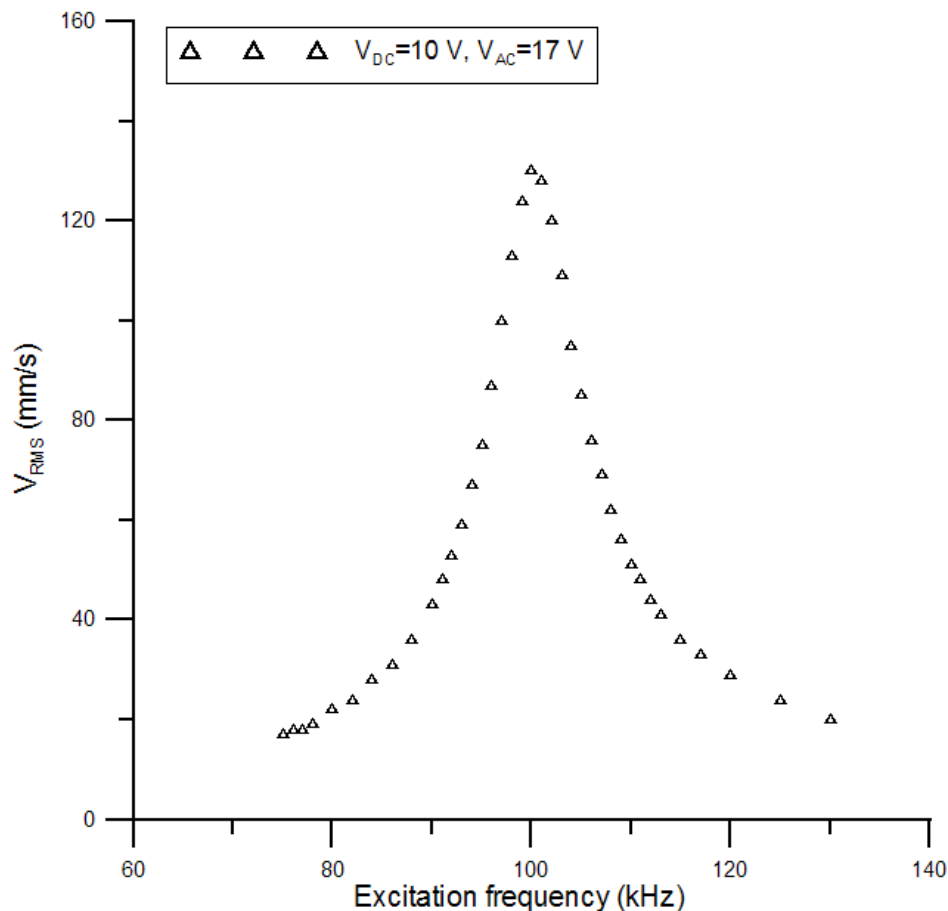


Figure 5.10: Experimental frequency-response curve for the RMS velocity of the beam midpoint at ($V_{DC} = 10$, $V_{AC} = 17$) V.

5.5 Dynamic Actuation Results

To trigger dynamic pull-in [63, 69], the bias voltage was set to a fixed value V_{DC} and the frequency of excitation was restricted to the neighborhood of the fundamental natural frequency ω_n of the switch design measured in section 5.4. Two procedures were used to induce dynamic pull-in:

- (1) *force sweep*: where the frequency of excitation was held at $\Omega = \omega_n$, while the amplitude v_{ac} was increased until dynamic pull-in occurred. This method is similar to that used by Fargas-Marques *et al.* [59].
- (2) *frequency sweep*: where v_{ac} was held constant, while the excitation frequency was swept up and down in the neighborhood of ω_n . The value of v_{ac} was then increased in small steps and the frequency sweeps were repeated until pull-in occurred.

Pull-in was detected as a sudden drop in the measured RMS velocity to the noise floor. The effective nonlinearity of the switch is composed of a *hardening* component due to midplane stretching in the bridge and a *softening* component due to the electrostatic field. The nonlinearity changes character from a positive hardening nonlinearity at low DC voltages to a negative and increasingly softening nonlinearity as the DC voltage increases. As the effective nonlinearity increases, regions of multivaluedness appear and expand in the frequency-response curves. As a result, the experimentally realizable part of the frequency-response curve is broken into a left and a right branch. A forward frequency sweep was used to obtain the left branch of the curve, while a backward frequency sweep was used to obtain the right branch of the curve.

Figure 5.11(a) shows the frequency-response curves obtained experimentally (diamonds) at $(V_{\text{DC}} = 20, V_{\text{AC}} = 27.5)$ V and numerically (solid lines) at $(V_{\text{DC}} = 24.5, V_{\text{AC}} = 26.5)$ V. Figure 5.11(b) shows the experimental frequency-response curve (diamonds) at $(V_{\text{DC}} = 50, V_{\text{AC}} = 6.5)$ V and the corresponding numerical curve obtained for $(V_{\text{DC}} = 56, V_{\text{AC}} =$

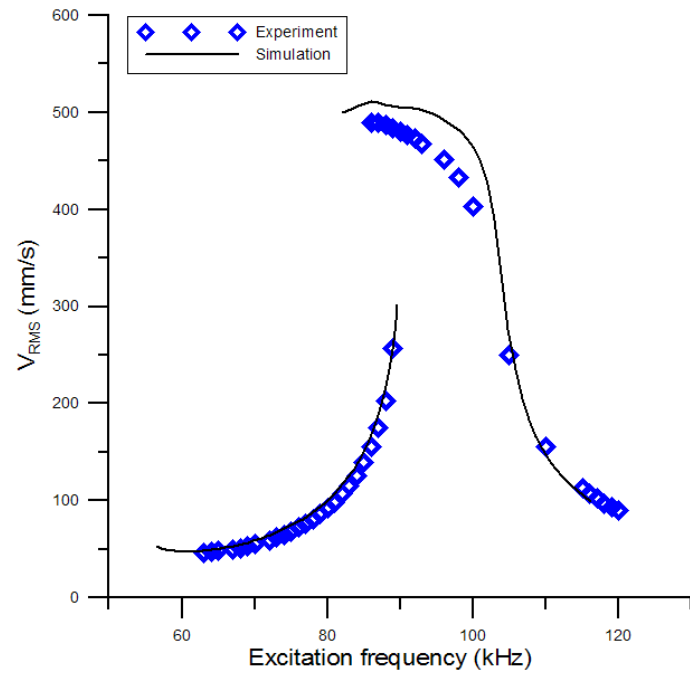
5.8) V.

The discrepancy between the experiment and simulation excitation levels is due to dielectric charging and divergence of the electrostatic field due to the doubly-curved configuration of the bridge under study, figure 5.8, from the parallel-plate assumptions. Dielectric charging, due to charge trapping in the silicon nitride insulation layer, increases the effective bias voltage across the bridge [70].

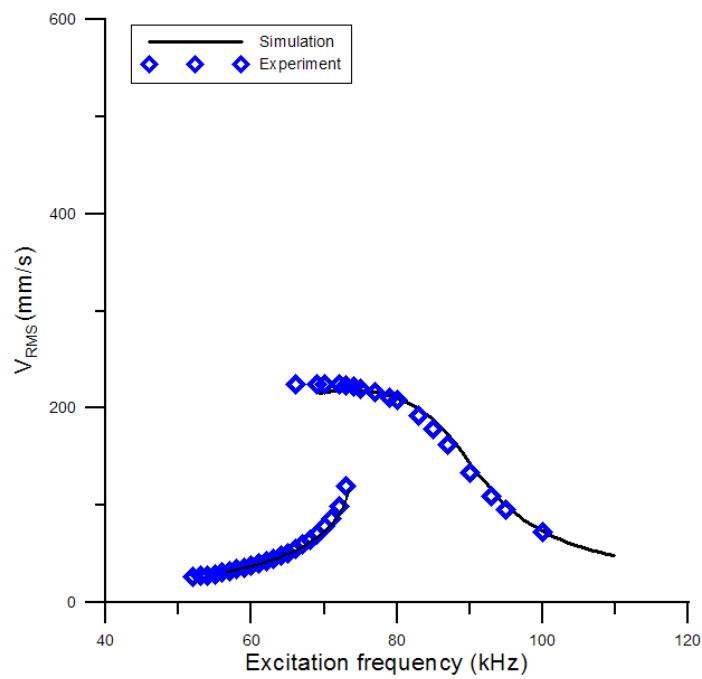
All the frequency-response curves shown in figure 5.11 are bent to the left indicating a softening nonlinearity. In each case, the dynamic pull-in occurred in backward sweeps beyond the peak point of the curve.

The velocity of beam oscillations is significantly larger under condition (1) than it is under condition (2) for the same excitation frequency. At low DC voltage, the stable equilibrium is away from the saddle which results in a larger basin of attraction, and thereby larger orbits and higher velocities, than those available at high DC voltage [69]. The phase portrait, which essentially maps the switch velocity versus its displacement depicts the basin of attraction. It is the set of initial conditions leading to long-time behavior that eventually approaches the attractor, which in this case is the switch pull-in. The orbits are essentially the map of switch velocity and its displacement in the phase portrait. The phase portraits of the switch are mapped and discussed in the following section. As a result, the orbits of beam oscillation have more room to grow with AC voltage under condition (1) than they do under condition (2) before touching the stable manifold of the saddle which precipitates pull-in.

Holding the bias voltage V_{DC} , and therefore the effective nonlinearity, constant while increasing the AC voltage V_{AC} , extends the softening frequency-response curves further to the left. Therefore, the peak of the frequency-response curve, the nonlinear resonance frequency λ , is a function of V_{AC} . Figure 5.12 shows the λ vs. V_{AC} curves at different bias voltages V_{DC} . The lowest λ in each curve indicates the last experimentally realizable amplitude in the frequency-response curve before dynamic pull-in interrupts the backward sweep.



(a)



(b)

Figure 5.11: The frequency-response curves of the midpoint RMS velocity for (a) low bias voltage and high AC voltage ($V_{DC} = 20$, $V_{AC} = 26.5$) V and (b) high bias voltage and low AC voltage ($V_{DC} = 50$, $V_{AC} = 6.5$) V.

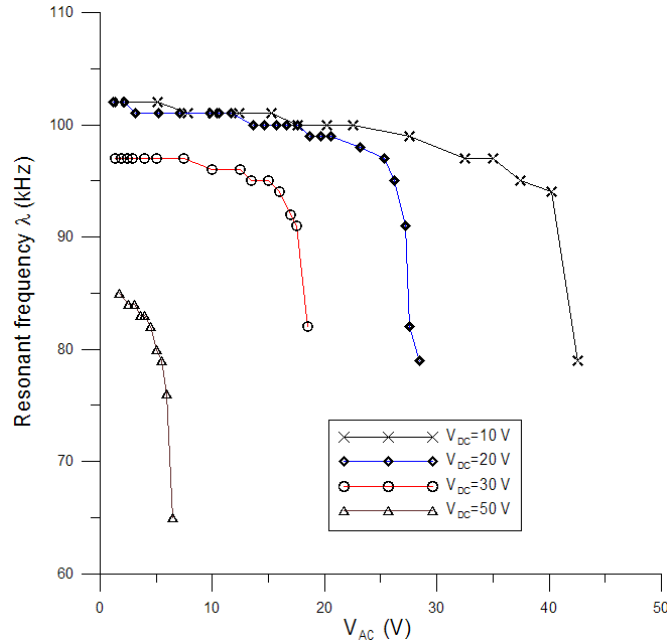


Figure 5.12: The nonlinear resonance frequency λ as a function of AC voltage V_{AC} at different bias voltages V_{DC} .

It can be seen from figure 5.12 that the AC voltage at which the backward sweep was interrupted is inversely proportional to the magnitude of the bias voltage V_{DC} . In fact, various combinations of V_{AC} and V_{DC} can be used to induce dynamic pull-in in a backward frequency sweep (procedure 2) and in a force-sweep (procedure 1). Figure 5.13 shows the combinations of V_{DC} and V_{AC} at the onset of dynamic pull-in under procedures 1 and 2. The figure shows that a smaller AC amplitude can induce dynamic pull-in at the nonlinear resonance frequency, procedure 2, than is required at the fundamental natural frequency, procedure 1.

A figure of merit FoM is defined to quantify the efficiency of various actuation methods used to induce pull-in compared to static actuation:

$$FoM = \frac{V_{SP} - V_{DP}}{V_{SP}} \% \quad (5.15)$$

where $V_{DP} = \sqrt{V_{DC}^2 + \frac{V_{AC}^2}{2}}$. Figure 5.14 compares the efficiency of dynamic actuation procedures 1 (circles) and 2 (triangles). The static pull-in of the switch under study is

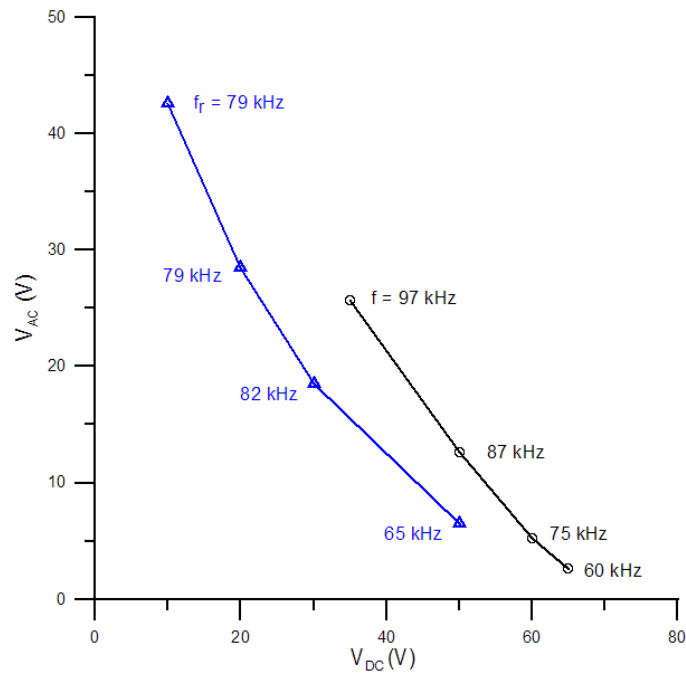


Figure 5.13: $V_{DC} - V_{AC}$ combinations required for dynamic pull-in for procedure 1 (circles) and procedure 2 (triangles)

$V_{SP} = 68.5$ V. Both procedures are superior to static actuation. This advantage increases as the bias voltage (V_{DC}) decreases opening more space for dynamic actuation procedures to take advantage of the dynamic amplification available at resonance. Further, procedure 2 outperforms procedure 1 for low bias voltages V_{DC} achieving 58.5% savings at $V_{DC} = 20$ V.

5.6 Dynamic Switching Methods

The phase portraits, depicting switch pull-in, were done in collaboration with Abdel-Rahman *et al.* at the University of Waterloo. In this section, two methods are proposed to realize dynamic actuation. These methods are designed to avoid the requirements imposed by the force sweep or frequency sweep dynamic switching methods discussed in section 5.5. Instead, the methods in this section use either a fixed excitation frequency or a single shift of the excitation frequency.

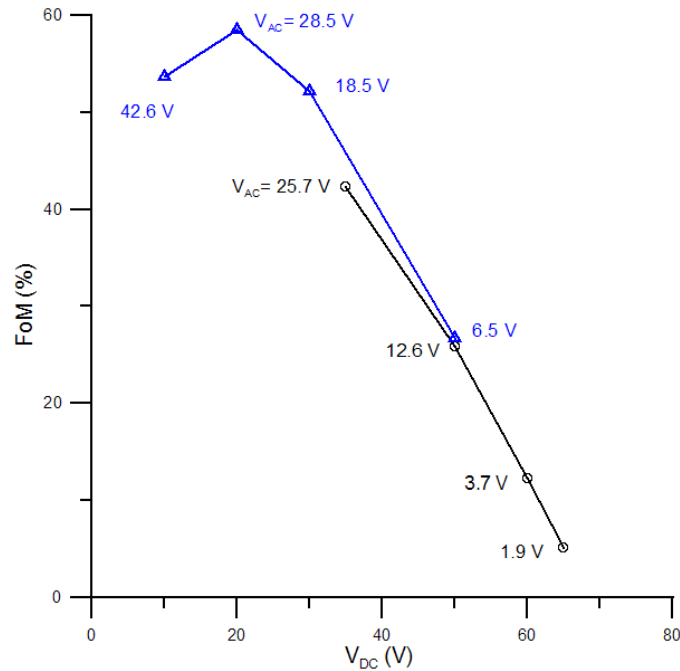


Figure 5.14: The figure of merit FoM representing the efficiency of dynamic actuation procedures 1 (circles) and 2 (triangles) compared to static actuation.

The switching time is a critical performance parameter for RF switches. The switching times of the fixed-frequency and shifted-frequency actuation methods are calculated in order to compare their performance. The switching time is defined as the time the bridge takes to move from an elevated steady-state position (ON-state) until the midpoint touches the transmission line (OFF-state). A shunt switch is normally ON; that is, the RF signal can be transmitted through the signal line when the bridge is unactuated. When the actuation waveform is applied, the beam closes the air gap and provides a low impedance path for the RF signal to be shunted to ground. This is considered the OFF-state of the switch.

In the fixed-frequency switching method, the bridge is excited with a fixed frequency starting from rest. In a narrow frequency range in the neighborhood of the resonance frequency, this method triggers touch-down. It was shown numerically that for a waveform defined by ($V_{DC} = 56$, $v_{ac} = 5.8$) V, switching can be achieved using this method in the frequency interval $A = [68.75, 75.97]$ kHz in figure 5.15. A simulated phase portrait of the bridge

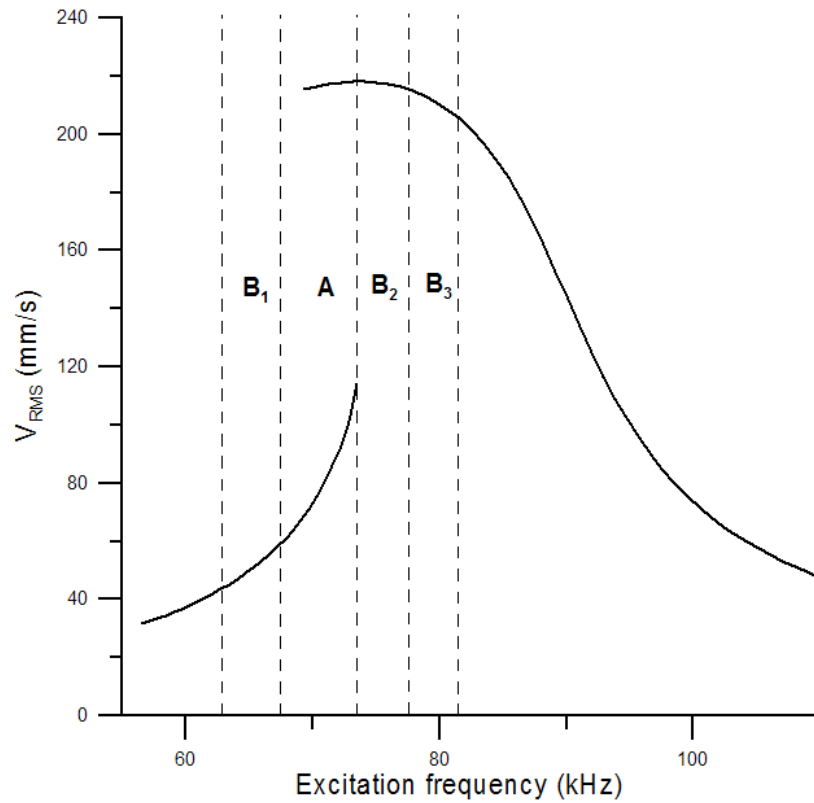


Figure 5.15: Frequency-response curve for ($V_{DC} = 56$, $V_{AC} = 5.8$) V, showing touch-down regions for different switching methods. The x-axis is separated into different regions for different switching methods based on the frequency values. A [68.75 - 75.97] KHz, B_1 [63.7 - 68.75] KHz, B_2 [76 - 79.7] KHz and B_3 [79.7 - 84.1] KHz.

response at an excitation frequency of $\Omega = 70.6$ kHz is shown in figure 5.16. The phase portrait is the plot of switch velocity versus its displacement.

Figure 5.16 shows in dashed lines the homoclinic orbit of the saddle in the absence of the forcing and damping. It represents the stable and unstable manifolds of the saddle intersecting non-transversally away from the saddle [71]. In the presence of forcing and damping, the homoclinic orbit is destroyed. Starting at rest, the midpoint describes larger orbits as the switch vibrates under the influence of the waveform. The orbit, then, follows the stable manifold to approach the saddle and is propelled to pull-in. The switching time in this case was calculated to be $62 \mu\text{s}$. This relatively large switching time is due to the high damping in the switch ($Q = 12.5$). Damping results in the bridge spending significant time as the response amplitude grows slowly over multiple excitation periods until it intersects the stable manifold of the saddle. The maximal switching times for this switching method, found at the edges of the frequency interval A , were calculated as $114 \mu\text{s}$ at $\Omega = 68.75$ kHz and $91 \mu\text{s}$ at $\Omega = 75.97$ kHz. This is comparatively larger than the pull-in time calculated under pure static actuation, $7.7 \mu\text{s}$ at the static pull-in voltage $V_{\text{DC}} = 68.5$ V.

The switching times throughout this subinterval (A) are too long for most RF applications. Switching time can be reduced by redesigning the switch to decrease the overall damping. One method to achieve this goal is to reduce the effect of squeeze-film damping (increasing Q), the dominant damping source, by reducing the bridge width or reducing the ambient pressure through hermetic encapsulation.

In the shifted-frequency switching method, an excitation signal is introduced at a frequency in the neighborhood of the natural frequency and held for a set period of time t_o . This signal is not intended to cause pull-in and the only requirements placed on the voltage waveform ($V_{\text{DC}}, v_{\text{ac}}$) are that

- the corresponding frequency-response curve exhibits multivaluedness
- the initial and shifted frequencies belong to an interval B of the frequency spectrum.

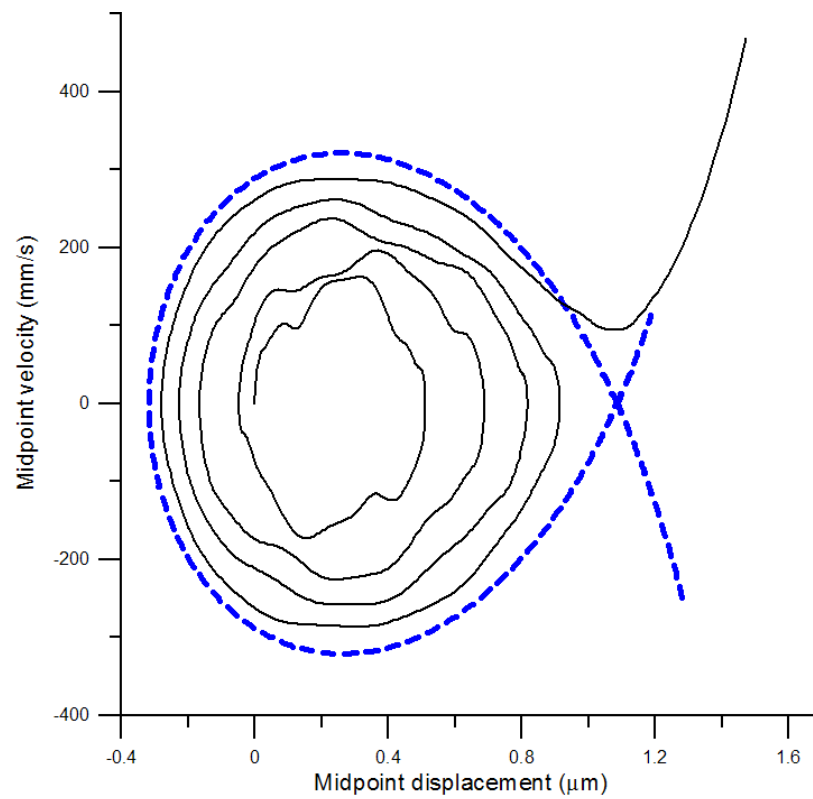


Figure 5.16: The simulated phase portrait of fixed-frequency switching for ($V_{\text{DC}} = 56$, $v_{\text{ac}} = 5.8$) V and $\Omega = 70.6$ kHz, for subinterval *A* in figure 5.15. The dashed lines depict the homoclinic orbit.

The frequency of excitation is then shifted by $\delta\Omega$.

To demonstrate this switching method, the same waveform is used for fixed-frequency switching ($V_{\text{DC}} = 56$, $v_{\text{ac}} = 5.8$) V, but with a frequency shift of $\delta\Omega = 0.1\Omega_{\circ}$. It was found numerically that the interval B can be subdivided into three subintervals B_1 , B_2 , and B_3 , figure 5.15, depending on the frequency shift direction. In the first subinterval, $B_1 = [63.7, 68.75]$ kHz, the only available stable responses lie on the lower branch of the frequency-response curve. An excitation frequency shift from $\Omega_{\circ} \in B_1$ to $\Omega_{\circ} + \delta\Omega$ triggers pull-in due to the fact that the frequency shift leads the system response to seek the larger stable orbits on the upper branch, thus approaching and intersecting the stable manifold of the saddle under the influence of the transient response. The phase portrait and time history for shifted-frequency switching starting from an initial excitation frequency $\Omega_{\circ} = 67.5$ kHz in the subinterval B_1 are shown in figure 5.17. The hold time was $t_{\circ} = 203 \mu\text{s}$ and the switching time was calculated to be $59 \mu\text{s}$. The phase portrait depicts the relation between switch midpoint displacement w and the midpoint velocity \dot{w} in mm/s; the velocity units are chosen in accordance with the experimental data.

In the second and third subintervals, $B_2 = [76, 79.7]$ kHz and $B_3 = [79.7, 84.1]$ kHz, the only available stable responses lie on the upper branch of the frequency-response curve. A shift-down from an initial excitation frequency in the subinterval B_3 , $\Omega_{\circ} \in B_3$, triggers pull-in as the response wanders around its initial large orbit and ends up intersecting the stable manifold of the saddle under the influence of this transient behavior. The phase portrait and time history for the shifted-frequency switching starting from an initial excitation frequency $\Omega_{\circ} = 83.2$ kHz in the subinterval B_3 are shown in figure 5.18. The hold time was $t_{\circ} = 203 \mu\text{s}$ and the switching time was calculated to be equal to $72 \mu\text{s}$.

It follows from figures 5.17 and 5.18 that a significant fraction of the switching time is consumed as the response orbit wanders prior to intersecting the stable manifold of the saddle. This process is strongly influenced by the switch damping as was the case for fixed-frequency switching. Therefore, the switching time of shifted-frequency switching can also

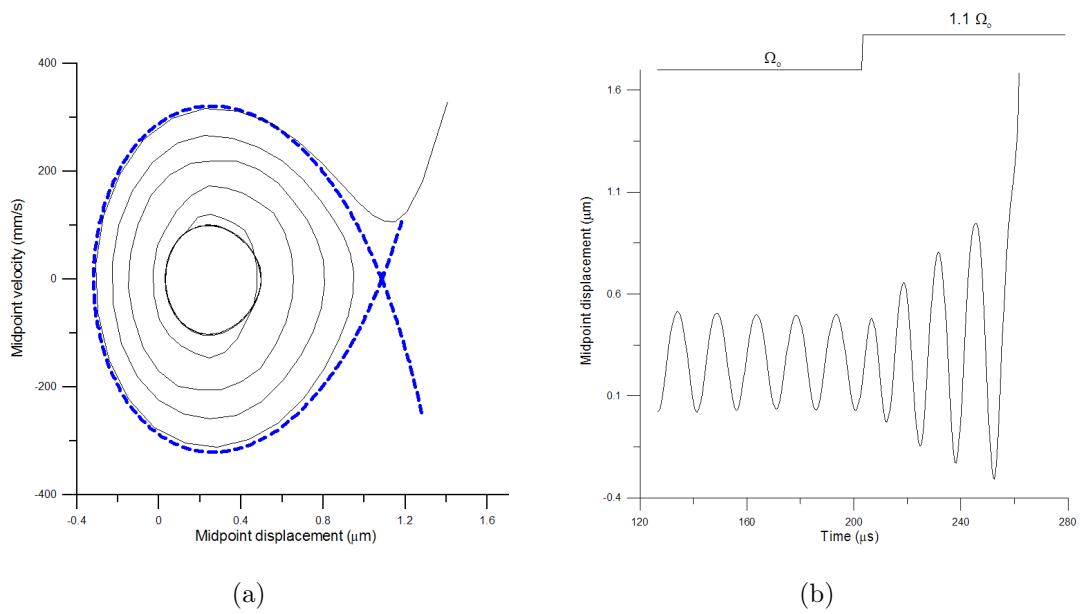


Figure 5.17: (a) The simulated phase portrait and (b) time history of shifted-frequency switching for the waveform ($V_{DC} = 56$, $V_{AC} = 5.8$) V starting from an initial excitation frequency $\Omega_o = 67.5$ kHz in the subinterval B_1 from figure 5.15.

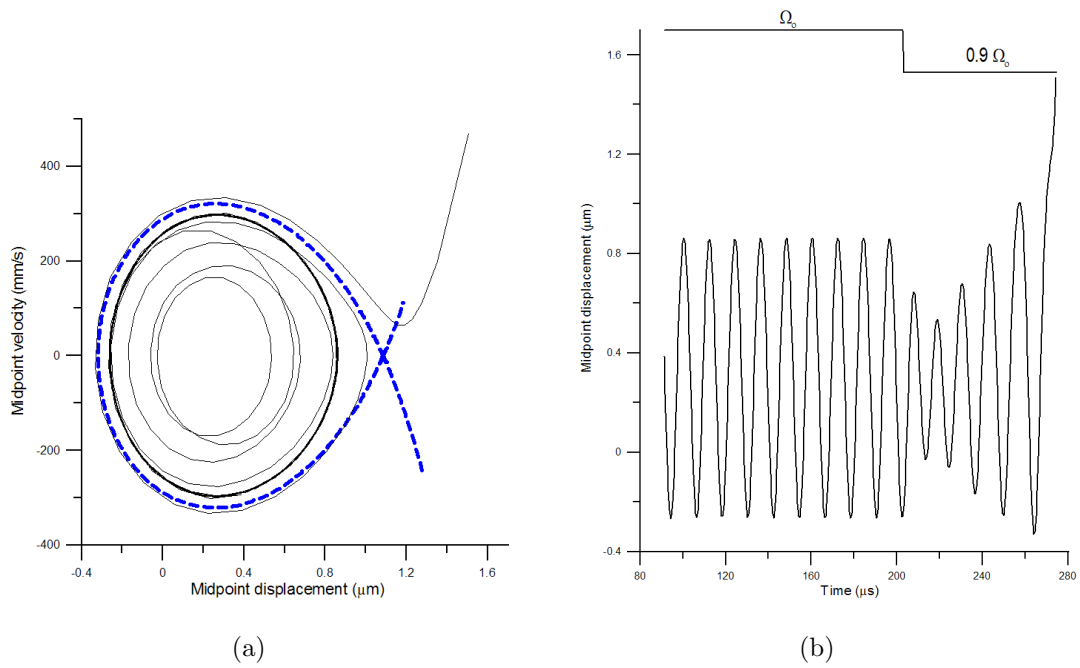


Figure 5.18: (a) The simulated phase portrait and (b) time history of shifted-frequency switching for a waveform of ($V_{DC} = 56$, $V_{AC} = 5.8$) V starting from an initial excitation frequency $\Omega_0 = 83.2$ kHz in subinterval B_3 from figure 5.15.

be reduced by reducing the damping.

For initial excitation frequencies in the subinterval B_2 , $\Omega_o \in B_2$, it was found that the frequency can be shifted up or down $\Omega_o \pm \delta\Omega$ to trigger pull-in. For example, using an initial excitation frequency $\Omega_o = 76.92$ kHz and a hold time of $t_o = 228$ μs , a switching time of 12.5 μs was realized as shown in figure 5.19. The switching time throughout this subinterval is the smallest compared to those obtained in the subintervals B_1 and B_3 and the interval A because the hold orbit in this case is the closest to the homoclinic orbit, which minimizes the time required for the transients to cause an intersection with the stable manifold of the saddle.

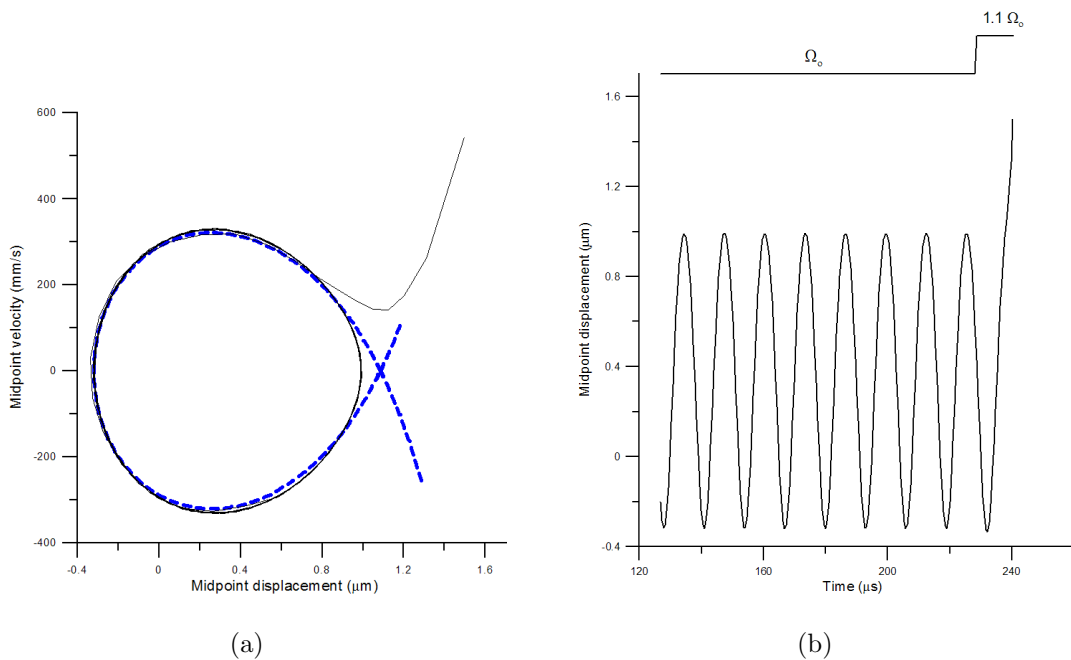


Figure 5.19: (a) Simulated phase portrait at $V_{DC} = 56$ V and $V_{AC} = 5.8$ V starting from an orbit at $\Omega = 76.92$ kHz and (b) time history with the frequency step function for subinterval B_2 from figure 5.15.

5.7 Summary

Shunt capacitive MEMS switches were electroplated gold bridges on CPW lines fabricated on silicon substrates. A reduced-order model was adopted to characterize the switch response. The model accounts for midplane stretching, electrostatic forcing due to non-overlapping parallel plates. A parameter identification routine was developed to estimate the switch parameters. The phenomenon of dynamic or resonant pull-in on these switches were investigated and modeled. The lower bound on static actuation, static pull-in voltage V_{SP} , was found to be 68.5 V. Dynamic actuation was investigated using force and frequency sweeps in the vicinity of the switch natural frequency. The voltage savings of dynamic actuation V_{DP} over static actuation were quantified using a Figure of Merit defined as

$$FoM = \frac{V_{SP} - V_{DP}}{V_{SP}}$$

Greater voltage savings were obtained using a frequency sweep, $FoM = 60\%$, than those obtained using a force sweep, $FoM = 40\%$. Dynamic switching using a force sweep requires increasing the voltage amplitude at a constant frequency until dynamic pull-in occurs. On the other hand, dynamic switching using a frequency sweep requires, in addition, a down-sweep past the nonlinear resonance frequency to trigger pull-in.

It is obvious that as the FoM increases, the switching time will also increase. To address this shortcoming a transient switching method is proposed to implement dynamic switching in order to obtain a shorter switching time of the same order as that obtained using static switching. Two switching methods are proposed to facilitate the use of the lower actuation voltage realized by the frequency-sweep technique. A fixed-frequency method simply sends a step waveform of the same order as those shown in figure 5.12 in the CPW at an excitation frequency within a narrow band around the cyclic-fold bifurcation. A shifted-frequency method maintains a waveform of the same order as those shown in figure 5.12 for a few excitation periods before shifting the excitation frequency up or down by a discrete

amount $\delta\Omega$. The fixed-frequency method is also simpler to implement. The shifted-frequency method requires an additional step while providing a wider actuation frequency band and the minimum realizable switching time for actuation frequencies within subinterval B_2 . The switching time obtained using dynamic actuation was always longer than that obtained using static actuation except for shifted-frequency switching when used in subinterval B_2 where the two switching times were comparable.

The next chapter will discuss non-linear responses of electrostatically actuated beams for both resonant switch and oscillator implications.

Chapter 6

Non-linear Response of Electrostatically Actuated Beam Resonators and Oscillator Phase Noise Implications

This chapter focuses on the study of non-linear responses of electrostatically actuated beams for both resonant switch and oscillator applications. While operating in an open-loop or resonant switch related application, a non-linear cancellation method is proposed to maximize the switch motion in the linear regime without multi-valuedness in the switch response. The resonator is modeled as a forced oscillator with quadratic and cubic spring non-linearities, and effect of bias voltage V_{DC} on the effective nonlinearity of the resonator is studied. Three domains of operation are identified in the resonator response: hardening-type, softening-type, and near-linear behaviors. The power handling of the resonator can be increased without the onset of frequency jumps (hysteresis) due to the non-linear spring.

An oscillator is a closed loop system where the resonator's response (phase) is fed back

via an amplifier. To increase the value of linear Q , operation in the non-linear regime is proposed. It has been shown that the multi-valuedness that limits the response of open loop systems no longer exists since frequency is always a single-valued function of the phase [72], [73]. However, the above references do not discuss the best case phase noise performance for such phase feedback systems, nor the theory behind the optimum operating points for better phase noise performance. In this work, the non-linear response is theoretically analyzed and the best case operating point (amplitude, phase and forcing) is determined for minimal phase noise response of the oscillator. The non-linear mixing of low frequency $1/f$ is investigated. This mixing causes phase distortion of the output signal and is quantified by the phase noise. It is shown that the optimal operating point of the resonators phase minimizes this distortion. The phase (of the resonator) can be established by controlling the rest of the phase around the loop since the total phase for self sustained oscillations around the loop is zero or 2π . It has been shown that setting the resonators phase automatically sets its corresponding amplitude and frequency [72], [73].

A set of two first-order nonlinear ordinary-differential equations that describe the modulation of amplitude and phase of the (displacement) response is presented. These are referred to as *modulation equations*. The amplitude and phase responses of the resonators displacement are coupled to each other through forcing, damping and the effective non-linearity co-efficient (S). For a sinusoidal forcing function at a frequency close to the resonant frequency of the resonator, the solution of resonator displacement is a set of the fixed points (constant values of amplitude and phase) defined by the modulation equations.

6.1 Background

Figure 6.1 illustrates the implementation of a reference oscillator which is comprised of a MEMS resonator with a feedback amplifier. Integration of these micromechanical structures with on-chip integrated circuitry potentially leads to considerable size and cost reduction,

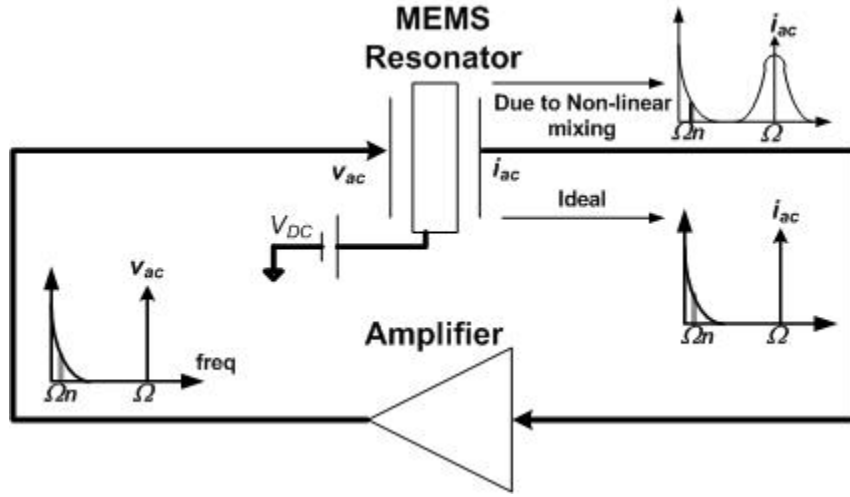


Figure 6.1: Implementation of MEMS based reference oscillator. The amplifier output presents a significant amount of low-frequency ($\Delta\Omega$) $1/f$ noise at the input of the resonator

making them commercially attractive. Figure 6.1 also illustrates the up conversion of low frequency ($1/f$) noise into signal sidebands that results in close in phase noise of the signal that is qualitatively illustrated in figure 6.2

The phase-analysis of the time-varying displacement gives an insight into how the nonlinearities in the resonator influence the phase noise performance of the output current. Perturbations in the period of a periodic signal will move the zero crossing point from its ideal position along the time axis, figure 6.2, leading to phase noise in the signal that can be represented by the 2^{nd} term on the right hand side of equation 6.1 (assuming the steady state phase $\gamma_{dc} = 0$)

$$A \cos(\Omega t + \gamma_n(t)) \approx A \cos(\Omega t) - A \gamma_n(t) \sin(\Omega t), \quad (6.1)$$

or as amplitude noise by setting $A = a_{dc} + a_n(t)$ and expanding the 1^{st} term on the right hand side of equation 6.1 as shown below [74]:

$$A \cos(\Omega t) = a_{dc} \cos(\Omega t) + a_n(t) \cos(\Omega t), \quad (6.2)$$

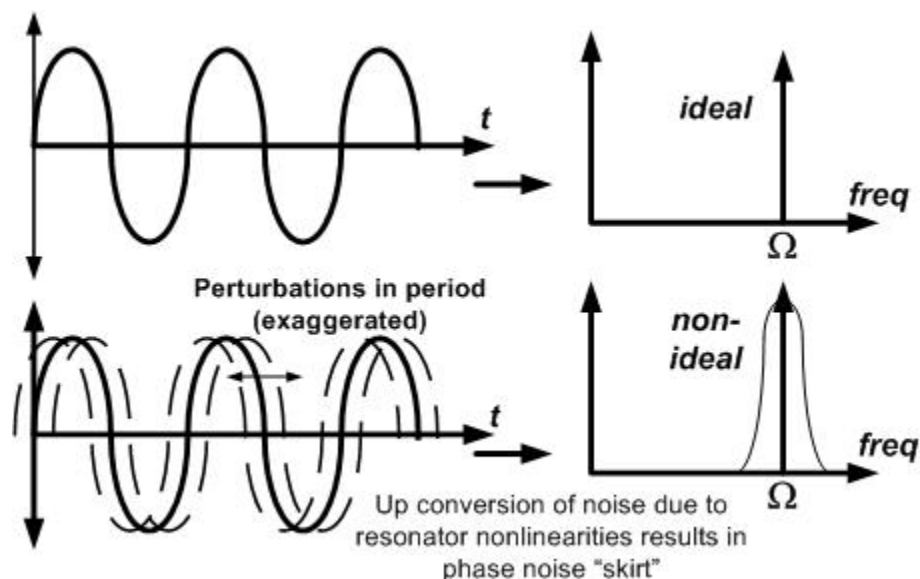


Figure 6.2: Illustration of an ideal vs. non-ideal spectrum [74].

where $|a_n(t)|$ and $|\gamma_n(t)|$ are very very small terms representing random variations in the period or the amplitude of the signal. The function $\gamma_n(t)$ is the phase noise. The spectrum of $\gamma_n(t)$ or $a_n(t)$ is translated to $\pm \Omega$. The effects of phase and amplitude noise are qualitatively the same. The symmetric sidebands would be replaced with a symmetric “skirt” in the frequency domain around Ω as illustrated in figure 6.2. The slope of the skirt, in dBc/Hz at a certain offset from the center frequency Ω , is the standard form in which *phase noise* is characterized in RF applications.

In MEMS resonators, it has long been claimed that maximum vibration amplitude and therefore the power handling capacity is limited by cubic and quadratic nonlinearities [75]. However, this is only valid when the resonator operates in open-loop. When operating as a closed loop phase feedback system, stable oscillations without multivalued responses with increased forcing has been demonstrated experimentally [72]. However, prior work in the literature does not theoretically analyze the phase response of the non-linear system in determining the optimum operating points for better phase noise performance of the system. Section 6.3 analyzes the frequency and phase responses of the resonator to determine the optimum phase/frequency, where the perturbations to frequency due to the perturbations in

phase (phase noise) is zero. These operating points should result in a better close in phase noise of the oscillator.

The influence of V_{DC} on the effective non-linearities of the system is also investigated in section 6.4. It is shown that there is a certain V_{DC} that sets the effective non-linearity, S , to zero by canceling the positive non-linearity (due to mid-plane stretching) with the negative non-linearity proportional to the electrostatic spring force. This method of cancellation increases the output amplitude and would prove effective in an open loop environment such as the operation of a resonant switch. However, in order to operate at a reasonable value of V_{DC} , it is typically required to have a larger positive non-linearity, which is proportional to the resonator gap (d) in fixed-fixed beam resonators. Also, decreasing d is essential for decreasing the motional resistance of resonators. Henceforth, this non-linearity cancellation approach will not be very useful for very narrow gap resonator based oscillators.

Meanwhile, it has been shown that $(1/f)$ noise up-conversion to carrier sidebands in very narrow gap electrostatic resonators is due to the parametric type mixing caused by the linear term, and not the quadratic or cubic terms [39]. The next section briefly describes the resonator model as adapted from [76] and presents the solution of the resonator's response that is used for frequency response analysis in the rest of the chapter. Section 6.5 briefly describes parametric forcing due to capacitive force non-linearity [39]. However, this section does not model the resonator's response as parametric forcing, but rather focuses on the selection of operating points in determining the best case phase noise performance. It is shown that, for the best case phase noise performance, the power handling must be maximized while minimizing the noise up-conversion due to parametric type mixing. Section 6.6 estimates the worst case noise mixing using [39] and derives an expression for phase noise when the resonator operates at the critical points where the perturbation to frequency is theoretically zero due to the perturbations of phase.

6.2 Clamped-Clamped Microbeam Resonator Model

Consider the clamped-clamped microbeam shown in figure 5.1 of chapter 5. The resonator is electrostatically actuated by the electrode under the micro bridge subject to a potential difference $v(t) = V_{DC} + v_{ac} \cos \Omega t$ where the excitation frequency $\Omega \approx \omega$, the natural frequency of the microbeam is defined by its first mode of resonance in the transverse direction. The non-dimensional equation of motion governing the transverse deflection of the microbeam $w(x, t)$ (adapted from [76], [77]) which is shown below, has already been presented in chapter 5, but is repeated here for reference.

$$\frac{\partial^2 w}{\partial t^2} + c \frac{\partial w}{\partial t} + \frac{\partial^4 w}{\partial x^4} = \left[N + \alpha_1 \int_0^l \left(\frac{\partial w}{\partial x} \right)^2 dx \right] \frac{\partial^2 w}{\partial x^2} + \frac{1}{2} \frac{\alpha_2 v(t)^2}{(1-w)^2} \quad (6.3)$$

where x is the position along the plate length l . The deflection of the beam is nondimensionalized with respect to the distance between the beam and the actuation electrode d , the position along the beam axis x is nondimensionalized with respect to the beam length l , c and N are nondimensionalized damping and axial tensile force respectively and the time t is nondimensionalized with respect to a characteristic time-scale $T = \left(\frac{\rho A l^4}{EI} \right)^{0.5}$, where $A = bh$ and $I = \frac{bh^3}{12}$ are the area and second moment of inertia of the beam cross-section, and b and h are the microbeam's breadth and thickness, respectively. $v(t)$ is the forcing function.

The other non-dimensional parameters appearing in equation 6.3 are shown below [76]:

$$\alpha_1 = 6 \left(\frac{d}{h} \right)^2, \quad (6.4)$$

$$\alpha_2 = \frac{6\epsilon l^4}{E h^3 d^3}.$$

where α_1 and α_2 are the scaling factors for geometric and electrostatic nonlinearities defined in equation 6.3. The geometric nonlinearity G, due to mid-plane stretching is defined by first term on the right hand side as $\left[\int_0^L \left(\frac{\partial w}{\partial x} \right)^2 dx \right] \frac{\partial^2 w}{\partial x^2}$. The electrostatic nonlinearity E, due

to capacitive transduction is defined by second term as $\frac{1}{2} \frac{v(t)^2}{(1-w)^2}$.

In the presence of damping, and operating away from internal resonances, the dynamic response can be approximated by a one-mode shape $\phi(x)$ Galerkin expansion. Further, a consistent first-order approximation (omitting the Higher Order Terms, H.O.T.) of the beam's response [76] can be obtained using the method of multiple scales [78] [41], as shown below

$$w(x, t) = w_s(x) + a \cos(\Omega t - \gamma)\phi(x) + H.O.T. \quad (6.5)$$

where $w_s(x)$ is the static deflection due to V_{DC} . The modulation of the amplitude a and phase γ is governed by two nonlinear differential equations [76] as shown below:

$$\begin{aligned} \dot{a} &= -\mu a + \frac{F}{\omega_o} \sin \gamma \\ \dot{\gamma} &= \sigma - \frac{S a^2}{\omega_o} + \frac{F}{a \omega_o} \cos \gamma, \end{aligned} \quad (6.6)$$

where

$$\Omega = \omega_o + \epsilon^2 \sigma \quad (6.7)$$

ϵ is a book-keeping parameter (implying that the detuning σ between the excitation frequency Ω and the natural frequency of the resonator ω is two orders of magnitude smaller than those frequencies), S is the effective nonlinearity coefficient of the system, μ is the modal damping coefficient, and F is the amplitude of excitation given by

$$F = \int \frac{\alpha_2}{(1 - w_s)^2} V_{DC} v_{ac} \phi(x) dx. \quad (6.8)$$

The effective nonlinearity coefficient is the sum of four nonlinearities [76]:

$$S = S_q^G + S_c^G + S_q^E + S_c^E. \quad (6.9)$$

arising from the quadratic ($_q$), cubic ($_c$), geometric ($_G$), and electrical ($_E$) nonlinearities. Table 6.1 summarizes the dependence of the nonlinear coefficients on the resonator voltage and dimensions. Note that the cubic geometric nonlinearity S_c^G is the only nonlinearity that depends on the geometry of the resonator and not on the bias voltage V_{DC} .

Property	Voltage Dependence	Dimensional Dependence
Cubic, Geometric	-	$\alpha_1(\propto (\frac{d}{h})^2)$
Quadratic, Geometric	V_{DC}^2	$\alpha_1(\propto (\frac{d}{h})^2)$
Cubic, Electrical	V_{DC}^2	$\alpha_2(\propto (\frac{l^4}{h^3 d^3}))$
Quadratic, Geometrical	V_{DC}^2	$\alpha_2(\propto (\frac{l^4}{h^3 d^3}))$

Table 6.1: Dependence of the nonlinearities on V_{DC} and resonator dimensions.

6.3 Steady State Solution of the Displacement Response

The periodic solutions of equation 6.3 correspond to conditions of constant a and γ ; that is the fixed points (a_{dc}, γ_{dc}) of the modulation equations 6.6. Using this solution, some properties of the steady state solution are derived in this section. Thus, letting $\dot{a} = \dot{\gamma} = 0$ in equation 6.6 and simplifying, the *Amplitude-Frequency* (adding and squaring the modulation equations) and the *Phase-Frequency* (dividing the amplitude equation by the phase equation) responses of the system, respectively, are obtained as shown below:

$$a_{dc}^2 \left[\mu^2 + \left(\sigma - \frac{S a_{dc}^2}{\omega} \right)^2 \right] = \frac{F^2}{\omega^2} \quad (6.10)$$

$$\cot \gamma_{dc} = \frac{(S a_{dc}^2 - \sigma)}{\mu}. \quad (6.11)$$

Equation 6.10 and 6.11 are implicit equations for amplitude a and phase γ of the periodic response as a function of the detuning parameter σ (which is a representation of the excitation frequency, Ω). Solving equation 6.10 for σ , we obtain

$$\sigma = \pm \frac{1}{a_{dc}} \left[\frac{F^2}{\omega^2} - \mu^2 a_{dc}^2 \right]^{1/2} + \frac{S a_{dc}^2}{\omega}. \quad (6.12)$$

Now, recalling that $\sigma = \Omega - \epsilon^2 \omega_o$, setting $\epsilon = 1$, and noting that the amplitude a_{dc} is maximum when the expression inside the square root vanishes, we obtain the following equation for the nonlinear resonance frequency.

$$\Omega_r = \omega_o + \frac{S F^2}{\omega^3 \mu^2}. \quad (6.13)$$

This equation relates the nonlinear resonance frequency Ω_r and the linear resonant frequency ($\Omega_r = \omega_o$, when $S = 0$) via the effective nonlinearity S of the system, the amplitude F of AC forcing, and the damping in the system. The above equation, re-written below in equation 6.14, shows that the amplitude-frequency ($A-f$) relationship has a parabolic dependence for high-Q resonators, similar to Quartz resonators. The equation shows the shift in frequency is proportional the non-linearity coefficient S .

$$\frac{\Omega_r - \omega}{\omega} = \frac{\Delta\omega}{\omega} = \left(\frac{S}{\omega^2} \right) a_{dc}^2. \quad (6.14)$$

6.3.1 Resonance curve: Points of Zero Slope

Another useful relation follows from taking the derivative of equation 6.11 with respect to σ as shown below

$$\frac{\partial \gamma_{dc}}{\partial \sigma} = - \frac{\mu(1 - 2S a_{dc} \frac{\partial a_{dc}}{\partial \sigma})}{\mu^2 + (\sigma - S a_{dc}^2 / \omega)^2}. \quad (6.15)$$

which shows the variation of phase with respect to the frequency and vice versa. Expressions for the phase and the amplitude at special points along the resonance curve are derived next. First consider the peak of the resonance. At this point, with the drive amplitude or forcing held fixed,

$$\frac{\partial a_{dc}}{\partial \sigma} = 0. \quad (6.16)$$

The derivative of equation 6.10 with respect to σ yields

$$\frac{\partial a_{dc}}{\partial \sigma} = \frac{2\omega^2 a_{dc}^2 (S a_{dc}^2 / \omega - \sigma)}{2a_{dc}\omega^2(\mu^2 + \sigma^2) + 2S a_{dc}^3(3S a_{dc}^2 - 4\sigma\omega)} \quad (6.17)$$

which, with equation 6.16, implies that at the peak of the resonance is:

$$\sigma - \frac{S a_{dc}^2}{\omega} = 0. \quad (6.18)$$

Substituting this equation into the $\dot{\gamma}$ modulation equation 6.6 yields $\cos\gamma_{dc} = 0$. From this and equation 6.6 it also follows that the relationship between the amplitude a_{dc} and the drive F is

$$a_{dc} = \frac{F}{\mu\omega} \quad (6.19)$$

and that the phase angle γ_{dc} is

$$\gamma_{dc} = -\pi/2. \quad (6.20)$$

Substituting equations 6.16 - 6.18 into equation 6.15 one also obtains

$$\left| \frac{\partial \gamma_{dc}}{\partial \sigma} \right| = 1/\mu = 1/2c = Q/2\omega \quad (6.21)$$

where we define $\mu = 2c$, and ω is the resonant frequency at the peak of the curve which corresponds to the phase angle of $\pi/2$. The above equation also implies that small changes in frequency due to the perturbations of phase ($\partial\sigma/\partial\gamma \approx 1/Q$) are minimal when the system has minimal damping or high Q . Re-arranging the above equation we arrive at the definition of Q given by

$$Q = \frac{\omega}{2} \frac{\partial\gamma_{dc}}{\partial\sigma} \quad (6.22)$$

Equation 6.22 is the definition of “open-loop” Q . For steady state oscillations in a feedback loop or a self-excited oscillator, the total phase shift around the loop must be zero or 2π . Suppose the oscillator frequency deviates from ω and the phase slope ($\partial\gamma/\partial\sigma$) is large, a significant change in the phase shift arises, thus violating the condition of oscillation and forcing the frequency to return to ω . Note that equations 6.18 through 6.21 hold even in the linear case when $S = 0$. This also suggests that behavior at resonance of a non-linear resonator is similar to that of a linear resonator.

6.3.2 Resonance Curve: Points of Infinite Slope

Now consider points on the resonance curve having infinite slope, that is, points at which

$$\frac{\partial\sigma}{\partial a_{dc}} = 0. \quad (6.23)$$

Note that, also according to equation 6.15, at these points:

$$\frac{\partial\sigma}{\partial\gamma_{dc}} = 0, \quad (6.24)$$

that is, the phase is a function of frequency and has infinite slope at the same frequency at which the resonance curve also has infinite slope. These points of infinite slope occur when (from equation 6.17)

$$2a\omega^2(\mu^2 + \sigma^2) + 2Sa_{dc}^3(3Sa_{dc}^2 - 4\sigma\omega) = 0. \quad (6.25)$$

One operating point is of particular interest. This is the critical point where, in addition to satisfying equation 6.23, one has

$$\frac{\partial^2 \sigma}{\partial a_{dc}^2} = 0, \quad (6.26)$$

which is essentially the point of inflection (a point of infinite slope). Taking the reciprocal of both sides of equation 6.17, differentiating with respect to a_{dc} , and using equations 6.23, 6.25 and 6.26, the following is obtained:

$$a_{dc,Crit}^2 = \frac{2}{3} \frac{\sigma\omega}{S} \quad (6.27)$$

Substituting equation 6.27 into equation 6.25, one obtains the critical detuning frequency:

$$\sigma_{Crit} = \sqrt{3}\mu. \quad (6.28)$$

Combining this result with equation 6.27 yields the critical point amplitude

$$a_{dc,Crit}^2 = \frac{2\sqrt{3}}{3} \frac{\mu\omega}{S}. \quad (6.29)$$

Equations 6.10, 6.28 and 6.29 then lead to the expression for the critical point drive (or amplitude of forcing):

$$F_{Crit}^2 = \frac{8\sqrt{3}}{9} \frac{\mu^3\omega^3}{S}. \quad (6.30)$$

Substituting equations 6.28 - 6.30 into equations 6.6, we find that the critical phase is given by

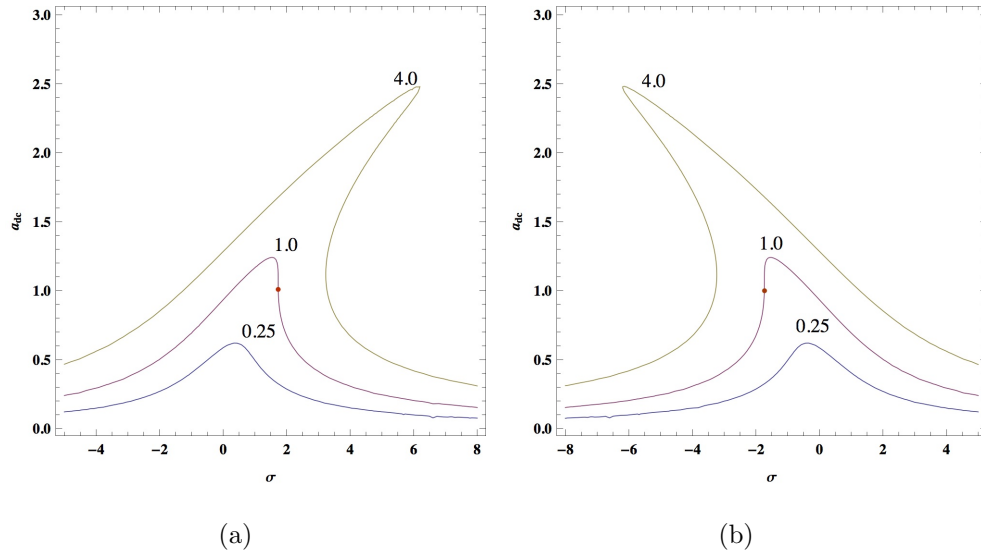


Figure 6.3: Sequence of amplitude-frequency resonance curves for which $S = \pm 1$ (figures 6.3(a) and 6.3(b) respectively) and $\mu = \omega = 1$. The central curve (1.0) in both the figures corresponds to the critical drive. Curves labeled 0.25 and 4, the drives are one quarter of or four times the critical drives respectively. At the critical drive the resonance curves exhibits a point of infinite slope (point of inflection), called the critical point. This is indicated by a red dot on both the figures. For larger drives the amplitude curves are multi-valued functions of the detuning frequency σ and they also have two points of infinite slopes.

$$\gamma_{dc,Crit} = -\frac{2\pi}{3}. \quad (6.31)$$

Figures 6.3 and 6.4 display a set of resonance curves (both amplitude and phase) for both positive and negative non-linearities. The plots were generated using modulation equations 6.6 and parameters $S = \pm 1$, $\mu = 1$ and $\omega = 1$. In figures 6.3 and 6.4, the curve labeled 1.0 is for the critical drive $F_{Crit}^2 = 8\sqrt{3}/9$ (equation 6.30). The curves labeled 0.25 and 4 correspond to one quarter and four times the critical drive respectively. Frequency pulling of the resonance curves due to the nonlinearity is evident in all three curves. The critical point on the critical drive curve is indicated by a red dot in the resonance curves. At smaller drives

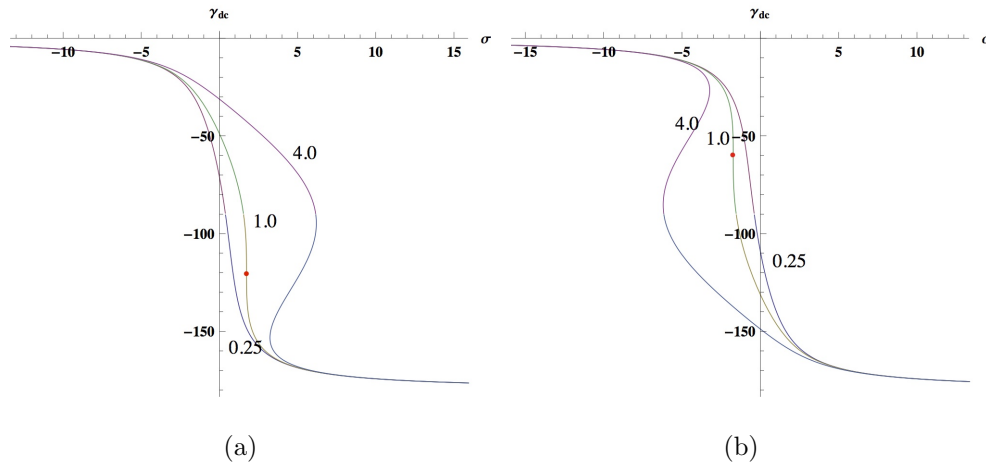


Figure 6.4: Sequence of phase-frequency resonance curves corresponding to the resonance curves of figure 6.3. The central curve (1.0) in both the figures corresponds to the critical drive. At the critical drive the phase also exhibits a point of infinite slope which occurs at the same value of the detuning frequency σ as the amplitude-resonance curve. This is indicated by a red dot on both the figures. For larger drives the phase becomes a multivalued function of the detuning frequency σ . Note, however, that σ , when viewed as a function of the phase, remains single valued.

the resonance curves are single valued. The last of the single valued curves is marked 1.0 and exhibits infinite slope at the critical point $(a_{dc,Crit}, \gamma_{dc,Crit})$. At larger drives ($\geq F_{Crit}^2$) the resonance curves are multivalued as a function of frequency and exhibit two points of infinite slope as shown in the figures 6.3 and 6.4. The importance of infinite slope points will be discussed in section 6.6.

Material Properties of Poly-Si Beam	15 MHz Resonator
Density ρ	2300 kg/m^3
Si Young's Modulus	150 GPa
Quality factor, Q	6800
Device Dimensions	
Electrode Length (l)	40 μm
Electrode breadth (b)	10 μm
Gap (d)	300 nm
Electrode Thickness (h)	2 μm
Electrode Area	40 x 10 μm^2

Table 6.2: Physical dimensions and material constants.

6.4 Non-linear Cancellation of Electrostatically actuated Resonators

This section discusses the influence of V_{DC} on the non-linearity of the system. Table 6.2 summarizes the material properties and dimensions of the micro-resonator under study here [79]. An external micro-beam is chosen to explain the non-linearity cancellation as well as the effect of non-linearities on resonator phase noise since this resonator has a very narrow gap and high Q compared to the fabricated resonators. The electrode to resonator gap is around 1 μm and the Q is around 12.5.

Figure 6.5 is a plot of the effective nonlinearity coefficient S versus V_{DC} for the resonator under study ($\alpha_1 = 0.135$, $\alpha_2 = 0.00172$) [76]. The positive geometric nonlinearities dominate at low V_{DC} whereas the negative electrical nonlinearities grow and dominate at high V_{DC} . At $V_{DC} = 39.2$ V, referred to as $V_{DC, Lin}$, the effective nonlinearity vanishes ($S = 0$) and the hardening geometric nonlinearities cancel the softening electric nonlinearities. Since the

geometric nonlinearities are proportional to d^2 and electric nonlinearities are proportional to $1/d^3$, it is possible to shift $V_{DC, Lin}$ to a larger value by increasing the gap. However, this results in operating at a smaller transduction coefficient α_2 and hence a larger motional resistance R_x . As a consequence, the amplifier gain in the oscillator implementation, and thus v_{ac} , need to be large enough to compensate for higher losses.

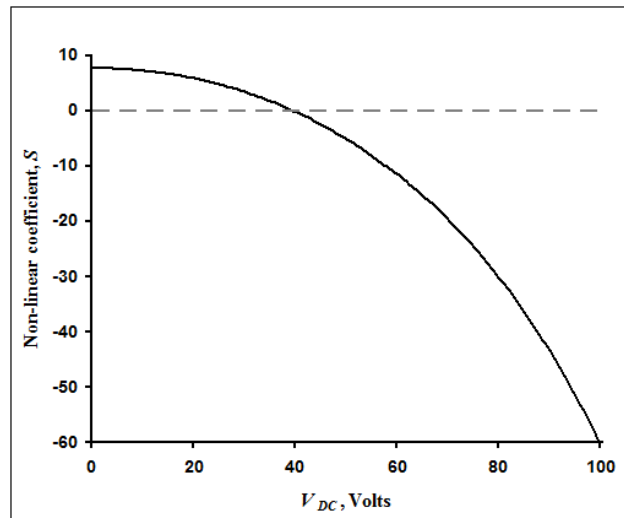


Figure 6.5: Nonlinearity coefficient S versus VDC.

Figure 6.6 is a plot of the maximum beam deflection w_{max} versus frequency in the hardening domain ($V_{DC} = 30$ V). At an AC excitation amplitude of $v_{ac} = 0.3$ V, the response is single valued. At an excitation amplitude of $v_{ac} = 1.0$ V, the resonator develops a region of multi-valuedness in the frequency interval [15.346, 15.354] MHz. The displacements are higher in this narrow frequency interval (7.6 KHz) but multi-valued, and hence not useful. For a given frequency, the threshold between single-valued and multi-valued frequency-response curves occurs at $v_{ac} = 0.37$ V. The maximum attainable deflection before multi-valued responses appear, for the hardening case was found to be $w_{max, hrd} = 60$ nm. This limits the resonator power handling capacity to $V_{DC} \approx 30$ V.

Similarly, figure 6.7 plots the amplitude response in the softening domain ($V_{DC} = 70$ V). When $v_{ac} = 0.5$ V multi-valued responses appear in the frequency interval [15.227, 15.332]

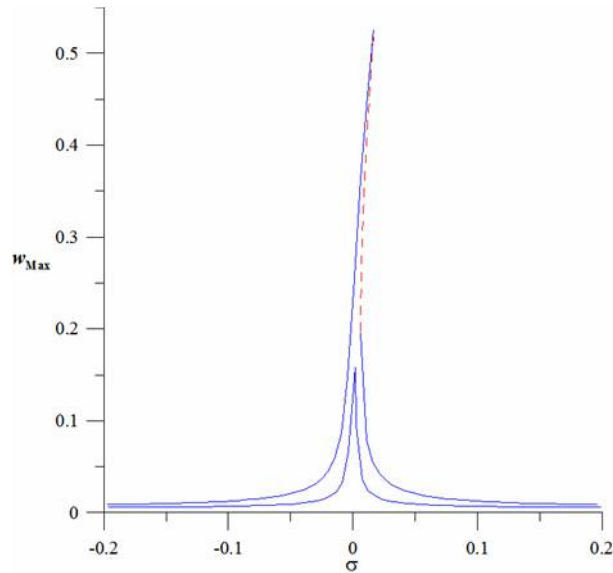


Figure 6.6: Frequency-response curves in the hardening domain. $V_{DC} = 30\text{V}$. $v_{ac} = 0.3\text{ V}$ for the lower curve and $v_{ac} = 1.0\text{ V}$ for the upper curve. w_{Max} is reported as a percentage of the capacitor gap d .

MHz resulting in hysteresis and rendering this frequency interval un-usable. The highest single-valued frequency-response curve in this case occurs at $v_{ac} = 0.061\text{ V}$. The maximum deflection attainable in this case, and thus the limiting value of realizable output current i_m was found to be at $w_{max,sft} = 30.6\text{ nm}$

Figure 6.8 shows a set of frequency response curves when the resonator is biased at $V_{DC,lin} = 39.2\text{ V}$. In this regime, the only instability limiting the amplitude of vibrations is dynamic pull-in [63]. The maximum attainable deflection $w_{max,lin}$ in the linear regime was found to be $w_{max,lin} = 180\text{ nm}$ when $v_{ac} = 1\text{ V}$, three times that which is realizable in the hardening domain at $V_{DC} = 30\text{V}$ and six times that which is realizable in the softening domain at $V_{DC} = 70\text{V}$. Hence, operating in the near-linear domain results in higher power handling capacity than operating in either the hardening or softening domains.

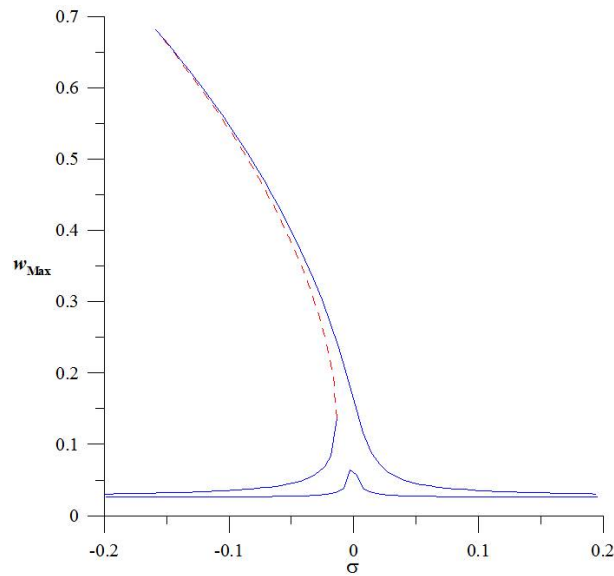


Figure 6.7: Frequency-response curves in the softening domain. $V_{DC} = 70\text{V}$. $v_{ac} = 0.05\text{ V}$ for the lower curve and $v_{ac} = 0.5\text{ V}$ for the upper curve. w_{Max} is reported as a percentage of the capacitor gap d .

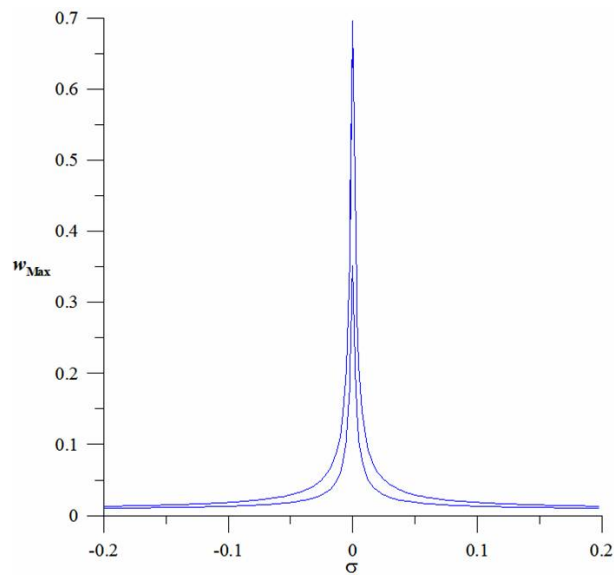


Figure 6.8: Frequency-response curves in the near-linear domain. $V_{DC} = 39.2\text{ V}$. $v_{ac} = 0.5\text{ V}$ for the lower curve and $v_{ac} = 1.0\text{ V}$ for the upper curve. w_{Max} is reported as a percentage of the capacitor gap d .

6.5 Phase Noise Analysis

In this section, the output current is calculated at $\Omega \pm \Omega_n$ sidebands. The current is then multiplied by the equivalent impedance $Z(\Omega \pm \Omega_n)$ at the offset frequencies to compute the output noise voltage. The output phase noise can be determined from the power ratio of the signal strength at the side bands ($\Omega \pm \Omega_n$) to the strength at Ω (discussed in the next section). Two major mechanisms of noise mixing are investigated. First, mixing due to capacitive current non-linearity is discussed, followed by mixing due to capacitive force non-linearity.

The output noise current can be calculated as follows:

$$i_n(\Omega \pm \Omega_n) = \frac{\partial(C(x)(V_{\text{DC}} + v_{\text{ac}} + v_n))}{\partial t} \approx V_{\text{DC}} \frac{\partial C(x)}{\partial t} \dot{x} + v_n \frac{\partial C(x)}{\partial x} \dot{x} + \dots \quad (6.32)$$

The first term in the above equation represents current at the excitation frequency Ω . The second term is responsible for the noise up conversion and results in noise current at $(\Omega + \Omega_n)$. The displacement response x is only at Ω and has no sidebands at $\Omega \pm \Omega_n$ since $\gamma_n = 0$ due to S being zero. Using 2.15 and 2.21, the up-converted noise current due to capacitive mixing can be written as:

$$i_n^{\text{cap}} = 2X_{\text{cap}}v_{\text{ac}}v_n \quad (6.33)$$

where the current aliasing factor due to capacitive non-linear mixing is defined as:

$$X_{\text{cap}} = \frac{Q\omega\eta^2}{2kV_{\text{DC}}}. \quad (6.34)$$

The current i_n^{cap} given by equation 6.33 has equal amplitudes at frequencies $\Omega \pm \Omega_n$.

The second main up-conversion mechanism is due to the square law: low frequency noise voltage v_n at Ω_n is mixed with signal voltage v_{ac} at Ω . The forcing, F_n at $\Omega \pm \Omega_n$ is given

by [39] includes the non-linear expansion of the capacitance and the square force law:

$$F_n = \frac{(V_{\text{DC}} + v_{\text{ac}} + v_n)^2 C}{2} \frac{C}{d} \left(1 + 2\frac{x}{d}\right). \quad (6.35)$$

The products $v_{\text{ac}} \times v_n$ and $x \times v_n$ result in the up-converted noise at $\Omega \pm \Omega_n$. Thus the force at the sidebands is:

$$F_n(\Omega \pm \Omega_n) \approx \frac{C}{d} v_{\text{ac}} v_n + 2\frac{C}{d} \frac{x}{d} V_{\text{DC}} v_n. \quad (6.36)$$

The displacement from this force is given by equation 2.16

$$x_n^F \approx -jQ \frac{F_n}{k}, \quad (6.37)$$

and the resulting noise current is:

$$i_n^F = \eta \dot{x}_n = -j\eta\omega x_n. \quad (6.38)$$

Substituting 6.36 and 6.37 in 6.38 and using equation 2.15 and 2.16 yields:

$$i_n^F = 2X_F v_{\text{ac}} v_n \quad (6.39)$$

where the X_F is the force aliasing factor given by:

$$X_F \approx \frac{Q\omega\eta^2}{2kV_{\text{DC}}} \left(1 - j2\frac{Q\eta V_{\text{DC}}}{kd}\right). \quad (6.40)$$

First term in the above equation is the same as the current aliasing factor, X_{cap} , in equation 6.34. The second term is due to xv_n , similar to parametric forcing. Substituting typical resonator parameters from Table 6.2 gives the value inside the brackets ($2\frac{Q\eta V_{\text{DC}}}{kd} \approx \dots$) as the

dominating term. The sum of both terms give the complete magnitude of aliasing factor, $X = X_{cap} + X_F$.

The value of force aliasing factor (X_F) is greater than the current aliasing factor (X_{cap}), showing that capacitor non-linearities dominate all other non-linearities. The non-linearity factor, S , does have an influence on the magnitude of the signal strengths. Instead of examining the influence of S on the aliasing factor, S should be used to determine if the resonator is linear, weakly-non-linear or strongly non-linear. The value is important to determine the region of operation of the resonator (defined by the fixed points of the system). If the resonator is near-linear or weakly non-linear (small S), the resonator phase should be set such that it operates at the peak frequency. This essentially is the point of zero slope or the peak of the frequency response curve ($\gamma_{dc} = \pm\pi/2$). Maximizing the v_{ac} value in the near-linear domain will improve the resonator phase noise performance, since the magnitude of output signal is maximized. When the system is non-linear like most electrostatic resonators, the resonator phase should be set such that, resonators frequency is around the point of infinite slope ($\gamma_{dc} = \pm 2\pi/3$) on the frequency response curves. This essentially means above the non-linear threshold, the dominant contributions to the phase noise are suppressed. To ensure the resonator maintains the specific phase conditions, the oscillator system should be implemented as a phase feedback system with a phase shifter/control (γ_{ctrl}) in the feedback loop that sets the resonator phase ($\gamma_{ctrl} = 2\pi - \gamma_{dc}$). In the next section, phase noise response of the output voltage is derived for the regions of zero and infinite slope defined by the effective non-linearity factor S .

6.6 Analytical Phase Noise Model

An analytical model for the noise in a closed loop resonator is now developed. The model is based on the well-known Leeson's equation [42], [74] and [39]. At resonance L_x cancels C_x and the amplifier cancels the resistive losses, R_x . Two sources of noise are included: thermal

noise $v_{n,t}$ and $1/f$ noise ($|v_{n,1/f}|^2 = |v_{n,t}|^2 \frac{\Omega_c}{\Omega_n}$), where Ω_n is the offset frequency from the center frequency Ω , and Ω_c is the corner frequency for the $1/f$ noise. The total input noise v_n of the resonator is $v_n = v_{n,t}(1 + \Omega_c/\Omega_n)$. The total output noise voltage can be found by multiplying the output noise current with the impedance of the resonator at $\Omega \pm \Omega_n$ and can be written as [42], [74]:

$$\frac{v_n^2}{\Delta f} = \frac{i_n^2}{\Delta f} |Z|^2 = 4kTR \frac{\Omega^2}{4\Omega_n^2} \frac{1}{\left(\frac{\Omega}{2}\right) \left(\frac{\partial \gamma}{\partial \sigma}\right)^2} = 4kTR \left(\frac{\Omega}{2Q\Omega_n}\right)^2. \quad (6.41)$$

where v_n and i_n are noise voltage and current respectively. It should be noted in the above equation that the definition of Q given in equation 6.22.

The noise at the output due to thermal noise can be written as

$$|v_{out}^{n,t}|^2 = |v_{n,t}|^2 \left[\frac{\Omega^2}{4\Omega_n^2} \frac{1}{\left(\frac{\Omega}{2}\right) \left(\frac{\partial \gamma}{\partial \sigma}\right)^2} + 1 \right] \quad (6.42)$$

This is single sideband noise. As the thermal noise in both side bands can be assumed uncorrelated, equation 6.42 is multiplied by two to obtain the double side-band noise and 1 is added to account for the noise floor.

The low frequency $1/f$ noise is up-converted in the resonator to noise current given by $i_{n,1/f} = 2Xv_{ac}v_{n,1/f}$, where $X = X_{cap} + X_F$ described in section 6.5. This up-converted noise is picked up by the amplifier and amplified (Gain = R_x) in the feed-back loop. The noise voltage at the output is given by

$$|v_{out}^{1/f}|^2 = X^2 R_x^2 |v_{ac}|^2 |v_{n,1/f}|^2 \left[\frac{\Omega^2}{4\Omega_n^2} \frac{1}{\left(\frac{\Omega}{2}\right) \left(\frac{\partial \gamma}{\partial \sigma}\right)^2} + 1 \right] \quad (6.43)$$

This is single sideband noise. As the noise on both side bands originate from the same $1/f$ source, they are correlated and the double side-band noise is obtained by multiplying 6.43 by 4. The total phase noise of the system is obtained by combining 6.42 and 6.43 and dividing

the result by two to account only for phase and not amplitude noise, and normalizing the result with signal v_{ac} we obtain:

$$S_\phi = \frac{|v_{n,t}|^2}{|v_{ac}|^2} \left(\frac{\Omega^2}{4\Omega_n^2} \frac{1}{\left(\frac{\Omega}{2}\right) \left(\frac{\partial\gamma}{\partial\sigma}\right)^2} + 1 \right) \left(1 + 2X^2 R_x^2 |v_{ac}|^2 \frac{\Omega_c}{\Omega_n} \right). \quad (6.44)$$

When the system is linear or weakly non-linear (S is small), the system Q is finite and is dominated by the damping in the system. Substituting equation 6.22 in equation 6.44 the phase noise can be written as

$$S_\phi = \frac{|v_{n,t}|^2}{|v_{ac}|^2} \left(\left(\frac{\Omega}{2Q\Omega_n} \right)^2 + 1 \right) \left(1 + 2X^2 R_x^2 |v_{ac}|^2 \frac{\Omega_c}{\Omega_n} \right). \quad (6.45)$$

When the system is strongly non-linear the linear definitions of Q is no longer valid. When the resonator is driven strongly non-linear, for a certain forcing function the slope of the resonators phase with respect to frequency is infinite ($\partial\gamma/\partial\sigma = \infty$), when the resonators phase, $\gamma_{dc} = 2\pi/3$. This essentially means the Q is infinite at that operating point and the phase noise equation 6.44 reduces to:

$$S_\phi = \frac{|v_{n,t}|^2}{|v_{ac}|^2} \left(1 + 2X^2 R_x^2 |v_{ac}|^2 \frac{\Omega_c}{\Omega_n} \right), \quad (6.46)$$

where the phase noise is falling of at a slope of $1/f$ due to the $1/\Omega_n$ term. Comparing equation 6.46 with equation 6.45, the phase noise is falling with the slopes were quadratic ($1/f^2$) or cubic ($1/f^3$), due to $1/\Omega_n^2$ and $1/\Omega_n^3$ terms respectively. It is evident from the equations and figure 6.9 that the phase noise of the oscillator operating in the non-linear regime is better than the ones operating in the linear regime.

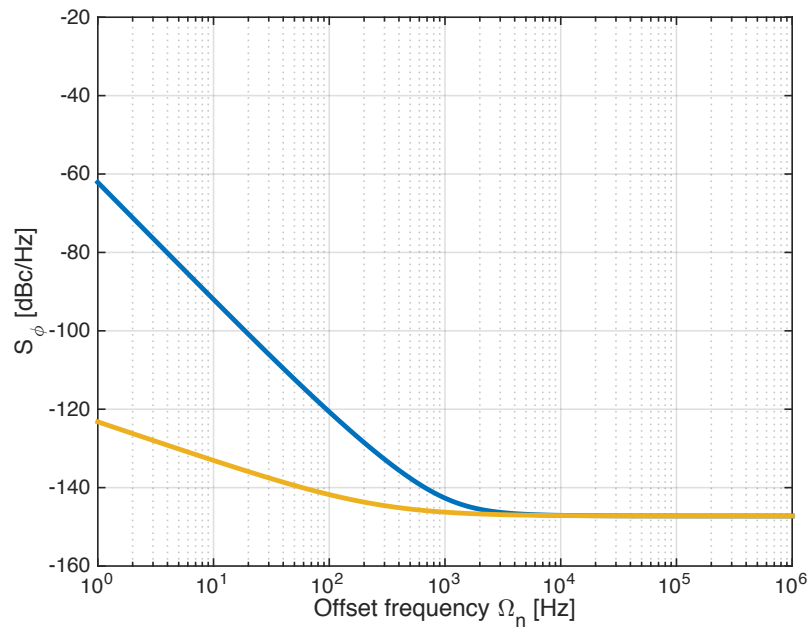


Figure 6.9: Simulated phase noise plots of the resonator with finite (blue) and infinite (yellow) Q . The parameters for the resonator is given in table 6.2. The close-in phase noise for finite Q , is falling with a slope of $1/f^3$ (using equation 6.45), while infinite Q (using equation 6.46) is falling with a slope of $1/f$.

6.7 Summary

The influence of V_{DC} over the effective non-linearity of the resonator was studied. Based on the dimensions of the resonator there is a certain $V_{DC, Lin}$ where the response is near linear ($S \approx 0$). The hardening non-linearities increase with gap ($\propto d^2$) while the softening non-linearities decrease with gap ($\propto 1/d^3$). Increasing the gap d would make S more positive and decreasing the gap lowers the value of S . Non-linear cancellation maximizes the output without any frequency hysteresis in the open-loop operation of the micro beam. This could prove useful for resonant switch applications.

The periodic response of the resonator displacement is defined by modulation equations, a set of two first-order nonlinear ordinary differential equations that describe the modulation of amplitude and phase of the response. Frequency response curves of amplitude and frequency are determined from these modulation equations. Regions of operation where the slope of the frequency response curves are zero and infinite determined. The zero slope point on the amplitude resonance curve is the peak of the resonance curve where the phase (γ_{dc}) of the response is $\pm\pi/2$. For a strongly non-linear system, the resonance curves are skewed based on the amount of non-linearity. For systems that are strongly non-linear, the best region to operate the resonator is the fixed point of the steady state solution that correspond to infinite slope ($\gamma_{dc} = \pm 2\pi/3$) in the frequency response of the system. At this operating point, the slope of the phase with respect to frequency is zero or in other words the rate of change of frequency with respect to phase is infinite. This theoretically leads to an infinite Q.

The best case phase noise response was analytically developed for such a fixed point. Two major aliasing schemes were analyzed and was shown that the capacitive force non-linearity is the major source of mixing that causes the up-conversion of $1/f$ frequency into signal sidebands.

Chapter 7

Conclusions, Contributions and Recommendations

The research objective of this dissertation was to study the influence and benefits of non-linearities on the performance of MEMS switches and resonators. In MEMS switches, the influence of non-linearities in reducing the dynamic pull-in voltage (V_{DP}) was analyzed. In resonators, the effect of various non-linearities in the mixing of low frequency $1/f$ noise into the input signal was investigated. Also, the best region to operate the resonator for optimum phase noise performance was determined. Although the research work in this dissertation focused on RF MEMS devices, specifically switches and resonators, it is relevant to MEMS devices in other application fields. Analytical modeling of process non-idealities of MEMS devices fabricated through a commercial foundry was also conducted. The approaches, results and conclusions arising from this work can be applied to other macro and micro systems for sensing, filtering, timing/signal generation and switching applications.

In this chapter conclusions based on the results of this research are drawn and key contributions are summarized. Finally, future research directions are recommended based on the derived conclusions.

7.1 Conclusions and Contributions

7.1.1 Modeling process non-idealities in a MEMS commercial foundry process

(Work related to this contribution was published in [46], [80])

In chapter 3 an analytical model was derived for a variable gap lateral (DC) contact MEMS switch that accounts for process non-idealities, specifically are the trapezoidal cross-sections (sidewall angle α) for electrodes and springs (instead of rectangular). The effect of electrostatic fringing fields was also modeled as a function of the varying gap instead of a constant fringe factor in the model.

The effect of side-wall angle on pull-in voltage was modeled. For the given switch dimensions and angles of electrodes and springs, the V_{PI} decreases with increase in α when K_x is held constant, and, if influence of α on K_x is included, V_{PI} increases with α . By accounting for electrostatic fringing as a constant in the model instead of modeling it as a function of the variable gap, the pull-in voltage of the switch is under predicted. Finally, the contact resistance measurements of these unpackaged switches show that the contact contamination is a detrimental issue and packaging of MEMS switches in a hermetic environment is essential.

The developed model helps designers predict the capacitances, forces, travel distances before pull-in, spring constants and eventually pull-in voltages of electrostatically actuated structures with inclined side-wall angles. The analytical model estimates the above parameters and matches well with the FEA simulations. This considerably reduces the simulation time for such analysis.

7.1.2 Influence of non-linearities on Dynamic Pull-in of lateral (series) and vertical (shunt) MEMS switches

(Work related to this contribution was published in [81], [82], [83], [84])

Chapters 4 and 5 investigated the dynamic (resonant) pull-in phenomenon as an actuation mechanism for a variable gap lateral DC-contact and vertical shunt capacitive MEMS switches respectively. The lateral switch was designed and fabricated in a commercially available MEMS foundry technology, and the fabrication process for the shunt capacitive switch was developed in the MicrON laboratories at Virginia Tech.

The use of the resonant pull-in technique reduces the overall pull-in voltage $V_{DP}(= \sqrt{V_{DC}^2 + \frac{v_{ac}^2}{2}}) < V_{SP}(= V_{DC})$ required to actuate the switch. There is an additional reduction of total actuation voltage possible via applying an AC actuation signal at the correct non-linear resonant frequency. The best case savings $((V_{SP} - V_{DP})/V_{SP})$ operating at the non-linear resonance is 50 % (for the lateral switch) and 60 % (for the vertical switch) as compared to 25 % and 40 %, respectively, using a fixed frequency approach. Adjacent in bias conditions to the resonant pull-in condition is a condition for which the switch acts as an impact oscillator.

On the other hand, switching time increases for the dynamic case compared to the static case, as shown in measured results for a lateral switch in Chapter 4. To address this shortcoming, transient switching methods are proposed in order to obtain a shorter switching time of the same order as that obtained using static switching for shunt switches in Chapter 4. A shifted-frequency method is proposed where the excitation frequency is shifted up or down by a discrete amount $\delta\Omega$ after a brief hold time. The shifted-frequency method enables a minimum realizable switching time comparable to the static switching time for a given set of actuation frequencies.

The reduction of actuation voltages by dynamic pull-in helps reduce the requirements for charge pump DC-DC converter MEMS switches. Understanding dynamic pull-in is also important in order to predict the upper limit of DC and AC voltages that can be applied to

MEMS resonators without going through pull-in.

7.1.3 Influence of effective non-linearities on the phase noise performance of MEMS electrostatic resonators

(Work related to this contribution was published in [85])

In chapter 6, the influence of V_{DC} on the effective non-linearity of the fixed-fixed microbeam based electrostatic resonator was studied. Based on the dimensions of the resonator and the type of resonance there is a certain $V_{DC, Lin}$ where the response is near linear ($S \approx 0$). In the near-linear domain, the dynamic pull-in is the only upper bound to the amplitude of vibrations, and hence the amplitude of output current, and thereby maximizes the power handling capacity of the resonator. The hardening non-linearities increase with gap ($\propto d^2$) while the softening non-linearities decrease with gap ($\propto 1/d^3$). Increasing the gap d makes S more positive and decreasing the gap lowers the value of S . Non-linear cancellation maximizes the output without any frequency hysteresis in the open-loop operation of the microbeam. This could prove useful for resonant switch applications.

The resonator's periodic response (displacement) is defined by modulation equations, a set of two first-order nonlinear ordinary differential equations that describe the modulation of amplitude and phase of the response. Frequency response curves of amplitude and frequency are determined from these modulation equations. Regions of operation where the slope of the frequency response curves are zero and infinite are determined. The zero slope point on the amplitude resonance curve is the peak of the resonance curve where the phase (γ_{dc}) of the response is $\pm\pi/2$. For a strongly non-linear system, the resonance curves are skewed based on the amount of effective non-linearity S . For systems that are strongly non-linear, the best region to operate the resonator is the fixed point of the steady state solution that correspond to infinite slope ($\gamma_{dc} = \pm 2\pi/3$) in the frequency response of the system. The best case phase noise response was analytically developed for such a fixed point. Two major

aliasing schemes were analyzed and it was shown that the capacitive force non-linearity is the major source of mixing that causes the up-conversion of $1/f$ frequency into signal sidebands.

A major impact of phase noise on receiver performance is the introduction of reciprocal noise mixing of nearby channels with non-ideal oscillator spectrum. Hence, the improvement in phase noise can result in closer channel spacing, in order to maximize the number of users in a given bandwidth.

7.2 Recommendations for Future Work

In this section, some recommendations for future work are made based on the knowledge gained in this research.

7.2.1 RF MEMS Switches

- For modeling process non-idealities of lateral actuators, a better estimation of Young's modulus of the structural material is needed as well as a better understanding of the (tensile or compressive) stress and stress gradients through the thickness of the structure.
- Analytical model developed for MEMS structures matched to Finite Element Analysis (FEA) model can be straight forwardly extended to development of scalable MEMS electro-mechanical models for CAD/design kit integration.
- Experimental verification to support the proposed methods of dynamic switching for MEMS switches in chapter 5 is needed.
- The development of integrated control circuitry to enable dynamic switching and different switching methods as proposed in Chapter 5

7.2.2 RF MEMS Resonators

- The resonator analysis should be extended to resonator based oscillatory systems, which are closed loop feedback systems. This would include a MEMS resonator with an active amplifier in the feedback path to account for the resonator losses. Such systems would be a self-starting systems instead of externally forced excitations. Stability analysis of such a closed loop system accounting for all the non-linearities in the system would provide more insight into optimizing the phase noise performance of the oscillator.
- The analysis and modeling can also be extended to bulk-mode resonators and such resonator based oscillatory systems.
- The analytical phase noise model for resonator based oscillator should be experimentally verified by building a phase feedback oscillatory system, where the phase of the resonator is controlled using a phase shifter in the feedback loop while maintaining the Barkhausen's criteria.

Bibliography

- [1] D. Koester, R. Mahadevan, B. Hardy, and K. Markus, “MUMPs design handbook,” *Revision 6.0, Cronos Integrated Microsystems*.
- [2] G. Marconi, “Wireless telegraphy,” 1905. US Patent 792,528.
- [3] L. Larson, “Microwave MEMS technology for next-generation wirelesscommunications,” in *1999 IEEE MTT-S International Microwave Symposium Digest*, vol. 3, 1999.
- [4] M. Chapman, “The impact of MEMS on cellular phone Architectures,” *Microwave Journal*, vol. 49, no. 5, p. 256, 2006.
- [5] H. De Los Santos, G. Fischer, H. Tilmans, J. Van Beek, N. Res, and I. LLC, “RF MEMS for ubiquitous wireless connectivity. Part II. Application,” *IEEE Microwave Magazine*, vol. 5, no. 4, pp. 50–65, 2004.
- [6] E. Armstrong, “A method of reducing disturbances in radio signaling by a system of frequency modulation,” *Proceedings of the IEEE*, vol. 72, no. 8, pp. 1042–1062, 1984.
- [7] C. Maxey, *Switched-Tank VCO Designs and Single Crystal Silicon Contour-Mode Disk Resonators for use in Multiband Radio Frequency Sources*. PhD thesis, Virginia Polytechnic Institute and State University, 2004.
- [8] C. Nguyen, “Rf mems in wireless architectures,” in *Proceedings of the 42nd annual Design Automation Conference*, p. 420, ACM, 2005.

- [9] J. de la Rosa, R. Castro-López, A. Morgado, E. Becerra-Alvarez, R. del Río, F. Fernández, and B. Pérez-Verdú, “Adaptive CMOS analog circuits for 4G mobile terminals—Review and state-of-the-art survey,” *Microelectronics Journal*, vol. 40, no. 1, pp. 156–176, 2009.
- [10] H. Tilmans, “RF-MEMS: An enabling technology for reconfigurable radio front-ends,” 2008.
- [11] C. Nguyen, “Frequency-selective MEMS for miniaturized communication devices,” in *IEEE Aerospace Conference, 1998. Proceedings.*, vol. 1, 1998.
- [12] K. Petersen, “Silicon as a mechanical material,” *proc. IEEE*, vol. 70, no. 5, pp. 420–457, 1982.
- [13] J. Kubby, “Hybrid silicon-on-insulator micromachining for critical MEMS components,” *Solid State Technology*, vol. 47, no. 9, pp. 69–77, 2004.
- [14] V. Dragoi, T. Glinsner, G. Mittendorfer, B. Wieder, and P. Lindner, “Adhesive wafer bonding for MEMS applications,” in *Proc. of SPIE Vol.*, vol. 5116, p. 161.
- [15] A. Mirza and A. Ayon, “Silicon wafer bonding: key to MEMS high-volume manufacturing,” *SENSORS-PETERBOROUGH-*, vol. 15, pp. 24–33, 1998.
- [16] H. Baltes, O. Brand, A. Hierlemann, D. Lange, and C. Hagleitner, “CMOS MEMS—present and future,” *Membranes*, vol. 19, p. 36, 2002.
- [17] J. Smith, S. Montague, J. Sniegowski, J. Murray, R. Manginell, P. McWhorter, and R. Huber, “Characterization of the embedded micromechanical device approach to the monolithic integration of MEMS with CMOS,” in *Proc. SPIE*, vol. 2879, pp. 306–314, 1996.
- [18] S. Sedky, A. Witvrouw, and K. Baert, “Poly SiGe, a promising material for MEMS monolithic integration with the driving electronics,” *Sensors & Actuators: A. Physical*, vol. 97, pp. 503–511, 2002.

- [19] A. Franke, J. Heck, T. King, and R. Howe, "Polycrystalline silicon-germanium films for integrated microsystems," *Journal of microelectromechanical systems*, vol. 12, no. 2, pp. 160–171, 2003.
- [20] C. Nguyen and R. Howe, "An integrated CMOS micromechanical resonator high-Q oscillator," *IEEE Journal of Solid-State Circuits*, vol. 34, no. 4, pp. 440–455, 1999.
- [21] W. Kuehnel and S. Sherman, "A surface micromachined silicon accelerometer with on-chip detection circuitry," *Sensors and actuators. A, Physical*, vol. 45, no. 1, pp. 7–16, 1994.
- [22] M. Pustan and Z. Rymuza, "Comparative Studies of Advantages of Integrated Monolithic versus Hybrid Microsystems,"
- [23] A. Witvrouw, M. Gromova, A. Mehta, S. Sedky, P. De Moor, K. Baert, and C. Van Hoof, "Poly-SiGe: A Superb Material for MEMS," in *Materials Research Society Symposium Proceedings*, pp. 25–36, 2004.
- [24] G. Rebeiz, *RF MEMS: theory, design, and technology*. John Wiley and Sons, 2003.
- [25] G. Rebeiz, K. Entesari, I. Reines, S.-j. Park, M. El-tanani, A. Grichener, and A. Brown, "Tuning in to RF MEMS," *Microwave Magazine, IEEE*, vol. 10, pp. 55–72, oct. 2009.
- [26] J. Muldavin, R. Boisvert, C. Bozler, S. Rabe, and C. Keast, "Power handling and linearity of mem capacitive series switches," in *Microwave Symposium Digest, 2003 IEEE MTT-S International*, vol. 3, pp. 1915 – 1918 vol.3, june 2003.
- [27] S. Majumder, J. Lampen, R. Morrison, and J. Maciel, "A packaged, high-lifetime ohmic mems rf switch," in *Microwave Symposium Digest, 2003 IEEE MTT-S International*, vol. 3, pp. 1935 – 1938 vol.3, june 2003.
- [28] G. Rebeiz and J. Muldavin, "RF MEMS switches and switch circuits," *IEEE Microwave magazine*, vol. 2, no. 4, pp. 59–71, 2001.

- [29] H. Newman, J. Ebel, D. Judy, and J. Maciel, "Lifetime measurements on a high-reliability rf-mems contact switch," *Microwave and Wireless Components Letters, IEEE*, vol. 18, pp. 100–102, feb. 2008.
- [30] J. Costa, T. Ivanov, J. Hammond, J. Gering, E. Glass, J. Jorgenson, D. Dening, D. Kerr, J. Reed, S. Crist, *et al.*, "Integrated MEMS Switch Technology on SOI-CMOS," in *Solid-State Sensors, Actuators, and Microsystems Workshop 2008*, pp. 18–21.
- [31] M. Fujii, I. Kimura, T. Satoh, and K. Imanaka, "RF MEMS switch with wafer level package utilizing frit glass bonding," in *European Microwave Conference, 2002. 32nd*, pp. 1–3, 2002.
- [32] J. Muldavin, C. Bozler, S. Rabe, P. Wyatt, and C. Keast, "Wafer-scale packaged rf microelectromechanical switches," *Microwave Theory and Techniques, IEEE Transactions on*, vol. 56, pp. 522–529, feb. 2008.
- [33] B. Pillans, J. Kleber, C. Goldsmith, and M. Eberly, "Rf power handling of capacitive rf mems devices," in *Microwave Symposium Digest, 2002 IEEE MTT-S International*, vol. 1, pp. 329–332, 2002.
- [34] C. Goldsmith, D. Forehand, Z. Peng, J. Hwang, and I. Ebel, "High-cycle life testing of rf mems switches," in *Microwave Symposium, 2007. IEEE/MTT-S International*, pp. 1805–1808, june 2007.
- [35] B. Lakshminarayanan and G. Rebeiz, "High-power high-reliability sub-microsecond rf mems switched capacitors," in *Microwave Symposium, 2007. IEEE/MTT-S International*, pp. 1801–1804, june 2007.
- [36] B. Lakshminarayanan, D. Mercier, and G. Rebeiz, "High-reliability miniature rf-mems switched capacitors," *Microwave Theory and Techniques, IEEE Transactions on*, vol. 56, pp. 971–981, april 2008.

- [37] J. Muldavin, C. Bozler, S. Rabe, and C. Keast, "Large tuning range analog and multi-bit mems varactors," in *Microwave Symposium Digest, 2004 IEEE MTT-S International*, vol. 3, pp. 1919 – 1922 Vol.3, june 2004.
- [38] W. Hsu, "Recent Progress in Silicon MemS Oscillators," 2008.
- [39] V. Kaajakari, J. Koskinen, and T. Mattila, "Phase noise in capacitively coupled micromechanical oscillators," *IEEE Transactions on Ultrasonics, Ferroelectrics and Frequency Control*, vol. 52, no. 12, pp. 2322–2331, 2005.
- [40] H. Tilmans, "Equivalent circuit representation of electromechanical transducers: II. Distributed-parameter systems," *Journal of Micromechanics and Microengineering*, vol. 7, pp. 285–309, 1997.
- [41] A. Nayfeh and D. Mook, "Nonlinear oscillations. 1979," *John Willey and Sons, New York*.
- [42] D. Leeson, "A simple model of feedback oscillator noise spectrum," *Proceedings of the IEEE*, vol. 54, no. 2, pp. 329–330, 1966.
- [43] T. M. Schaefer, "Lateral motion mems switch."
- [44] J. Burghartz, B. Rejaei, and H. Schellevis, "Saddle add-on metallization for RF-IC technology," *IEEE Transactions on Electron Devices*, vol. 51, no. 3, pp. 460–466, 2004.
- [45] W. Young and R. Budynas, *Roark's formulas for stress and strain*. McGraw-Hill New York, 1989.
- [46] K. Vummidi, S. Raman, J. Costa, D. Kozuch, I. Ivanov, and J. Hammond, "Laterally driven high isolation dc contact rf mems switch," in *Proceedings of Eurosensors XX, Gotenburg, Sweden, Sep. 17-20*, pp. 336–337, 2006.
- [47] G. Fedder, *Simulation of microelectromechanical systems*. PhD thesis, UNIVERSITY of CALIFORNIA, 1994.

- [48] F. Crotti, “Commemorazione de alberto castigliano,” *Politecnico* 32, vol. (11/12), p. 597, dec. 1884.
- [49] “Coventor, Inc.”
- [50] F. Tay, X. Jun, Y. Liang, V. Logeeswaran, and Y. Yufeng, “The effects of non-parallel plates in a differential capacitive microaccelerometer,” *Journal of Micromechanics and Microengineering*, vol. 9, pp. 283–293, 1999.
- [51] J. Seeger and S. Crary, “Stabilization of electrostatically actuated mechanical devices,” in *Solid State Sensors and Actuators, 1997. TRANSDUCERS’97 Chicago., 1997 International Conference on*, vol. 2, pp. 1133–1136, 2002.
- [52] S. Bromley and B. Nelson, “Performance of microcontacts tested with a novel mems device,” in *Electrical Contacts, 2001. Proceedings of the Forty-Seventh IEEE Holm Conference on*, pp. 122 –127, 2001.
- [53] R. Holm, *Electric contacts: theory and applications*. Springer Verlag, 1999.
- [54] B. Jensen, L.-W. Chow, K. Huang, K. Saitou, J. Volakis, and K. Kurabayashi, “Effect of nanoscale heating on electrical transport in rf mems switch contacts,” *Microelectromechanical Systems, Journal of*, vol. 14, pp. 935 – 946, oct. 2005.
- [55] H. Angus, “Surface films on precious-metal contacts,” *British Journal of Applied Physics*, vol. 13, p. 58, 1962.
- [56] J. W. Tringe, T. A. Uhlman, A. C. Oliver, and J. E. Houston, “A single asperity study of au/au electrical contacts,” *Journal of Applied Physics*, vol. 93, pp. 4661 –4669, apr 2003.
- [57] Y. Wang, Z. Li, D. McCormick, and N. Tien, “A low-voltage lateral mems switch with high rf performance,” *Microelectromechanical Systems, Journal of*, vol. 13, pp. 902 – 911, dec. 2004.

- [58] D. Elata and H. Bamberger, “On the dynamic pull-in of electrostatic actuators with multiple degrees of freedom and multiple voltage sources,” *Microelectromechanical Systems, Journal of*, vol. 15, no. 1, pp. 131 – 140, 2006.
- [59] A. Fargas-Marques, J. Casals-Terre, and A. Shkel, “Resonant pull-in condition in parallel-plate electrostatic actuators,” *Journal of Microelectromechanical Systems*, vol. 16, no. 5, p. 1044, 2007.
- [60] R. CoventorWare, “by CoventorWare Inc,” 2008.
- [61] Y. He, J. Marchetti, C. Gallegos, and F. Maseeh, “Accurate fully-coupled natural frequency shift of mems actuators due to voltage bias and other external forces,” in *Micro Electro Mechanical Systems, 1999. MEMS '99. Twelfth IEEE International Conference on*, pp. 321 –325, jan 1999.
- [62] Y. Lin, W. Li, Z. Ren, and C. Nguyen, “The micromechanical resonant switch,” in *Tech. Digest, 2008 Solid-State Sensor, Actuator, and Microsystems Workshop, Hilton Head, South Carolina*, 2008.
- [63] A. Nayfeh, M. Younis, and E. Abdel-Rahman, “Dynamic pull-in phenomenon in MEMS resonators,” *Nonlinear Dynamics*, vol. 48, no. 1, pp. 153–163, 2007.
- [64] “Zeland Software Inc,”
- [65] E. Abdel-Rahman, M. Younis, and A. Nayfeh, “Characterization of the mechanical behavior of an electrically actuated microbeam,” *Journal of Micromechanics and Microengineering*, vol. 12, p. 759, 2002.
- [66] P. Osterberg and S. Senturia, “M-TEST: A test chip for MEMS material property measurement using electrostatically actuated test structures,” *Journal of Microelectromechanical Systems*, vol. 6, no. 2, p. 107, 1997.
- [67] P. Inc., “OFV-5000 Vibrometer Controller user manual,”

- [68] V. Inc., “Wyko-NT1100 Optical Profiling System datasheet,”
- [69] F. Najar, A. Nayfeh, E. Abdel-Rahman, S. Choura, and S. El-Borgi, “Dynamics and Global Stability of Beam-based Electrostatic Microactuators,” *Journal of Vibration and Control*, 2010.
- [70] Z. Peng, X. Yuan, J. Hwang, D. Forehand, and C. Goldsmith, “Top vs. bottom charging of the dielectric in RF MEMS capacitive switches,” in *Proceedings of Asia-Pacific Microwave Conference, Yokohoma, Japan*, 2006.
- [71] A. Nayfeh and B. Balachandran, *Applied nonlinear dynamics*. Wiley, New York, 1995.
- [72] H. Lee, J. Salvia, S. Yoneoka, G. Bahl, Y. Qu, R. Melamud, S. Chandorkar, M. Hopcroft, B. Kim, and T. Kenny, “Stable oscillation of mems resonators beyond the critical bifurcation point,” in *Solid-State Sensor, Actuator, and Microsystems Workshop, Hilton Head Workshop*, pp. 70–73, 2010.
- [73] R. Mestrom, R. Fey, and H. Nijmeijer, “On phase feedback for nonlinear mems resonators,” in *Frequency Control Symposium, 2007 Joint with the 21st European Frequency and Time Forum, IEEE International*, pp. 765–770, IEEE, 2007.
- [74] R. Behzad, “RF microelectronics,” 1998.
- [75] S. Lee and C. Nguyen, “Phase noise amplitude dependence in self limiting wine-glass disk oscillators,” in *Proc. Hilton Head 2004: A Solid State Sensor, Actuator and Microsystems Workshop (South Carolina)*, 2004.
- [76] M. Younis and A. Nayfeh, “A study of the nonlinear response of a resonant microbeam to an electric actuation,” *Nonlinear Dynamics*, vol. 31, no. 1, pp. 91–117, 2003.
- [77] A. Nayfeh, “Nonlinear interactions: analytical, computational, and experimental methods,” *John Wiley and Sons, New York*, 2000.

- [78] A. Nayfeh, "Introduction to perturbation techniques," *John Wiley and Sons, New York*, 1981.
- [79] S. Lee and C.-C. Nguyen, "Mechanically-coupled micromechanical resonator arrays for improved phase noise," in *Frequency Control Symposium and Exposition, 2004. Proceedings of the 2004 IEEE International*, pp. 144–150, IEEE, 2004.
- [80] K. Vummidi, J. Hammond, J. Costa, and S. Raman, "Modeling of Process Non-idealities of a Variable-gap Electrostatic Laterally Driven Metal contact RF MEMS switch," *Journal of Sensors and Actuators (rebuttal)*.
- [81] K. Vummidi, M. Khater, E. Abdel-Rahman, A. Nayfeh, and S. Raman, "Dynamic Pull-in of Shunt Capacitive MEMS Switches," *Procedia Chemistry*, vol. 1, no. 1, pp. 622–625, 2009.
- [82] K. Vummidi, J. Hammond, J. Costa, and S. Raman, "Resonant Pull-in for a variable gap lateral contact RF MEMS switch," in *Micro Electro Mechanical Systems (MEMS), 2010 IEEE 23rd International Conference on*, pp. 767–770, 2010.
- [83] M. Khater, K. Vummidi, E. Abdel-Rahman, and A. H. Nayfeh, "Dynamic Switching of MEMS Shunt Switches," in *(presented at ASME/IDETC)*, 2010.
- [84] M. Khater, K. Vummidi, E. Abdel-Rahman, A. Nayfeh, and S. Raman, "Dynamic actuation methods for capacitive MEMS shunt switches," *Journal of Micromechanics and Microengineering*, vol. 21, p. 035009, 2011.
- [85] K. Vummidi, B. K. Hammad, A.-R. E, A. H. Nayfeh, and S. Raman, "Micromechanical resonators with near-linear response," in *Proceedings of ASME Inter-national Mechanical Engineering Congress 2008, October 31 - November 6, Boston, Massachusetts, USA.*, 2008.